Calibration of A Small Anode Germanium Well Detector

Master's Thesis, 7.6.2017

Author:

Joonas S. Tikkanen

Supervisors:

Roy Pöllänen (STUK),
Jaana Kumpulainen (JYFL)

Abstract

Tikkanen, Joonas
Calibration of A Small Anode Germanium Well Detector
Master's thesis
Department of Physics, University of Jyväskylä, 2017, 86 pages.

Calibration of a small anode germanium (SAGe) well detector was performed for three sample geometries. Two of the geometries were cylindrical containers measured on top of the detector and one was a test tube measured inside the well. The full energy peak efficiency calibrations were done with certified samples ordered from NPL. One-nuclide samples were manufactured from radioactive solutions for the total efficiency calibration. The total efficiency calibration was done by simulating the total efficiency with MCNP and adjusting the model to match the experiments. The calibrations were done for energy range between 30 keV and 1.9 MeV. The calibrations were reliable enough for the detector to be used in accredited gamma-ray spectrometric measurements.

Keywords: SAGe well detector, full energy peak efficiency calibration, total efficiency calibration, coincidence correction

Tiivistelmä

Tikkanen, Joonas
Calibration of A Small Anode Germanium Well Detector
Pro Gradu -tutkielma
Fysiikan laitos, Jyväskylän yliopisto, 2017, 86 sivua.

SAGe kolokiteen kalibroinnit suoritettiin kolmelle näytegeometrialle. Kaksi geometrioista oli sylinterin muotoisia purkkeja, jotka mitattiin ilmaisimen päällä ja yksi koeputki, joka mitattiin kolon sisällä. Piikkitehokkuuskalibrointi tehtiin NPL:sta tilattujen sertifioitujen näytteiden avulla. Yksinuklidinäytteitä valmistettiin radioaktiivisista liuoksista totaalitehokkuuskalibrointia varten. Totaalitehokkuuskäyrä saatiin simuloimalla totaalitehokkuudet MCNP:llä ja sovittamalla malli vastaamaan kokeellisia tuloksia. Kalibraatiot tehtiin energiavälille 30 keV–1.9 MeV. Kalibroinnit olivat tarpeeksi luotettavia, että ilmaisinta voidaan käyttää akkreditoiduissa gammaspektrometrisissä mittauksissa.

Avainsanat: SAGe kolokide, piikkitehokkuuskalibrointi, totaalitehokkuuskalibrointi, koinsidenssikorjaus

Aknowledgements

I would like to thank Roy Pöllänen and Jaana Kumpulainen for supervising this thesis. Roy helped in numerous ways with problems related to calibrations and I am thankful for the vast amount of time he spend helping me. From other people who helped during the making of this thesis I would like to mention Jani Turunen and Antti Vainonen, who helped with UniSAMPO Shaman spectrum analysis program and other issues, Sinikka Virtanen, who prepared the samples and gave advice regarding chemistry, Mikko Teräväinen, who helped with detector configuration, Jaana Joenvuori, who revised the language of the thesis and Teemu Siiskonen who guided me in the use of Monte Carlo simulation software. I am also in gratitude to Pia Vesterbacka, Radiation and Nuclear Safety Authority of Finland (STUK) and the university of Jyväskylä for giving the opportunity to write this thesis.

Helsinki, 7th of June, 2017

Joonas Tikkanen

Contents

1 Introduction

Germanium detectors are made of low impurity germanium crystals enveloped inside a vacuum. Germanium is a semiconductor material and when radiation enters the crystal, it excites electrons to the conduction band. If an electric field is applied to the crystal, the charges can be collected and the resulting current gives information about the energy deposited in the crystal. The result in gamma-ray spectrometry is a spectrum from which nuclides present in a sample and their activities can be calculated.

Because of the small energy gap between the germanium valence and conduction bands, the Ge detectors have to be kept in low temperatures to reduce the thermal excitation of the electrons to the conduction band. The cooling is usually done with liquid nitrogen which keeps the detector near the temperature of 77 K. The Ge crystal has to be kept in a vacuum to keep it insulated. The outer shell of the detector, called end cap, is usually made of aluminum.

The first germanium detectors became commercially available in the 1960s and were made by adding lithium atoms to the crystal material [1]. This helped to balance effects caused by impurities and made the use of larger crystals possible. The lithium doped germanium detectors were called Ge(Li) detectors. The Ge(Li) detectors had to be kept constantly cooled. The methods for producing germanium developed and smaller impurity concentrations were achieved. The detectors that were made from the low impurity materials were called high purity germanium, or HPGe, detectors and they became commercially available in the 1980s. The performance of the detectors were equal, but unlike with Ge(Li) detectors, the HPGe detectors could be heated to room temperature without damaging the detector.

The well detector is a special configuration of germanium detectors where there is a cylindrical hole at the center of the crystal. This makes it possible to place the samples inside the hole. The fraction of the solid angle of the crystal surrounding the sample, or the *geometrical efficiency*, can be almost 100%. Therefore the radiation detection efficiency will usually be larger than for detectors where the sample is measured on top of the detector.

The gamma spectrometry laboratory at STUK measures environmental samples, fallout samples, air filters and foodstuffs to name a few. Over 3000 samples were measured in 2016 with fourteen HPGe detectors. The samples are related to monitoring of the radioactive nuclides in the environment or to activity certificates for export for example. The gamma spectrometry laboratory has a Finnish Accreditation Service accreditation.

The small anode germanium well detector is a novel type of detector where relatively low energy gamma-rays can be detected inside the well. The goal of this thesis is to make the required calibrations so that the detector can be used in accredited measurements and document the calibration procedure properly. The focus is on the detection efficiency calibrations. The optimization of the detector resolution and background subtraction are among other topics.

Using the SAGe well detector introduces new types of challenges. The summing effects of gamma rays emitted simultaneously cause large correction factors because of the geometric efficiency. Better detection efficiency when compared to earlier well detector models at energies below 40 keV amplify the summing issues. Also, the detector was the first well detector at STUK and for these reasons its calibration required more attention than a regular HPGe detector. In spite of the shortcomings, using the SAGe well detector leads to smaller minimum detectable activities with small sample volumes when compared to other types of Ge detectors.

The first chapters are dedicated to give the reader basic knowledge about Ge detectors and gamma spectrometry. The software and numerical methods used in the spectrum analysis and simulations are introduced thereafter. The rest of the thesis consists of description of the measurements, simulations, results and discussion of the results. The reader is assumed to have knowledge about interactions of radiation with matter and know the fundamentals of radiation detection.

2 Germanium Detectors

Germanium detectors are widely used in physics due to their superior energy resolution when compared to e.g. NaI detectors. Ge detectors have to be kept in low temperatures and therefore equipment are needed for the cooling. Other limiting factors in the use of Ge detectors is their high price and limitations in growing the germanium crystal.

2.1 Principles of Ge Detectors

When a gamma ray enters a germanium crystal, it can interact with an electron giving it kinetic energy. This electron collides with other electrons exciting them from the valence band to the conduction band. Every excitation creates an electron hole pair. The amount of electrons and holes produced is proportional to the energy of the radiation and can be written as

$$N = \frac{E}{\epsilon}, \tag{2.1}$$

where E is the energy deposited in the crystal by the radiation quantum and ϵ is the average amount of energy required to create one electron hole pair. For germanium, $\epsilon = 2.96$ eV [2].

The created charge can be collected by applying a voltage across the crystal. Unlike in gaseous radiation detectors, both electrons and holes contribute to the collected charge. The hole is filled by another electron which creates another hole in the position of the shifted electron and so on. Since electrons move on average in opposite direction to the electric field, the holes propagate towards, and are collected at the cathode. Diffusion also affects the movement of the charge carriers.

In a pure germanium crystal the number of electrons and holes would be equal. Pure crystals are in practice impossible to manufacture and there are always some impurities left. In n-type semiconductors the impurity atom has one more electron on the outer shell than the crystal material. Germanium forms four covalent bonds with surrounding atoms. When the impurity atom occupies a lattice point in the crystal, one electron is left without a pair. The impurity atom is in this case called a *donor*. Energy of this electron is near the conduction band and it is easily excited across the forbidden gap. Even at 77 K, a large fraction of these electrons are on the conduction band. In p-type semiconductors the impurity atoms have one electron less on the outer shell. These atoms form states in the crystal that can

be occupied by electrons on the conduction band. Energy levels of these states are slightly above the valence band and the crystal can be seen as having an excess of holes. These impurity atoms are called *acceptors*. A common name for donors and acceptors is dopant. The electrons in n-type materials and the holes in p-type materials dominate the electrical conductivity [1].

In a pn-junction, a p-type and an n-type semiconductor are put in contact. Some of the excited electrons in the n-type material diffuse across the junction and combine with the holes. This leaves positive ions on the n side and creates negative ions on the p side producing a space charge across the junction. This inhibits further diffusion because electrons are repelled by the negative charge on the p side.

If a large enough voltage is applied through the junction so that the electric field is from n to p side, the electrons can get through to the p side and the junction begins to conduct. In the opposite case, the applied electric field draws the conduction band electrons and holes on the p side further away from the junction. This creates a volume that is similar to pure crystal structure. This volume is called the *depletion region*. The depletion region grows when the electric field from p to n side is increased. The growth continues until the whole crystal is depleted or the voltage is so large that the junction brakes down (the break down voltage) and begins to conduct. When radiation excites electrons in a completely depleted crystal, the situation is almost identical to pure crystal and the charges can be collected efficiently. Another name for pn-junction is diode. In the book by Knoll [1], the depletion depth d for a semiconductor detector with planar geometry is approximated by

$$d \approx \left(\frac{2\epsilon V}{eN_d}\right)^{1/2}, \tag{2.2}$$

where N_d is the dopant concentration in the detector crystal (donors for n- and acceptors for p-type material), e is the unit charge and V is the voltage across the junction.

Gamma-ray detectors are usually made of solid material to achieve high enough cross section for the photon interactions. Scintillation detectors are efficient in detecting gamma-rays but they have a poor energy resolution. Semiconductor detectors have sufficient cross sections for efficient detection of gamma-rays if the depleted region can be made large enough. From the equation (2.2) we can see that ϵ and the dopant concentration determine the thickness of the depleted volume (voltage can be increased only to the breakdown voltage). For silicon ϵ is 3.62 eV [2]. Germanium can be produced in higher purity than silicon and because of this and the smaller ϵ is better suited for gamma-ray detection. Impurity concentrations of 10^9 cm^{-3} to 10^{10} cm^{-3} are achieved when manufacturing high purity germanium crystals [3].

In practice, the charges cannot be collected from the entire volume of the crystal. There will always be a *dead layer* on the surface where the charge carriers created by radiation are not collected. The thickness of the dead layer, especially on the top of the detector affects the detection efficiency of low energy gamma-rays significantly.

Most of the dead layer is caused by the electric contact on the top. The thickness can be as low as tenths of a micrometer [1].

Although small value of ϵ increases the amount of charge carriers and makes thicker crystals possible, it also increases thermal excitation of valence band electrons. The probability per unit time for a creation of an electron hole pair is given by

$$p(T) = CT^{3/2}\exp\left(-\frac{E_g}{2kT}\right), \tag{2.3}$$

where E_g is bandgap energy, T the absolute temperature, k the Boltzmann constant and C proportionality constant characteristic of the material. For germanium $E_g =$ 0.665 eV at 300 K and 0.746 eV at 0 K [1]. Approximating the forbidden gap at liquid nitrogen temperature 77 K to be equal to that at 0 K, we can calculate the difference in thermal excitation probability to be

$$\begin{aligned}\frac{p(300\text{ K})}{p(77\text{ K})} &= \frac{(300\text{ K})^{3/2}}{(77\text{ K})^{3/2}} \cdot \exp\left[\frac{1}{2 \cdot 8.617 \cdot 10^{-5}\text{ eV/K}}\left(\frac{0.746\text{ eV}}{77\text{ K}} - \frac{0.665\text{ eV}}{300\text{ K}}\right)\right] \\ &= 5.18 \cdot 10^{19}.\end{aligned}$$

To reduce the leakage current caused by thermal excitation, Ge detectors are operated at low temperatures.

2.2 The Fano Factor and Timing Characteristics

If the creation of electron hole pairs along the path of the radiation particle is assumed to be a Poisson process, the variance of N would be E/ϵ, which means $\sigma_N^2 = N$, where σ_N is the standard deviation of N. However, the observed variance is always smaller. This can be taken into account with the *Fano factor*, which is defined as

$$F = \frac{Observed\ variance}{E/\epsilon}. \tag{2.4}$$

One wants the Fano factor to be as small as possible to obtain a better energy resolution. The standard deviation can now be expressed as

$$\sigma_N = \sqrt{\frac{FE}{\epsilon}}. \tag{2.5}$$

The standard deviation of energy deposited in the medium is given by

$$\sigma_E = \epsilon\sigma_N = \sqrt{\epsilon FE}. \tag{2.6}$$

The value of the Fano factor can be approximated to be 0.1 for germanium and silicon [2].

When considering charge collection, the charges can be approximated to be created at a single point. The time to collect the charge depends on where in the detector

the excitations happen. Even though both holes and electrons contribute to the pulse amplitude, the saturation velocity of the electrons is 2-3 times higher than for holes. A simplified idea of how the charge collection and pulse formation happens is given in Figure 2.1. The time to collect the two charge carriers varies depending on carrier type and their drift distances. The lower plot represents the pulse when the charges are integrated with a long time constant [1].

The *rise time* is usually defined as the time it takes for a signal to change from 10% to 90% of its maximum value. It is strongly dependent on the resistances and capacitances of the components in the measurement circuit. If the rise time is short, then the duration of the pulse will also be short. This means that as small a rise time as practically possible should be used. Shorter pulse duration decreases the chance of another radiation particle entering the detector during the charge collection and thus contributing to the same pulse (pulse pile up). On the other hand, rise time should be long enough for complete charge collection to occur. *Dead time* is the time during which the measurement system is unable to process new pulses without overlap with the previous one. Dead time increases with activity and can be decreased with shorter rise times.

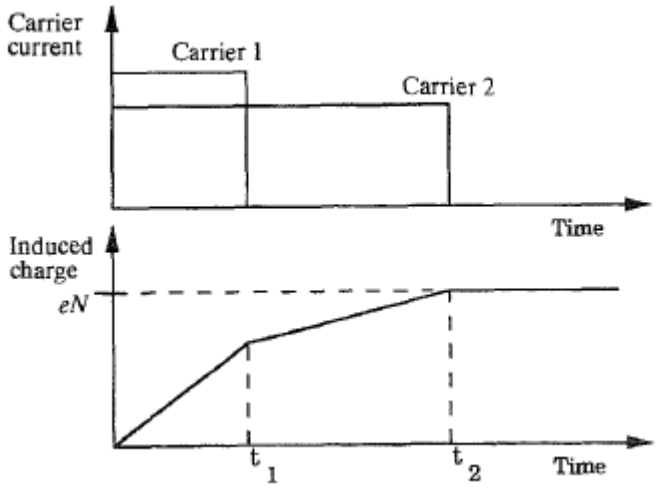

Figure 2.1. Upper plot: The idealized representation of electron and hole currents after the interaction of a photon. The faster component (caused by electrons or holes) depends on the drift distances and mobilities of the charge carriers. Lower plot: Induced charges of the charge carriers integrated with an infinite time constant. t_1 is the collection time for the faster carrier type and t_2 the collection time for the slower. [1]

2.3 Configurations of Ge Detectors

There are two types of configurations of Ge detectors: Planar and coaxial. In planar configuration the crystal is a round disc with contacts on top and bottom. The material can be p or n type. For example Canberra's Broad Energy Germanium (BEGe) detectors use planar crystals (Figure 2.2).

In coaxial geometry, the crystal is a cylinder with a cylindrical hole in the center (Figure 2.3). One electrical contact is on the outer surface and the other inside the hole. The hole can go through the whole detector, or it can go through only partially. The latter case is called a blind hole and it leaves an intact surface at the other end of the cylinder. Detectors that are penetrated completely are called true coaxial, and those that are penetrated partially are called closed-end coaxial detectors. In closed-end coaxial detectors the electric field is not radial in the closed end. This effect can be reduced by making the hole deeper and rounding the corner of the closed end. The rounding is called bulletization [1].

A special case of the coaxial configuration is a well configuration (Figure 2.4). In it, a closed end coaxial crystal is turned upside down so that the sample can be placed inside the hole. This enables almost a 100% geometrical efficiency for small samples inside the well, allowing large detection efficiencies. This, on the other hand, increases dead time and summing effects discussed in chapter 3.2.

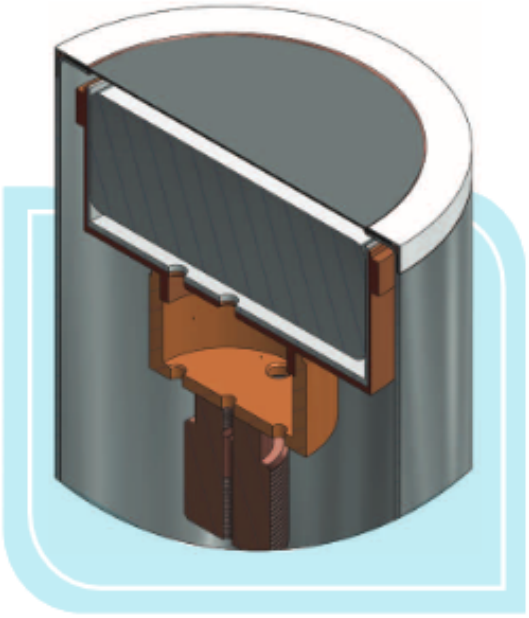

Figure 2.2. Canberra's Broad Energy Germanium (BEGe) Detector. The germanium crystal is in vacuum and the sample is placed on a thin carbon epoxy window. Picture from www.canberra.com

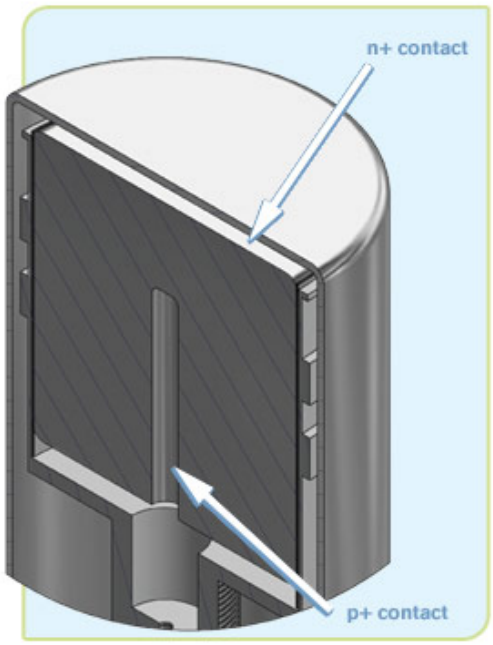

Figure 2.3. Coaxial Ge detector configuration. Picture from www.canberra.com

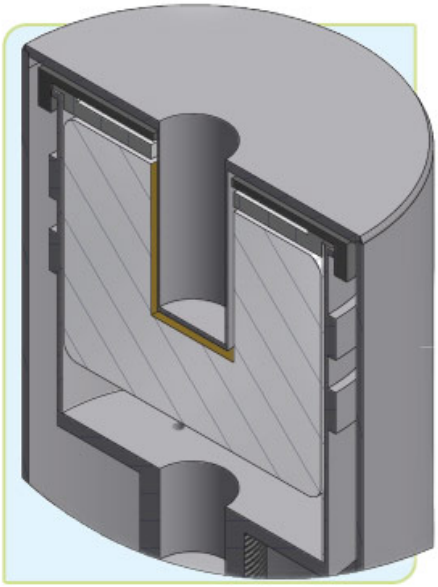

Figure 2.4. Well detector configuration. Picture from www.canberra.com

A cryostat is used to connect the detector to the cooling system. It consists of a heat conducting rod that connects the crystal to liquid nitrogen. This system is kept insulated by enveloping it with aluminum and pumping a vacuum inside. The part surrounding the crystal is called the *end cap*. On the top side of the end cap is an entrance window that can be made from aluminum, beryllium or carbon epoxy, for example. The thickness of the window should be small to prevent absorption in it. Reduction of resolution might be a symptom of vacuum loss. The liquid nitrogen is kept inside an insulated container called a *dewar*. An example of a cryostat dewar system is shown in Figure 2.5.

Even though the system is well insulated, the nitrogen level in the dewar decreases with time and regular dewars have to be filled approximately once a week. Some dewars are equipped with electrical cooling systems that cool the vaporized nitrogen back into liquid state. Examples of these types of dewars are Ortec's Möbius and Canberra's Cryo-Cycle. The cooling can also be done completely electronically but this leaves the detector vulnerable to power outages.

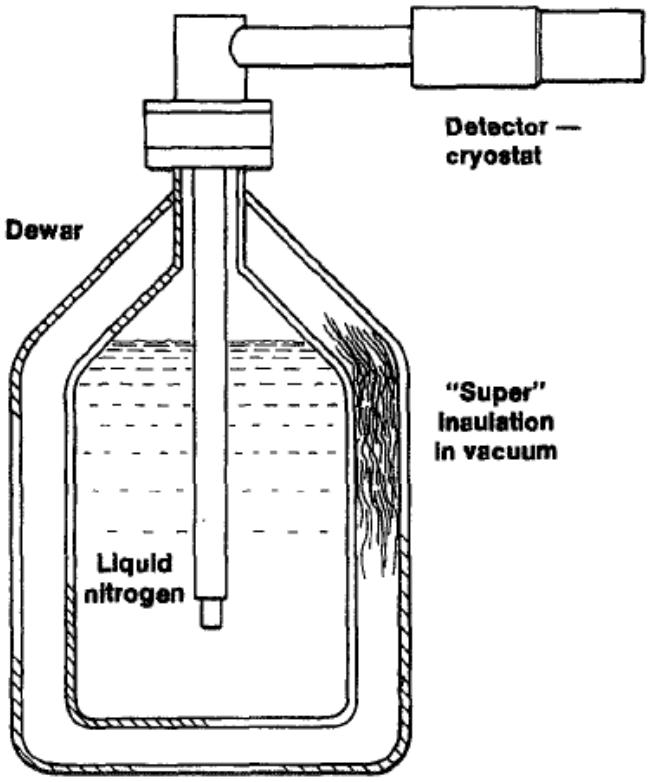

Figure 2.5. Configuration of a cryostat dewar system. In this figure the detector is in horizontal position but it can also be aligned in other directions. [1]

3 Gamma-ray Spectrometry

Gamma-ray spectrometry, or gamma spectrometry, is a method for identifying the radionuclides and for determining their activities in a sample. Ge detectors are well suited for gamma spectrometry because of their energy resolution. With good resolution it is possible to calculate activities of different nuclides that emit gamma rays with energies close to each other. The result of a measurement is a spectrum that has to be analyzed to obtain the results.

3.1 Pulse processing

A schematic of pulse processing is shown in Figure 3.1. After the charge collection, the signal goes through a preamplifier. The current is converted into voltage that rises quickly when radiation enters the crystal and decays slowly (Figure 3.1). The rise in the voltage ΔV is proportional to the created charge and therefore to the energy deposited in the Ge crystal. The preamplifier is usually attached to the detector cryostat system and is close to the crystal. This means that the amplifier, or at least some of its components, are near liquid nitrogen temperature. At low temperatures the noise caused by the amplifier is reduced. The level of amplification can be adjusted and this is important while performing the energy calibration (section 3.3).

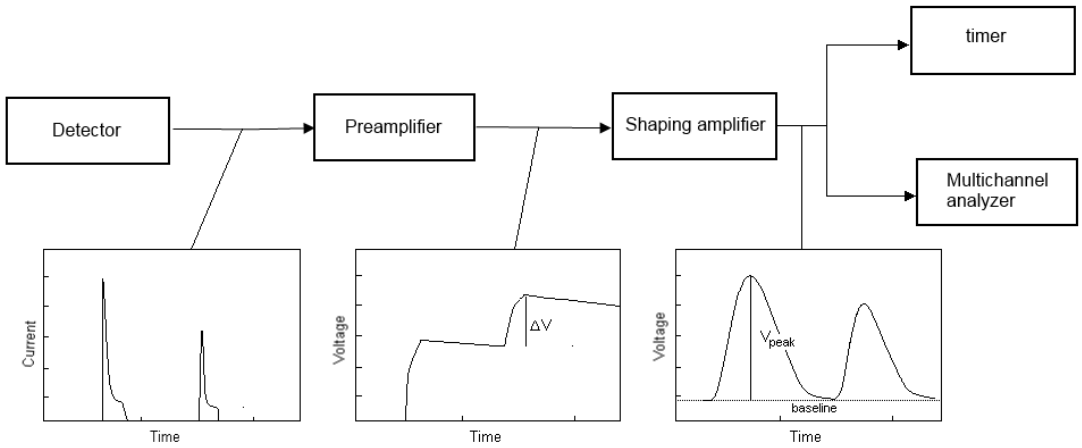

Figure 3.1. Schematic of pulse processing in gamma spectrometry.

The pulse from the preamplifier is put through another amplifier called a *shaping amplifier*. It is used to shape the pulse into a form where the voltage rises to the maximum value of V_{peak} and drops quickly to the baseline. V_{peak} is proportional to ΔV and therefore to the created charge. The duration of a pulse is characterized by the *shaping time* of the amplifier. The shorter the pulses are, the lower the probability of pulse pile up. Another characteristic of the pulse shape is the rise time discussed in section 2.2. The relation between shaping time and rise time depends on how the pulse is shaped. The shaping amplifier is not attached to the detector except in case of portable detectors.

The pulse may decay so that the voltage is below the baseline after the pulse. This effect is called undershoot. If another pulse is processed during this period the maximum voltage of the pulse will be lower and the registered energy will be incorrect. The same applies if the voltage is above the baseline. The circuitry can be shaped so that voltage drops to baseline quickly and without dropping below it. The behavior can be adjusted with a rheostat. This technique for baseline restoration without undershoot is called *pole zero cancellation* [1].

If the volume of the detector crystal is large, there will be significant fluctuations in charge collection time. This will in turn lead to variation in the shaping amplifier output, and therefore to resolution degradation, if the pulse shape is Gaussian. This effect is called *ballistic deficit*. One method to reduce the ballistic deficit is to shape the pulse into a trapezoidal shape. Trapezoidal pulse with three different charge collection times are shown in Figure 3.2. The length of the constant amplitude is called a *flat top* and it can be adjusted. If the flat top is long enough, every pulse has time to reach the maximum amplitude before starting to decay and there will be no variation in output voltage. However, increasing the flat top will increase pulse length and therefore the dead time will increase [1, 4].

Part of the pulses can be discarded with discriminator circuits. Discriminators can pass pulses above some threshold level and reject distorted pulse shapes and pile up events, for example [1].

There are also discriminators that select pulses with amplitudes between upper and lower threshold levels. This kind of discriminator is called a differential discriminator or a *single channel analyzer* (SCA). Pulses from a SCA can be put to a counter. The counter stores the number of pulses passed through the SCA during the measurement. However, counts in single energy region, or *channel*, are not of particular interest in gamma-ray spectrometry. To obtain a spectrum, a *multichannel analyzer* (MCA) is used. MCA can be thought of as a device that has multiple SCAs with distinct energy thresholds and a counter for each channel. The width of each channel is equal. The results of a measurement can be plotted as a histogram, where the number of counts is plotted for each channel. This histogram is called the pulse height spectrum. At STUK, MCAs used in gamma spectrometry have 8192 (2^{13}) channels and the energy range for one channel is approximately 0.33 keV.

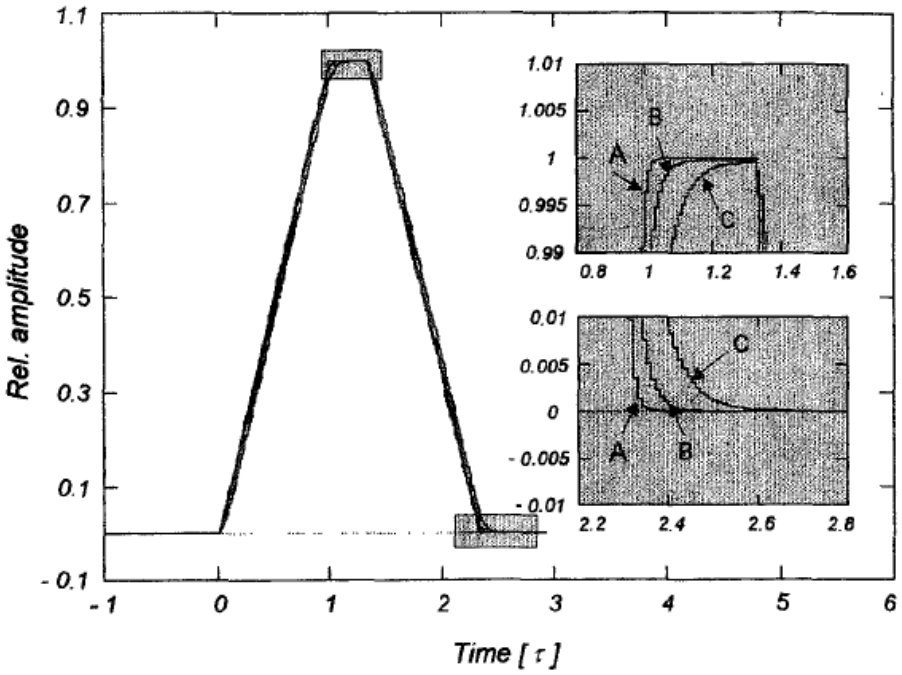

Figure 3.2. Effect of trapezoidal shaping with three different detector charge collection times. If the constant amplitude, or the flat top, is long enough, the pulses will have the same amplitude. [1]

3.2 Analysis of the spectrum

An example of a pulse height spectrum measured with a Ge detector is shown in Figure 3.3. The channel number is calibrated to match the energy deposited in the active volume of the detector. Some areas have larger count rates than the channels in their vicinity and form a shape close to a bell curve. These areas are called peaks. The more stable area between the peaks is called the baseline. The energy of a peak is determined as the energy at the maximum amplitude.

Decaying nuclides emit a gamma-ray or gamma-rays of specific energies. Therefore the energy of a peak can be traced back to a nuclide. For example, the large peak in the middle of the spectrum in Figure 3.3 corresponds to an energy of 1460.8 keV originating from the decay of ^{40}K. If a peak corresponds to one transition in a nuclide, it is called a *full energy peak* (FEP). If the detection efficiency is known, the activity of the nuclide in a sample can be calculated.

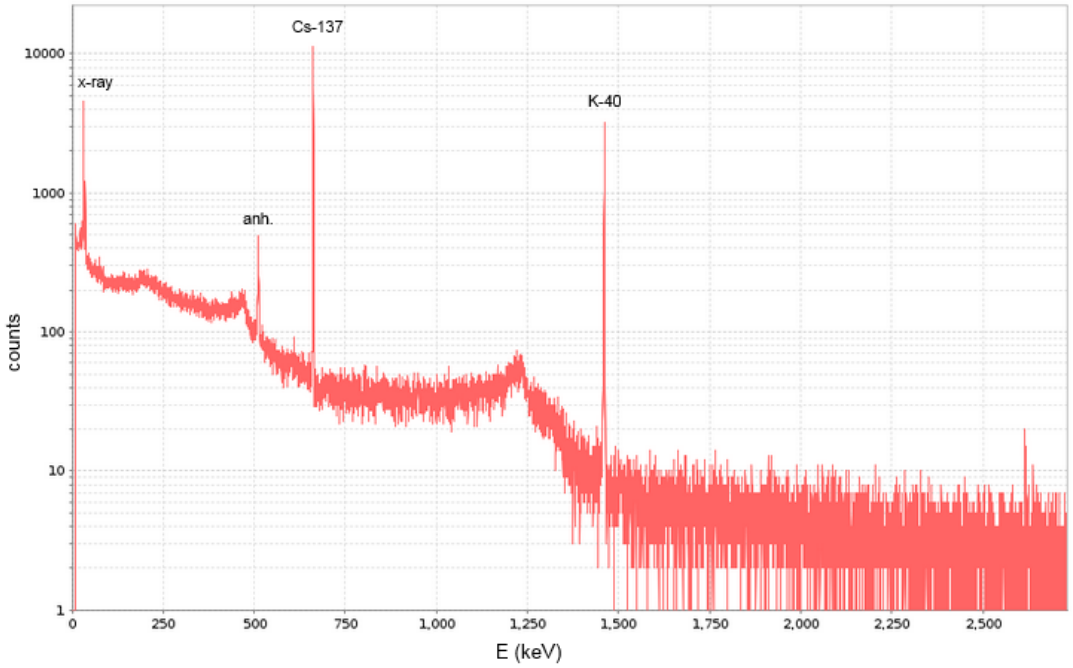

Figure 3.3. Example of a pulse height spectrum measured with a Ge detector. The sample was a perch sample and it contained ^{137}Cs and ^{40}K. The annihilation peak (anh.) at energy 511 keV is from annihilation of positrons.

3.2.1 Background

In an ideal case the counts in the channels outside peaks would be zero. In reality, however, there is always a background in the spectrum. Part of the background originates from radioactivity in the environment. Construction materials in the walls, floor and ceiling contain radioactive nuclides from which ^{40}K and natural decay chains of uranium are usually the most important. Air also contains radioactive nuclides, examples of which are ^{222}Rn and ^{7}Be. These nuclides cause both stable background and peaks in the spectrum.

Some of the background is of cosmic origin. Protons and alpha particles with energies up to 10^{18} eV and a mean energy of approximately 5 GeV originate in supernovas. These particles collide in the atmosphere creating secondary radiation, mostly π-mesons. The original particles and the secondary radiation cause a continuously distributed background with some peaks related to excitations in the detector and surrounding materials [2].

The background from the environment can be effectively reduced with shielding. The detector is placed inside a cavity surrounded with high Z material, usually lead. This reduces the effect of all the radiation originating outside the shield on the measurements. However, the radiation originating from the sample can excite electrons on the inner shell of lead atoms. This leads to emission of x-rays from the

shield. The K x-rays of lead have energies of 73 keV, 75 keV and 85 keV. The effect of the x-rays can be reduced by placing a layer of copper on the inner surface of the shield. The x-rays of copper have energies below 9 keV and therefore their detection is improbable. A layer of plastic can be put on the inner surface of the shield to lessen the bremsstrahlung radiation caused by electrons from the sample colliding with the shield.

The background caused by nuclides in air can be reduced by either keeping the inside of the shield in vacuum or, more practically, keeping an overpressure of nitrogen inside the shield [5]. Some gamma spectrometry laboratories are placed deep underground to lessen the effects of cosmic radiation: the thick layer of rock absorbs most of the high energy particles.

Radioactive contamination inside the shield would lead to increased background and extra peaks. This increases the background but is especially problematic when the nuclide causing the contamination can be found in samples. Therefore the users of Ge detectors should pay attention to keep the environment in the laboratory clean of any unwanted radioactive materials. The contamination, as any other background arising from the surroundings can be taken into account by performing background measurements.

Most of the background is usually caused by Compton scattering of photons. The Compton scattering cross section for energies of interest is significant. A gamma-ray can go through multiple scatterings before being absorbed through photoelectric effect. If these scatterings and the photoelectric absorption occur inside the active volume of the crystal the resulting pulse will contribute to the FEP. If the scattered rays escape or the scattering occurs outside the active volume, the pulse will be a part of the background.

The energies of the scattered photon and the recoil electron are given by

$$E'_\gamma = \frac{E_\gamma}{1 + (E_\gamma/m_e c^2)(1 - \cos\theta)} \tag{3.1}$$

and

$$E_e(\theta) = E_\gamma \frac{(E_\gamma/m_e c^2)(1 - \cos\theta)}{1 + (E_\gamma/m_e c^2)(1 - \cos\theta)}, \tag{3.2}$$

where E_γ is the energy of the photon prior to and E'_γ after the scattering, $m_e c^2$ the rest energy of an electron (511 keV) and θ the scattering angle [1]. θ can have values between 0 and π which means that the energies of the recoil electrons are between zero ($\theta = 0$) and

$$E_e(\pi) = E_\gamma \frac{2E_\gamma/m_e c^2}{1 + 2E_\gamma/m_e c^2}. \tag{3.3}$$

Because a fraction of the scattered photons escape the crystal, there will be a *Compton continuum* in the spectrum. A simplified image of a spectrum without background from outside the source is shown in Figure 3.4. At the end of the continuum

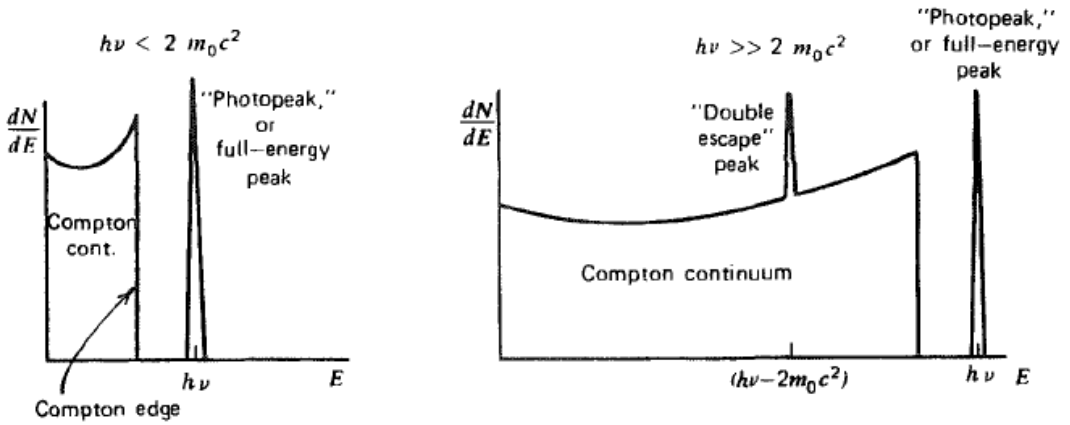

Figure 3.4. The simplified effect of Compton continuum on a spectrum in a small detector. The enrgy of the photons is $h\nu$, where ν is the frequency of the photon and h is the Planc's constant. Notice the U-like shape and the sharp edge of the continuum. On the image on the right side there is the double escape peak discussed in section 3.2.2. [1]

there is a *Compton edge* where the contribution of Compton scattering to the background is zero. The Compton edge for the decay of ^{40}K can be seen in Figure 3.3 at the energy of about 1240 keV and for the decay of ^{137}Cs in Figures 3.3 and 3.5 at the energy of 477 keV. The actual background caused by Compton scattering differs from the one in Figure 3.4 because the gamma-rays can go through multiple scatterings before escaping the detector. The photons can also scatter before entering the crystal active volume [1].

The energies of the scattered photons from equation (3.1) are close to each other between scattering angles of 110° and 180°. This leads to photons scattering from different angles around the detector contributing to a single peak in the spectrum called the *backscatter peak*. For photons that scatter in head on collisions ($\theta = \pi$) the energy of the scattered photon is

$$E'_\gamma = \frac{E_\gamma}{1 + 2E_\gamma/m_ec^2}. \tag{3.4}$$

For energies much larger than m_ec^2 this becomes

$$E'_\gamma \approx \frac{m_ec^2}{2} = 255.5 \text{ keV}. \tag{3.5}$$

Thus the backscatter peak, if large enough to be observed, is always below 255.5 keV. The backscatter peak caused by the 661.7 keV gamma-rays is shown in Figure 3.5. The energy of the peak is 184 keV.

The use of the terms background and baseline for the areas in the spectrum between peaks can be quite arbitrary. The background can refer to the baseline or to the pulses caused by radioactivity in the environment. Baseline always refers to the area caused by Compton effects that has to be subtracted to get the actual peak area.

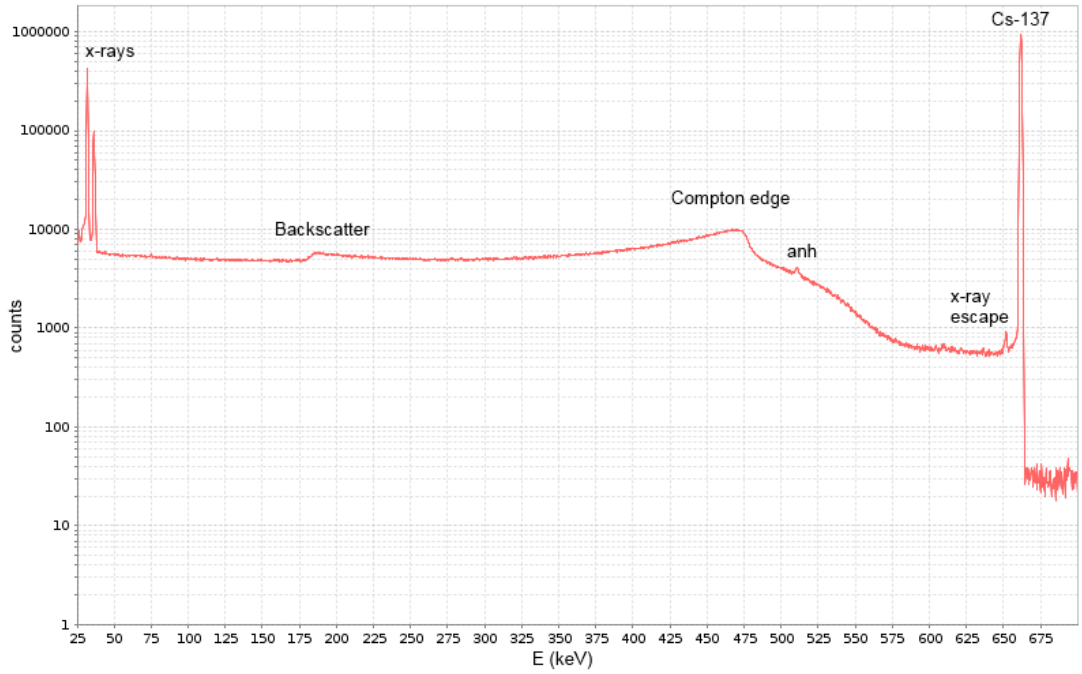

Figure 3.5. Backscatter peak, Ge x-ray escape peak and Compton edge caused by the 661.7 keV photons.

3.2.2 Escape peaks

For photons with energy above 1022 keV interaction through pair production is possible. The creation of the two particles requires 1022 keV and the rest of the photon energy is converted into kinetic energy of the particles. After its creation, the electron behaves as any electron excited in Compton scattering or photoelectric effect. It collides with atoms exciting other electrons to the conduction band to the point when its energy is below ϵ.

A positron dissipates its energy in the medium in the same way as electrons until it reaches thermal energies [2]. After reaching thermal energies, it annihilates with an electron creating two photons with an energy of 511 keV. If both of these photons are absorbed in the germanium crystal, the original gamma-ray contributes to the FEP. However, some fraction of the annihilation photons will escape the detector. This leads to *single* and *double escape peaks* in the spectrum. Single escape peaks consists of pulses where one of the 511 keV photons escaped. The energy of this peak is therefore 551 keV below the FEP. Pulses where both annihilation photons escaped form the double escape peak at 1022 keV below the FEP. Right side of Figure 3.4 shows only the double escape peak because the figure represents spectra measured with a small detector where the probability of absorbing either of the secondary photons is small.

Radiation inside the Ge crystal can cause excitation of the inner shell electrons of

germanium atoms. This leads to emission of x-rays with energies of approximately 10 keV. Part of these x-rays escape the detector active volume. The probability of the escape is significant only near the active volume edge. The events where one of the Ge x-rays escape form a peak in the spectrum 10 keV below a FEP. The Ge x-ray escape peak can be seen in Figure 3.5 at 652 keV.

3.2.3 Peak Shape and Resolution

Many sources of random fluctuation in the charge creation, collection and pulse processing lead to a Gaussian shape of the peaks. Sometimes the peak does not exactly have a Gaussian shape but has a so called tail on either side. These kind of peaks can be modeled with a modified Gaussian shape. If a Gaussian function is fitted to the peak, the fit can be called a Gaussian fit. A Gaussian fit is shown in Figure 3.6.

The width of a peak is usually characterized by its *full width at half maximum* (FWHM). It tells the width of a peak at half of its maximum amplitude. This definition can be applied to all peak shapes. For a Gaussian peak shape, the standard deviation σ is linked to FWHM by

$$\mathrm{FWHM} = 2.355 \cdot \sigma. \tag{3.6}$$

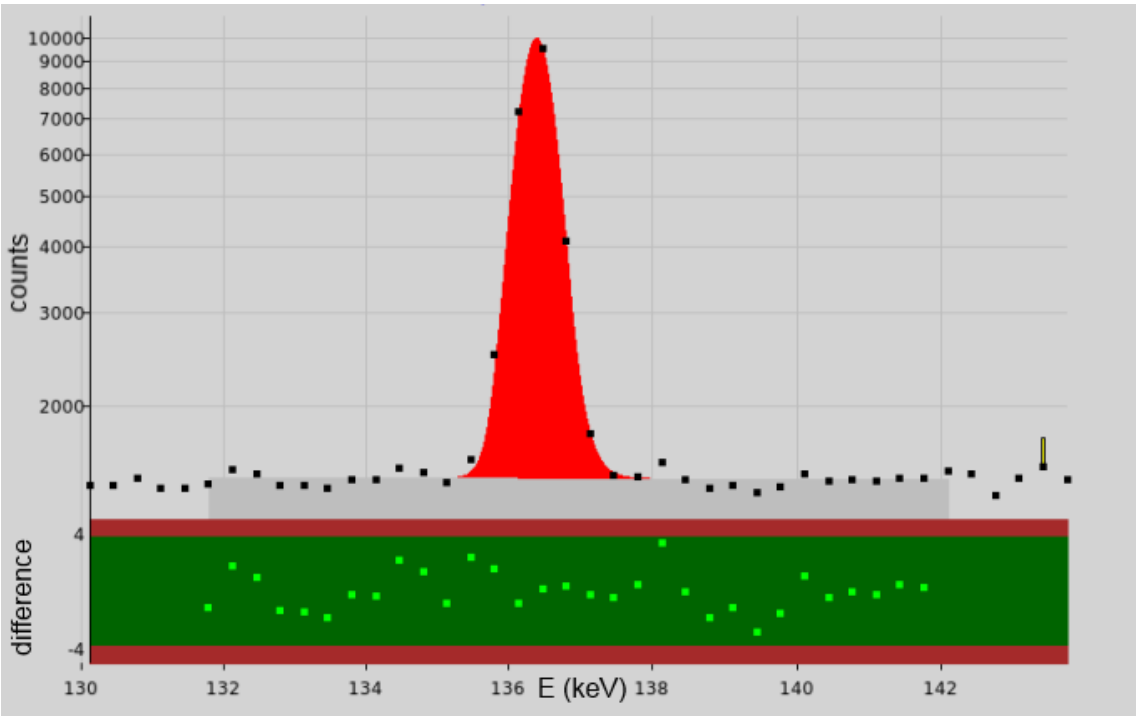

Figure 3.6. A Gaussian fit to a peak. The dark gray area is the baseline. The bottom part shows the difference between the fit and the count in each channel in standard deviations.

Other definitions for a peak width are full width at fifth maximum (FWFM) and full width at tenth maximum (FWTM), for example.

The FWHM increases with energy. For Canberra's BE5030P BEGe detector B6 at STUK the FWHM values given by the manufacturer are 0.48 keV at 5.9 keV, 0.72 keV at 122 keV and 1.80 keV at 1332 keV. A small peak width is preferable since it decreases complications arising from overlapping peaks.

3.2.4 Activity Calculation

The area of a full energy peak is proportional to the number of gamma rays emitted in the sample. The area is given by the equation

$$N_p(E) = N_\gamma(E)\varepsilon(E) = A \cdot I(E) \cdot t \cdot \varepsilon(E), \tag{3.7}$$

where N_γ is the number of photons emitted with energy E, A the activity of the radionuclide in question, I the photon emission intensity, t the data acquisition time and ε the full energy peak efficiency (FEPE) of the detector. FEPE is the fraction of the emitted photons contributing to the full energy peak. If an index i is given for each peak in the spectrum, the above equation can be written as

$$n_i = A \cdot I_i \cdot \varepsilon_i, \tag{3.8}$$

where $n_i = N_p(E)/t$ is the count rate of the peak. From this, the activity of the nuclide is

$$A = \frac{n_i}{I_i \cdot \varepsilon_i}. \tag{3.9}$$

If a nuclide has more than one peak, all the peaks can be used in activity calculation.

The area of a peak can be calculated in two different ways. One method is to sum the counts from each channel of the peak and subtract the baseline. This method is very simple, but the problem is which channels to include in a peak. Usually the distance between the upper and lower channel of a peak is 2-3 times FWHM [6]. This definition becomes problematic when two peaks are close to each other.

The other method is to fit a Gaussian function

$$G(E) = G \cdot e^{-\frac{(E-E_0)^2}{2\sigma^2}} \tag{3.10}$$

to the peak, where G is the peak amplitude, E_0 peak centroid energy and σ the standard deviation of the function. The baseline is subtracted from each channel before fitting. The area of a peak is then

$$N_{p,i} = \sqrt{2\pi}G\sigma. \tag{3.11}$$

Tailing can be included in the fit. The areas for overlapping peaks can be calculated by making a fit for both peaks. This way, the areas of almost completely overlapping peaks can be calculated.

The baseline can be subtracted by assuming it to be linear between the upper and lower channel of a peak. Then the shape of the background is a trapezoid and its area is

$$N_{b,i} = \frac{n_C(C_U + C_L)}{2}, \tag{3.12}$$

where n_C is the number of channels in the peak, C_U is the upper and C_L the lower channel count. However, the background has fluctuations from channel to channel. More stable estimation of the background is achieved by taking the upper and lower channel counts to be a mean of some number of channels, usually 3–5, before and after the peak [6]. More complex baseline definitions can also be used.

Uncertainty estimate for the summing method can be written as

$$\delta N_{p,i} = \left(\sum_{i=L}^{H} C_i + \frac{n_C^2(C_U + C_L)}{4} \right)^{\frac{1}{2}} \tag{3.13}$$

if the count in each channel is assumed to have a Poisson distribution. From this equation it can be seen that the baseline increases the uncertainty of the peak area. For a Gaussian fit, the uncertainty estimation is more complicated. Without taking into account the uncertainty of the baseline subtraction and the difference between summed and fitted peak area, the relative uncertainty is

$$\frac{\delta N_{p,i}}{N_{p,i}} = \left(\frac{\delta\sigma^2}{\sigma^2} + \frac{\delta G^2}{G^2} + \frac{\mathrm{cov}(\sigma, G)}{\sigma G} \right)^{\frac{1}{2}}, \tag{3.14}$$

where $\mathrm{cov}(\sigma, G)$ is the covariance between σ and G [6].

Radioactive nuclides in the environment form peaks in the spectrum. Contribution of this radiation is known from background measurements and it can be subtracted from the peak area. This, however, increases the uncertainty of the peak area and therefore the spectrum should have as low a background as possible.

3.2.5 Correction Factors

When calculating the count rates, using the real measurement time leads to systematic errors because of the dead time. Instead, the data acquisition time, also known as the *live time*, is defined as measurement time minus the dead time. However, correcting for the dead time increases uncertainty. The relative uncertainties of the dead time correction factors can be as large as 20–30% and therefore the count rate should be kept moderate [6]. As a rule of thumb, dead time should not exceed 10% of the measurement time.

When the activities are calculated for a reference date that is not the measurement date, the decay of the radionuclides has to be taken into account. This effect can be calculated from the exponential decay formula and the correction factor is

$$c_t = \frac{A_0}{A_m} = \exp\left(\frac{\ln(2)(T_m - T_0)}{t_{1/2}} \right), \tag{3.15}$$

where T_m is the measurement start time, T_0 the reference date, A_m the activity at the measurement start time, A_0 the activity at the reference date and $t_{1/2}$ the nuclide half life. The uncertainty to the result caused by this correction is usually insignificant compared to other sources of uncertainty. If a nuclide has a short half life, its decay during the measurement has to be corrected for when calculating the activities.

If a plate of material is placed between the source and the detector, the plate absorbs part of the gamma-rays. For monochromatic photons arriving at the plate perpendicularly, the attenuation for thickness x is according to Beer-Lambert absorption law

$$\frac{\Phi_x}{\Phi} = e^{-\mu(E)x} = e^{-\frac{\mu(E)}{\rho}\rho x}, \tag{3.16}$$

where Φ is the photon flux before and Φ_x after the plate, $\mu(E)$ the linear and $\mu(E)/\rho$ the mass attenuation coefficient. Equation (3.16) gives the attenuation only for collimated sources or sources far away from the detector. The attenuation depends on the energy of the photon. The more energetic the photons are, the larger fraction of them penetrate through matter.

Radiation originates randomly inside the volume source. Therefore the attenuation inside the sample must be corrected for if the sample differs from the calibration source. An estimate for a self attenuation correction factor can be obtained by integrating equation (3.16):

$$c_x(E) = \left(\int_0^x e^{-\mu(E)x} dx\right)^{-1} = \frac{\mu(E)}{1 - e^{-\mu(E)x}}. \tag{3.17}$$

Same assumptions are used here as for equation (3.16) and therefore the correction factor is not valid for sources near the detector. A more realistic self attenuation correction can be calculated with computational methods.

3.2.6 True Coincidence Summing

The decay scheme of ^{60}Co is shown in Figure 3.7. After the β^- decay, 99.88% of the daughter nucleus are on the energy level of 2505.7 keV. This states decays practically every time through the 1332.5 keV state to the ground state. Hence, for practically every decay of ^{60}Co, there will be two emitted gamma-rays with energies 1173.2 keV and 1332.5 keV. Since the half lives of both states are on the order of picoseconds, these events can be thought as simultaneous when compared to the time scale of the charge collection in a Ge detector.

The directions of these two photons are random and are thought as independent of each other [2]. There is a possibility that both photons emitted in a single decay are detected with a Ge detector. The resulting pulse contributes to neither of the FEPs and therefore the count rates are smaller than in the case of a single emission. This

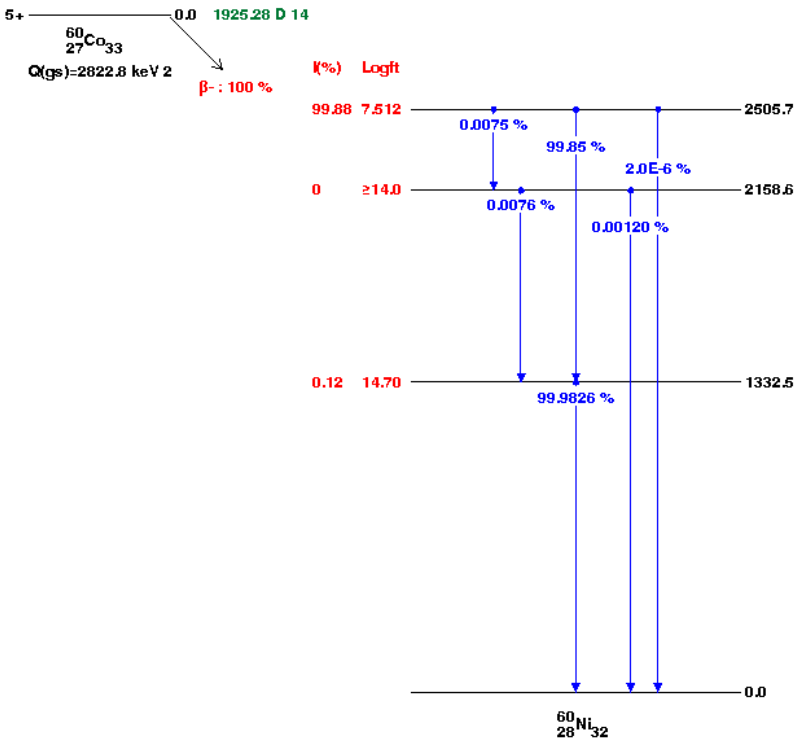

Figure 3.7. Decay scheme of ^{60}Co. I tells the percentage of direct decay to the level. The level energies in keV are on the right written in black. Source: http://www.nndc.bnl.gov/nudat2.

effect is called *true coincidence summing* (TCS). TCS is independent of the activity of the nuclide.

To calculate the TCS correction factors, one needs to know the full energy peak efficiency $\varepsilon(E)$ and the *total efficiency* $\eta(E)$. The total efficiency is defined as the probability of detecting a gamma ray with energy E. This means the probability that the gamma-ray leaves any of its energy in the active volume of the detector, not necessarily all of its energy.

For a ^{60}Co point source, the TCS correction factor is

$$c_{\mathrm{TCS},1} = \frac{\varepsilon_1}{p_{\mathrm{FEP},1}} = \frac{\varepsilon_1}{\varepsilon_1(1-\eta_2)} = \frac{1}{1-\eta_2}, \tag{3.18}$$

where the index 1 refers to the photon with energy 1173.2 keV, index 2 to that of 1332.5 keV and $p_{\mathrm{FEP},1}$ is the probability of the 1173.2 keV gamma-ray contributing to the full energy peak. The same is true if the indexes are switched. ^{60}Co is one of the most simple cases regarding the TCS correction factors.

In other cases, the emission probabilities of the different photons x_{ik} have to be taken into account. For any transition $i \to k$ the TCS correction coefficient can be presented as the ratio of the peak count rate without coincidence summing to the

observed rate, or

$$c_{\mathrm{TCS},ik} = n^*_{ik}/n_{ik}. \tag{3.19}$$

The count rates can be written as

$$n^*_{ik} = L_i a_{ik} \tag{3.20}$$

and

$$n_{ik} = K_i A_{ik} M_k. \tag{3.21}$$

The factors are defined as

$$L_i = X_i + \sum_{n=i+1}^{m} L_n x_{ni}, \tag{3.22}$$

$$a_{ik} = \frac{x_{ik}\varepsilon_{ik}}{1+\alpha_{ik}}, \tag{3.23}$$

$$K_i = X_i + \sum_{n=i+1}^{m} K_n b_{ni}, \tag{3.24}$$

$$b_{ik} = x_{ik}\left(1 - \frac{\eta_{ik}}{1+\alpha_{ik}}\right), \tag{3.25}$$

$$A_{ik} = a_{ik} + \sum_{j=k+1}^{i-1} a_{ij} A_{jk}, \tag{3.26}$$

$$M_k = \sum_{j=0}^{k-1} b_{kj} M_j, \quad M_0 = 1, \tag{3.27}$$

where X_i is the percentage of direct decay to the level i, m is the highest energy level and α_{ik} is the total conversion coefficient of transition $i \to k$ [7]. The uncertainties of the TCS correction factors are too complex to calculate because of correlations that are difficult to estimate.

After correcting for the effects discussed, equation (3.9) becomes

$$A = \frac{n_i}{I_i \cdot \varepsilon_i} \cdot c_t \cdot c_x \cdot c_{\mathrm{TCS}}. \tag{3.28}$$

The count rate is calculated with the live time. Note that any of the correction factors can be equal to or less than one.

3.3 Calibration

The amplification of the preamplifier signal is adjusted so that the channel number corresponds to a wanted energy. This is called the *energy calibration*. The channel-energy dependence is nearly linear and therefore it is enough to calibrate the energy with a couple of points. One method of doing the energy calibration is to first measure a calibration source with one nuclide, adjust the energy for one peak and then check that other peaks of the same source or another one are in place. The energy calibration has to be checked regularly since the amplification experiences drift over time.

In *full energy peak efficiency calibration* the full energy peak efficiency ε is determined for a measurement geometry in a wide energy range. The result is a FEPE curve, example of which is shown in Figure 3.8. The calibration can be done either experimentally, computationally or a combination of these methods can be used. In the computational method, the detector is modeled with a Monte Carlo software and the efficiencies are simulated. The problem with this method is the accurate description of the detector and the sample. In the experimental method, calibration sources where the activities of the nuclides are known are used. The efficiencies for the gamma energies emitted by the sample can be calculated by modifying equation (3.28):

$$\varepsilon_i = \frac{n_i}{I_i \cdot A} \cdot c_t \cdot c_x \cdot c_{\mathrm{TCS}}. \tag{3.29}$$

the FEPE curve is fitted using values calculated with equation (3.29). If the sample geometry in the measurements is similar to the calibration sample, or the sample is thin, the self attenuation correction does not need to be calculated. The fitting of the curve is not necessary if the detector is used to measure only nuclides present in the calibration source. In this case, the TCS correction need not to be done since the factors would cancel out in the activity calculation.

It is important to have sufficient number of FEPE values with proper energies to fit the FEPE curve accurately. From Figure 3.8 it can be seen that after approximately hundred keV the curve is nearly linear on the log-log scale. The curve at lower energies is clearly nonlinear and therefore the peaks used in the efficiency calibration should be more densely spaced at low energies.

The calibration nuclides should emit only one photon to inhibit complications arising from TCS. However, at the energies above 1 MeV such nuclides are not available and nuclides emitting photons with different energies have to be used. Such nuclides are for example ^{88}Y and ^{60}Co. TCS can be problematic at lower energies too, especially if the dead layer of the detector is thin. Thick dead layer stops most of the x-rays produced in electron capture reducing their contribution to TCS. The activity of the source should be low enough not to cause significant dead time and pulse pile up.

The FEPE curve is fitted by choosing a fitting function and then making a least

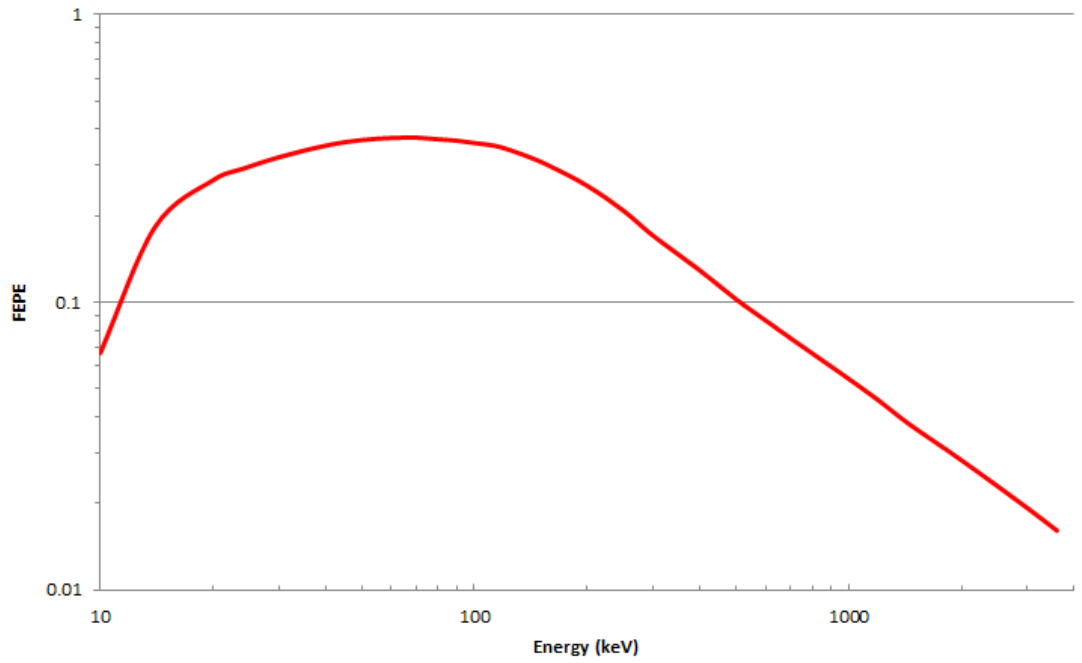

Figure 3.8. FEPE curve for BEGe detector B6 at STUK.

squares fit to the calculated FEPE values. The most common function is a logarithmic polynomial

$$\log(\varepsilon) = \sum_{i=1}^{n} a_i \log\left(\frac{E}{E_0}\right)^{i-1}, \tag{3.30}$$

where E_0 is an arbitrary reference energy and a_i are the fitting parameters [1, 6, 8]. The polynomial can be fitted separately for low and high energies. Other fitting functions can be found for example in references [1, 8, 9].

If the detector is used to measure nuclides that emit gamma rays with multiple energies, the TCS correction factors must be calculated. From equations (3.19)–(3.27) it can be seen that in order to calculate the TCS correction factors one must know the total efficiencies at the energies of the transitions. Therefore a *total efficiency calibration* is needed.

Usually only nuclides emitting photons with one energy are used in the total efficiency calibration. The nuclides should also not emit electrons with energies larger than few hundred keV. Firstly, the count rate in the whole spectrum caused by the photons n'_{tot} needs to be calculated. This is done by summing all the counts in channels from the lower limit of the spectrum to the right edge of the peak, dividing the sum with the measurement time. The background count rate in the same channel range is then subtracted. One could sum the counts in the whole spectrum, but since the calibration nuclide can not cause counts on higher energies than the peak itself, adding these channels would only increase uncertainty. If the nuclide emits x-rays, the area of these should be subtracted too. Also, the intensity of these x-rays

should be low compared to, and not in coincidence with the gamma ray. The total efficiency can be calculated with

$$\eta_i = \frac{n'_{i,\mathrm{tot}}}{I_i \cdot A}, \tag{3.31}$$

where i refers to the nuclide in question.

The total efficiency for a ^{60}Co point source can be approximated even though two gamma rays are emitted in a single decay. The cobalt atom is assumed to emit only the 1173.2 keV and 1332.5 keV photons and both of them are emitted in every decay. The count summing interval ranges from the lower limit of the spectrum to the right edge of the sum peak. If a pulse is formed by interactions of the two photons, then only one pulse is registered in the spectrum instead of two. This leads to an underestimation of the total number of counts in the spectrum.

This effect can be corrected by assuming that both photons have the same total efficiency η. Then, the probability that both photons are detected is η^2. The probability that neither of the photons are detected is $(1-\eta)^2$ and the probability that one or both of the photons are detected is

$$1 - (1-\eta)^2 = 2\eta - \eta^2. \tag{3.32}$$

Therefore the fraction of sum pulses from all the pulses that are detected is

$$p(\mathrm{sum}) = \frac{\eta^2}{2\eta - \eta^2} = \frac{\eta}{2-\eta}. \tag{3.33}$$

When the sum pulses are taken into account, equation (3.31) becomes

$$\eta = \frac{(1 + p(\mathrm{sum}))n'_{\mathrm{tot}}}{I \cdot A} = \frac{\frac{2}{2-\eta}n'_{\mathrm{tot}}}{I \cdot A}. \tag{3.34}$$

The gamma yield in this case is $I = I_1 + I_2$, where I_i are the gamma yields of the two gamma lines. The solution for equation (3.34) is

$$\eta = 1 - \sqrt{1 - \frac{2 \cdot n'_{\mathrm{tot}}}{I \cdot A}}. \tag{3.35}$$

This approximation of the total efficiency can be used for a volume source too if the total efficiency is nearly constant with respect to the position within the sample.

The energy for which the total efficiency in equation (3.35) is calculated can be the average energy of the two photons, i.e. 1252.85 keV. A better evaluation is obtained by calculating the average energy on log-log scale since the total efficiency curve is linear at high energies. However, this would require information about the slope beforehand. The energies calculated with the two methods do not differ significantly.

A total efficiency curve has to be fitted to the total efficiency points. This can be done with the same methods as the FEPE curve but this is usually difficult because of the small number of nuclides suitable for the total efficiency calibration. Experimental and computational methods have been developed to overcome this problem.

4 Computational Methods

In practice Computational methods are always needed in the analysis of the results in gamma-ray spectrometry. The areas of the peaks, self absorption corrections etc. could be calculated by hand but this would be difficult and time consuming. Therefore programs that do the analysis fast and reliably have been developed. Computational methods are also needed in the efficiency calibrations if the TCS correction factors have to be calculated.

4.1 The Monte Carlo Method

Monte Carlo (MC) simulations are a very useful and often necessary tool in gamma-ray spectrometry. The method is based on simulating the physical behavior of radiation quanta in matter using random numbers. When the number of simulated quanta is large and therefore fluctuations average out, properties of the system can be determined. If not mentioned otherwise, the following discussion considers only x-rays and gamma-rays.

An important part of the simulation is an accurate description of the measurement system. The system can be considered to consist of various objects that have different characteristics, for example, sample, container, detector window, dead layer etc. When a decay of an atom occurs in a randomly selected position inside the sample, the resulting photon or photons are given a random direction. The distance to the surface of the next object in the direction of a photon λ is calculated. An interaction occurs during this path length if

$$\lambda_i = -\frac{\ln s}{\mu_{\text{tot}}} < \lambda, \tag{4.1}$$

where s is a random number from a uniform distribution between 0 and 1 and μ_{tot} is the linear attenuation coefficient for the material of the current object and the energy of the photon [10]. λ_i is the length that the particle travels without interactions. If $\lambda_i > \lambda$, then no interaction happens in the current object. In that case, the photon is moved to the crossing point to the next object, the path length in the object is calculated and the condition in equation (4.1) is checked with μ_{tot} of the object and a new random number s.

The total linear attenuation coefficient can be written as

$$\mu_{\text{tot}} = \mu_{\text{photo}} + \mu_{\text{Compton}} + \mu_{\text{pair}}, \tag{4.2}$$

where the coefficients on the right side are linear attenuation coefficients for photoelectric effect, Compton scattering and pair production. When the condition in equation (4.1) holds, the type of the interaction is determined by

$$\begin{aligned} 0 < s < \frac{\mu_{\text{photo}}}{\mu_{\text{tot}}} & \qquad \text{photoelectric effect,} \\ \frac{\mu_{\text{photo}}}{\mu_{\text{tot}}} < s < \frac{\mu_{\text{photo}} + \mu_{\text{Compton}}}{\mu_{\text{tot}}} & \qquad \text{Compton scattering,} \\ \frac{\mu_{\text{photo}} + \mu_{\text{Compton}}}{\mu_{\text{tot}}} < s < 1 & \qquad \text{pair production.} \end{aligned} \tag{4.3}$$

Note that s does not have the same value as in equation (4.1). The elastic Thomson scattering of the photons can be taken into account in the simulations but the effect is minuscule.

For interactions that happen inside the detector active volume, the energy losses are put in memory. If the photon interacts through photoelectric effect, it is deleted and an electron with the energy of the photon is created. Usually, however, it is assumed that the electron loses all its energy in a very small volume. Therefore it is sufficient to think that the photon transfers its energy to the object it is currently in. This assumption is validated in refs. [1, 10, 11]. Leaving out the electron interactions saves time while performing the simulations.

In Compton scattering, the photon is deleted and a secondary photon created. The direction of the secondary photon is determined with a random variable from a probability distribution of Compton scattering. Again, the energy of the ejected electron can be assumed to be deposited in the current object [10].

If the photon interacts through pair production, the photon is deleted and two photons with energy $m_e c^2$, or 511 keV, are created at the same position. The direction of one of the photons is chosen at random and the direction of the other is the opposite. Energy deposited to the current object is the energy of the photon minus 1022 keV. There is a cut off energy for every particle in the simulation. If the energy of the particle is below this limit, it will be deleted and the remaining energy is assumed to be left in the current object.

If more than one photon was created during the processing of one emission in the sample, the same procedure is done for each of them until the photons have escaped the system or deposited all of their energy. Then the energy deposited in the detector active volume can be summed from the energies deposited in individual interactions. This information can be used, for example, in simulating spectra.

The information about the deposited energy can also be used in simulation of the full energy peak and total efficiencies. The total efficiency for photons with energy E in a sample can be attained by simulating the behavior of a large number of these photons originating randomly inside the sample. The photons are processed individually. The number of photons that lead to deposition of energy inside the detector active volume is saved in memory and this number is compared to the number of emitted

photons. The same procedure applies to FEPE except the number of events leading to the full deposition of energy E inside the detector active volume is counted.

When the efficiencies are simulated for multiple energies, the efficiency curves can be fitted. The energy intervals can be arbitrarily small but usually they are spaced more densely at low energies. The curve can be interpolation between the efficiency points, especially when the number of points is large, or other fitting methods can be used.

The statistical uncertainty of the simulations is inversely proportional to the square root of the number of simulated photons and therefore it can in principle be reduced to an arbitrary small value. The simulation time is four times longer when the statistical uncertainty is halved. The uncertainties of the nuclide data, linear attenuation factors and the model of the system have to be taken into account also. The attenuation and nuclide data may contain strong correlations [11]. The detector parameters provided by the manufacturers can differ significantly from the real ones [12]. Therefore the parameters in Monte Carlo simulations should be adjusted with results from measurements.

The dead layer of the detector crystal is not a layer of uniform thickness. The dead layer in a MC model usually has a constant thickness and the thickness is fitted with experimental efficiencies. The same may apply to window thickness. The dead layer is not constant in another regard. The amount of collected charge does not suddenly go from full collection to no collection but changes gradually as a function of depth. Therefore the dead layer of the MC model should be thinner when simulating total efficiencies and thicker in FEPE simulations [13].

4.2 MCNP

MCNP is a Monte Carlo simulation software used to model radiation transport. The name is an abbreviation of Monte Carlo N-Particle. The version used in this thesis was 6.1 [14]. MCNP has various fields of use including high energy physics, radiation therapy, dosimetry and detector modeling, for example. Because of the large field of applications, MCNP does not have a user interface and therefore defining the model is more difficult than with softwares dedicated to more specific types of models. However, the use of MCNP can not be described as difficult. People with little background in programming should learn to use it quickly, especially if a tutor is available.

The model in MCNP is constructed with cells. These cells are defined by intersections and unions of volumes restricted by surfaces. A material or a vacuum is defined for each cell and there can be no undefined areas inside the system. The density of a material is not calculated and it must be given by the user. This allows, for example, the determination of the effects of cross section uncertainties [11]. The density of materials depend on temperature and when modeling a germanium

detector the parts inside the end cap are denser than in room temperature. Each cell is also given an importance value that defines whether the particle transport continues in it or not. If the importance for a particle entering the cell is zero, it is deleted and is thought to escape the system.

The surfaces can be defined one at a time but this is time consuming in the case of simple geometries. Therefore some basic objects have been programmed into the system. For example, the six sides of a cube need not be defined separately but can be build with one line of code containing information about the position, orientation and the lengths of the sides of the cube. A cylinder is constructed by giving the position of the center of the end of the cylinder, the vector from that point to the center of the opposite side and the radius of the cylinder. For example, a 10 cm high vertical cylinder with radius of 5 cm on top of the x-y plane is constructed with

```
n RCC 0 0 0  0 0 10  5
```

where n is the label of the surface (integer), RCC defines that the surface is a cylinder, the first three numbers are the coordinates of the bottom of the cylinder, the next three the vector defining the direction and length of the cylinder and the last number the radius of the cylinder.

The materials are constructed by giving the fraction of elements or nuclides in the material. Water can be constructed with

```
mn 1000 2 8000 1
```

where mn is the label of the material, for example, m3, the first number in 1000 defines that the atom is hydrogen and the first number in 8000 that the atom is oxygen. The three zeros tell that the atomic mass is the average of isotopes found in nature. The 2 and 1 after the 1000 and 8000 tell that there is two hydrogen atoms to every oxygen atom. If a certain isotope needs to be used, the three zeros are changed to the mass number of the isotope. For example

```
mn 82210 1
```

defines a material made solely of ^{210}Pb (atomic number 82, mass number 210).

The source in the model is defined by giving its position, dimensions, type of emitted particles, energy and distribution. There can be multiple samples and one sample can have various types of particles and different energies. If attenuation inside the sample needs to be taken into account, the sample material needs to be defined in a cell and the sample defined so that it has the same dimensions. The source energies can not be defined by giving a radioactive nuclide but the values need to be defined by the user. In addition, simultaneous emission of two particles is not possible.

The information about the simulation that will be given in the output is defined with *tallies*. The only tally used in this thesis is the pulse height spectrum, or tally 8. After radiation transport, the program gives the number of counts in user defined energy intervals, or bins. The unit of the spectrum is pulses per source particle.

When used for efficiency calibrations of a gamma spectrometer, the pulse height spectrum in the detector active volume is calculated. The total efficiency values are obtained by defining energy bin between 1 keV and some energy larger than the photon energy. The choice of the upper limit is arbitrary because there is no background and the count rate at energies larger than the photon energy is zero. Because the pulse height spectrum is given per source particle, tally 8 gives the total efficiency without further processing. The photons cause a spectrum where the width of the full efficiency peak is zero. Therefore in the FEPE simulation, the energy bins need to be defined so that a bin has a lower limit slightly below and upper limit above the photon energy to reduce the contribution of Compton continuum to the bin. With a bin width of 1 keV the contribution of the continuum is less than 0.1%. As with total efficiencies, tally 8 gives the FEPE as the pulse height in the bin if the effect of Compton continuum is insignificant.

The problem termination can be done by setting the number of histories (i.e. number of particles emitted by the sample) to be simulated, a simulation time or a precision limit. The counting time can be reduced by *variance reduction*. It means that the properties of the source particle are weighed so that more particles contribute to the problem at hand. For example, the photons emitted from a flat sample on top of a HPGe detector have a very small contribution to the efficiency calculations if the photon is not emitted towards the detector. Therefore more photons that are emitted towards the detector can be simulated to reduce the counting time. Use of the variance reduction should be kept to a minimum because of possible unnoticed contributions to the uncertainties of the simulations.

MCNP contains a vast amount of different options for the simulations and the description in this chapter gives only a glimpse of the possibilities. The use of the user manual is restricted but the first volume of the MCNP5 manual containing an overview and theory is freely available [15].

4.3 UniSAMPO Shaman

At STUK, the program used to calculate the peak areas in spectra of the environmental samples is *UniSAMPO* (US). US fits a Gaussian function of equation (3.10) to the peaks and determines the peak areas. There are different options for the shape of the background and tails can be used in the fit. If two or more peaks are close to each other, they can be fitted simultaneously to take their overlap into account. The analysis of spectra can be fully automated or it can be modified manually. Opening screen of US can be seen in Figure 4.1.

US can read various types of inputs, one of which is a phd file. A phd file includes sample description, live and real acquisition time of the measurement, energy, resolution, FEPE and total efficiency calibration data and the spectrum data. The fits to the calibration points are done by US. The resolution calibration is not needed if the spectrum contains enough peaks. In that case US can make a peak shape fitting

based on the calculated parameters of the peaks. The energy calibration can also be done in US. If the energies are off by only few keVs, the peaks can be fitted to energies of known nuclides. Calibration points in every calibration, except the total efficiency calibration, can be added, changed or deleted by the user.

The tail shape calibration is calculated from the peaks. The tail parameter is defined as the distance from the peak top to the beginning of the tail. At the beginning of the tail the fitting function changes smoothly from a regular Gaussian of eq. (3.10) to the tail function

$$G(E) = Ge^{\frac{E_j(2E_0-2E+E_j)}{2\sigma^2}}, \tag{4.4}$$

where G is the peak amplitude and E_j is the tail parameter [16]. E_j is usually not equal for high and low tails. After calculating the low and high tail parameters, US makes a fit to the calculated points. The fitting function is linear by default but it can be changed.

The baseline of the peak can be set to be either linear or parabolic. The user can also set a step in the baseline. This is useful when the height of the baseline differs on opposite sides of a peak. When multiple peaks are fitted simultaneously, the drop during each peak is proportional to the height of the peak [16].

The manual analysis procedure begins with checking the energy and shape calibrations. If the shapes are calculated from the spectra, deleting outliers or clearly erroneous points is usually sufficient. Then the analyst goes through the spectrum and deletes falsely recognized peaks and adds those that were not found. After the

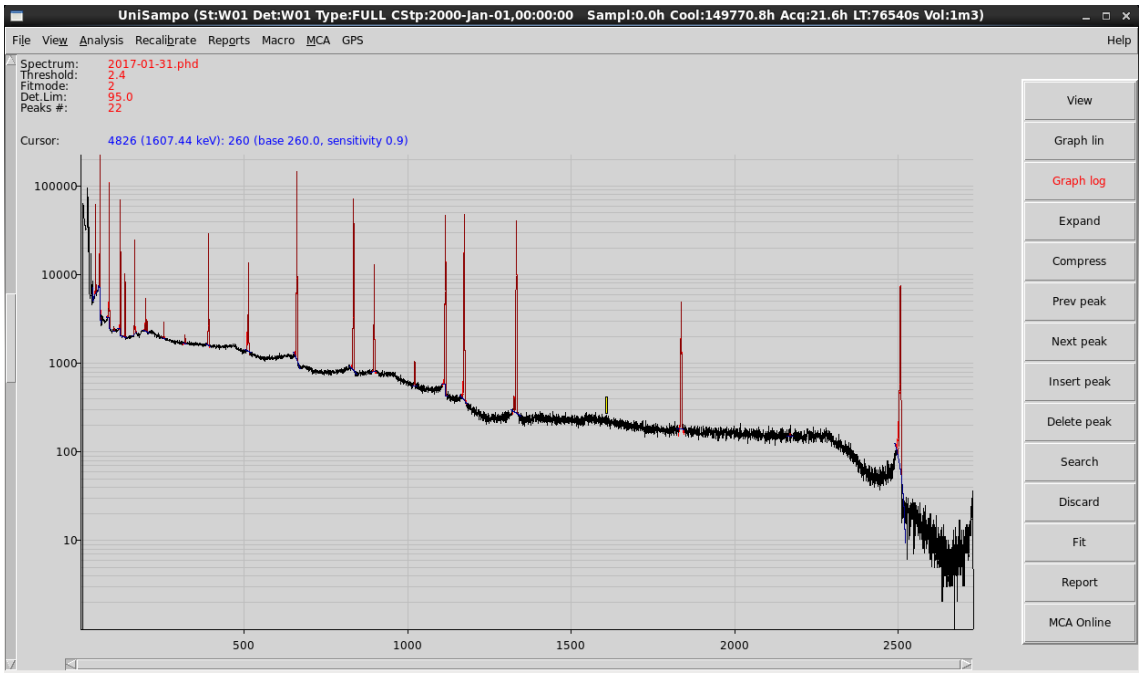

Figure 4.1. Opening screen of UniSAMPO. The fits of the peaks are shown with red lines.

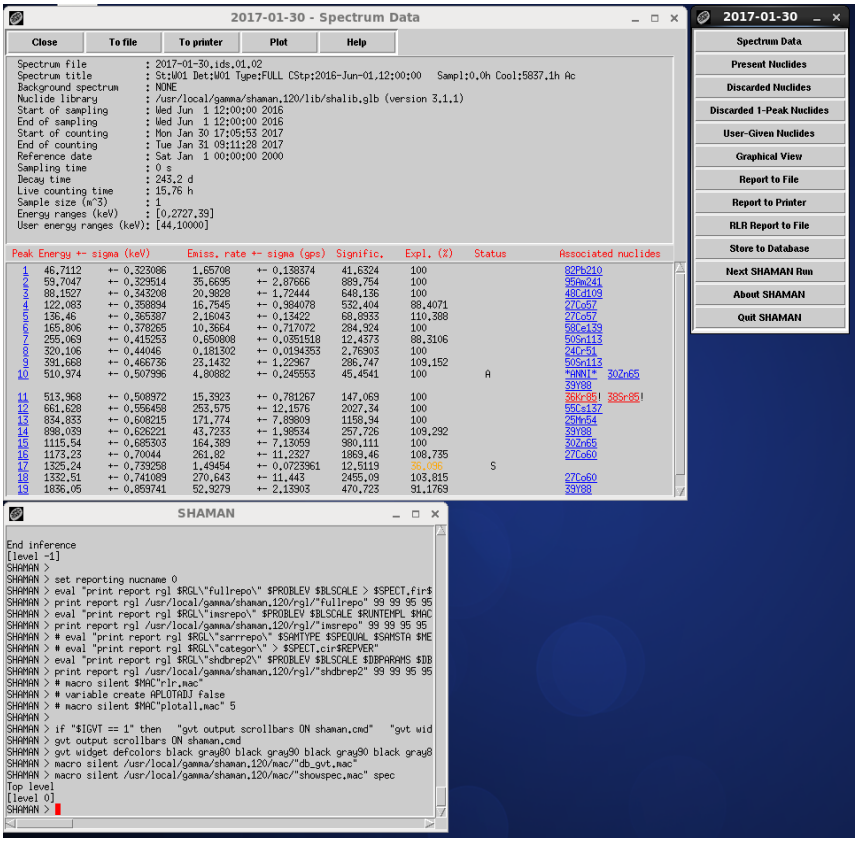

Figure 4.2. Opening screen of Shaman. The upper screen shows information about the measurement and explanations for the peaks. On the right is the main menu and on the bottom a command line of Shaman.

wanted peaks are fitted, the fits are inspected. The analyst can change the fitting interval and set the shape of the baseline. When all the peaks are fitted properly, the *Shaman* analysis is launched.

Shaman (Figure 4.2) is a program designed for nuclide identification from a gamma spectrum. It uses spectra that are already analyzed in a similar way to what was described for UniSAMPO. Shaman calculates the activities, activity concentrations and minimum detectable activities for each identified radionuclide in the spectrum.

If two gamma lines of different nuclides are close to each other, Shaman may not be able to decide the right nuclide or it might give a false identification. The user can drop wrong identifications and add correct ones from a list of discarded nuclides. Shaman has to be run again to update these changes.

To give real activities, corrections discussed in chapter 3.2 need to be taken into account. Shaman uses a more accurate approximation than (3.17) for self attenuation correction. The method was developed at STUK and it is designed for Williams containers (chapter 5.3.1). It assumes that for an infinitesimal layer in a cylindrical

source, the full energy peak efficiency is

$$\varepsilon(z) = f_0 e^{-(f_1 - z f_2)} e^{-\mu z(1+f_3 \exp(-f_4 z))}, \tag{4.5}$$

where z is the distance of the layer from the bottom of the sample, μ the linear attenuation coefficient and f_i the fitting parameters [7]. The efficiency of the sample is obtained by integrating equation (4.5) from zero to the sample height. This correction, however, assumes the mass attenuation coefficient to be constant for every material. This leads to unreliable results, especially for low energies and high Z materials.

Shaman uses the method given in equations (3.19)–(3.27) to calculate the TCS correction factors. The efficiencies are given by US and the nuclide data are from Shaman's own library. The library is collected from different sources, mainly from NUDAT database [17]. NUDAT can be accessed at National Nuclear Data Center (NNDC) website. New data can be added and existing data modified if more reliable information becomes available [7].

Both UniSAMPO and Shaman analysis can be done automatically after the measurement. However, the quality of the peak fits in US and the sanity of the nuclide identifications in Shaman should always be inspected. The US and Shaman analyses are always done together at STUK and they will be referred to as UniSAMPO Shaman, or USS. USS is used in a Linux environment.

4.3.1 Background in USS

The contributions of background peaks need to be subtracted from the spectra of the sample measurements. In USS there are two possible ways to do this. One is to analyze the background spectrum with USS. After fitting the peaks with UniSAMPO, when Shaman is run, it creates a file that can be used as the background spectrum file. The background spectrum file for a detector has to be defined in the setting.

The other method is to make a list of the background peaks. The list includes the energy of the peak, the peak count rate and standard deviation of the count rate. If a peak is found within the given energy tolerance, the count rate in the list is subtracted from the peak.

Shaman subtracts the count rates of the background peaks from the sample spectrum and if the net count rate is less than the detection limit, the peak is marked as a background peak in the reports. If the count rate is larger, Shaman tries to find another explanation for the peak, e.g. gamma rays from a radionuclide. The uncertainty of the count rates for these peaks are

$$\delta n_i = \sqrt{\delta n_{t,i}^2 + \delta n_{b,i}^2}, \tag{4.6}$$

where n_i is the net count rate, n_t the count rate of the peak without background subtraction and n_b is the background count rate of the peak [7].

4.3.2 Uncertainty Analysis in USS

The peak area uncertainty estimate in US takes into account the uncertainties of the fitting parameters (equations 3.10 and 4.4), the baseline and possible background peaks. It does not take into account the quality of the fit. If the shape of a peak differs from the Gaussian, for example, because of a overlapping Compton edge, the peak area might be calculated incorrectly. This extra uncertainty should be added to the uncertainties of the FEPE calibration points.

Even though the uncertainties of the coincidence correction factors can not be calculated accurately, the uncertainty can be estimated. Shaman uses a formula

$$\delta c_{\mathrm{TCS}} = (c_{\mathrm{TCS}} - 1) \cdot 0.1 \tag{4.7}$$

for the uncertainty estimation. There is no physical explanation for this formula and it is a sophisticated guess made by the authors [18].

When a nuclide has multiple peaks in the spectrum, Shaman uses information from all the fitted peaks in the activity calculation. When making the uncertainty estimation, the program assumes that the uncertainties of the activities calculated from single peaks are independent. In general this assumption is incorrect. The efficiencies of the lines can have significant correlations especially if the peaks are close to each other. A more suitable way to calculate the uncertainties is to use uncertainties of the largest peak of the nuclide. This method gives an upper limit for the standard deviation.

USS can not differentiate between uncertainties related to the calibration and those related to the samples. For example, if a calibration is done for a cylindrical container where the sample is very thin, the uncertainties related to the composition of the sample can be insignificant. When a spectrum for a sample, whose height is several centimeters, is measured, the uncertainty related to the composition of the sample can be the source of the largest uncertainty, especially at low energies. The uncertainties of the thick samples can not be taken into account separately but they have to be included in the uncertainties of the efficiencies. This leads to an overestimation of uncertainties for thin samples.

4.4 Other Programs

MAESTRO-32 (later referred to as Maestro) is a multichannel analyzer emulation software made by Ortec (Figure 4.3). The software is used to control the data acquisition, process the data from a MCA and view it on a PC. The version used at STUK is 7.01.

After a measurement is started, Maestro shows the acquired spectrum in real time. Information about peak areas and count rates can be viewed. This is helpful when sufficient counting statistics need to be assured before ending the measurement.

Maestro also shows the energy of the peak and its FWHM. When the measurement is stopped, the spectrum can be saved in various forms. Sum of counts in a user-defined channel range can be calculated from the saved spectra.

The operation of the preamplifier and the shaping amplifier are done with Maestro. The preamp amplification can be set between 0.45 and 32. If the amplification needs to be less than 0.45, it can be lowered with a resistor before the signal reaches the shaping amplifier. The pole zero cancellation can be done manually or automatically. The rise time can be set from 0.8 to 23 µs and the flat top from 0.3 to 2.4 µs. The detector bias voltage control and detector state monitoring are also performed with Maestro.

Gamma-99 is a spectrum analysis software that performs the same functions as USS. The difference is that when calculating peak areas, Gamma-99 sums the pulses in the peak range and subtracts the baseline instead of fitting the peak. The user can change the peak limits and the shape of the baseline if needed. After the peak ranges and the baseline is set, the nuclides are identified and the peak count rates and the activities are calculated.

GESPECOR (Germanium Spectra Correction) is a simulation program used in gamma spectrometry for calculation of efficiencies, self attenuation corrections and

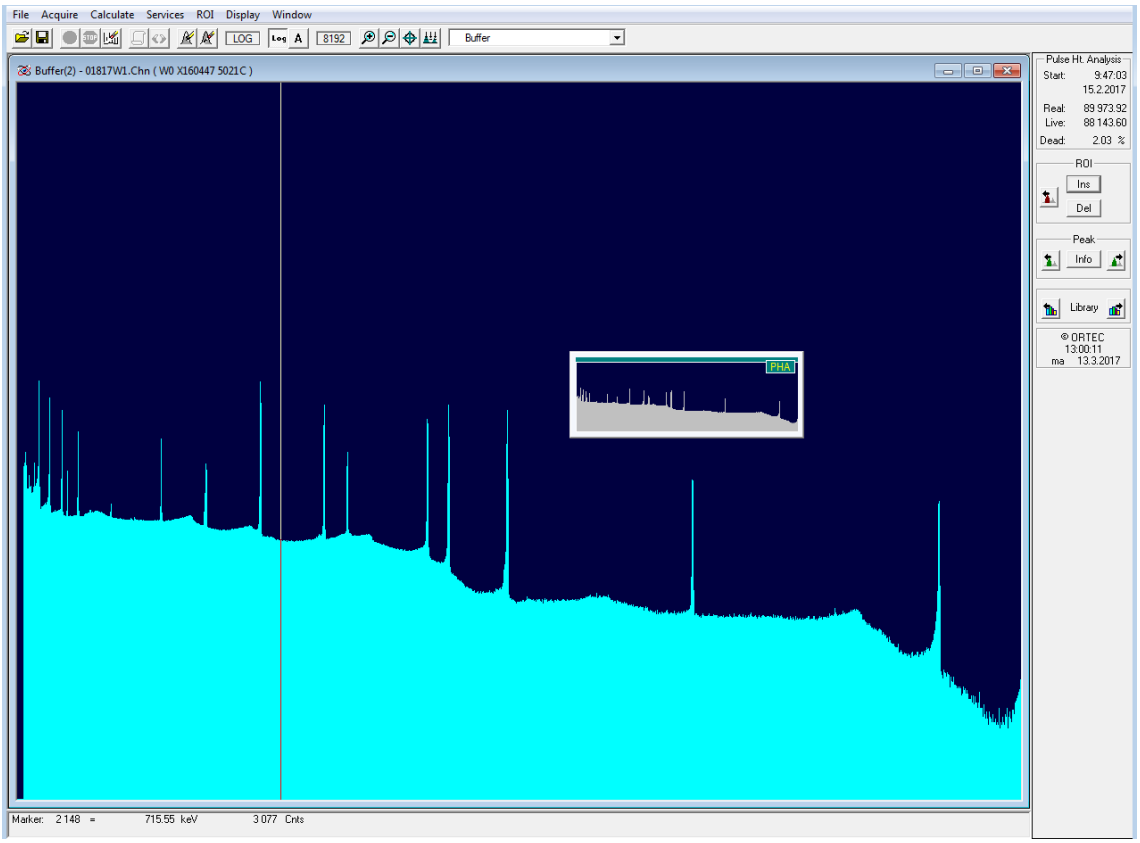

Figure 4.3. Main window of Maestro.

TCS correction factors. GESPECOR uses Monte Carlo methods for the calculations. It has an user interface that is intuitive to use. The detector model can be planar, coaxial or a well detector. The possibilities in constructing the model are not as wide as with the MCNP. For example, the geometry must be cylindrical and dead layer thickness inside the well as well as outside has to be constant. More information about GESPECOR can be found for example in references [13, 19, 20].

5 Description of Measurement Equipment and Samples

This chapter contains the description of the detector, its accessories, measurement electronics and samples. The calibrations were done for three different sample geometries: cylindrical Williams and T containers and a test tube. The geometries are described in this chapter.

5.1 Canberra's Model GSW300 SAGe Well Detector

The Canberra's small anode germanium (SAGe) model GSW300 well detector at STUK is a p-type HPGe detector with a blind hole. The detector is labeled as W1. The preamplifier is attached to the detector and its model is 2002CSL. The detector dimensions given in the detector specification sheet and the initial guesses for the dead layer thicknesses from the datasheet are in Table 5.1 [21]. The detector inside its shield is shown in Figure 5.1.

The thickness of the dead layer and the aluminum window allow spectrometry down to 20 keV inside and to 40 keV outside the well. The high limit is 10 MeV [22]. Therefore the energy range of the detector is sufficient for environmental sample measurements. The 20 keV low limit removes some of the problems with coincidence effects faced with the BEGe detectors whose low limit for detection is below 10 keV.

According to the detector specification sheet, the FWHM is 0.727 keV at 122 keV (^{57}Co) and 1.75 keV at 1332.5 keV (^{60}Co) with 5.6 µs rise time and 1.6 µs flat top. The FWTM is reported as 3.27 keV at 1332.5 keV. The resolution of the SAGe well detector is better than that of coaxial detectors and traditional well detectors [22].

Table 5.1. Detector dimensions from the detector specification sheet and the datasheet.

diameter	87.5 mm	active volume	348 cm^3
height	65.5 mm	distance from window outside	10 mm
well diameter	21 mm	end cap well diameter	16 mm
well depth	40.5 mm	end cap well depth	40 mm
dead layer in well	50 µm	end cap thickness in well side	0.5 mm
dead layer outside well	0.5 mm	end cap thickness in well bottom	1 mm

A contamination cover (Figure 5.1c) was made to protect the detector from possible contamination caused by a sample. A 98 mm long and 47 mm wide piece of 0.15 mm thick transparent foil was cut and rolled around the short side so that it formed a tube that had two layers of foil at every point. The free end was attached with a piece of tape the length of the tube. Then a piece of plastic wrap large enough to cover the bottom of the pipe was cut. The wrap was attached to the bottom of the pipe by folding the edges of the wrap to the side of the pipe and attaching a piece of clear tape around the end of the pipe.

The effect of the tape and the wrap on the attenuation of photons can be assumed to be negligible because of their low thickness. However, the foil was taken into account in the Monte Carlo simulations. A piece of plastic wrap covering the detector is used when measuring samples on top. The effect of this wrap on attenuation is also negligible.

5.2 Shielding, Dewar and Measurement Electronics

The detector is inside a lead shield (Figure 5.1b) to reduce the background. The shield is 16 cm thick on the side and the top is 16 cm thick. The height of the shield is 72 cm on the outside and 39.5 cm on the inside, leaving approximately 16 cm of lead on the bottom. The inner layer of the shield is made of 3.5 mm thick layer of copper to mitigate the emission of x-rays generated by excitation of lead atoms. There is also a 4 mm thick plastic cover inside the shield to prevent contamination of the shield and to reduce the bremsstrahlung radiation originating from the shield. The dipstick is surrounded by two lead tiles to plug the hole made for the dipstick.

The detector is cooled with Canberra's Cryo Cycle II model CCII-V0 dewar (Figure 5.1d). It uses an electric system to cool vaporized nitrogen back to liquid. This makes it possible to use the dewar for years without having to add nitrogen. In addition it will keep the detector cooled for about a week without power. The dewar is lifted on a layer of lead tiles to adjust the detector to the right height and to reduce background originating from radiation below the detector.

Ortec's DSPEC50 signal processing hardware (Figure 5.1e)) was used for signal processing. It contains the pulse shaping amplifier and the multi channel analyzer. It is also used to control the amplification of the preamp and to provide the detector bias voltage and preamp power. The DSPEC can be connected to a PC with a USB or an Ethernet cable.

The DSPEC uses trapezoidal pulse shaping to minimize the effects of ballistic deficit. Rise time and flat top can be adjusted to obtain the best resolution. The MCA system conversion gain, or the maximum channel number, can be set to 512, 1024, 2048, 4069, 8192 or 16384. The lower part of the spectrum can be cut off. This can be helpful when there is considerable noise at low energies. The DSPEC is controlled with Maestro.

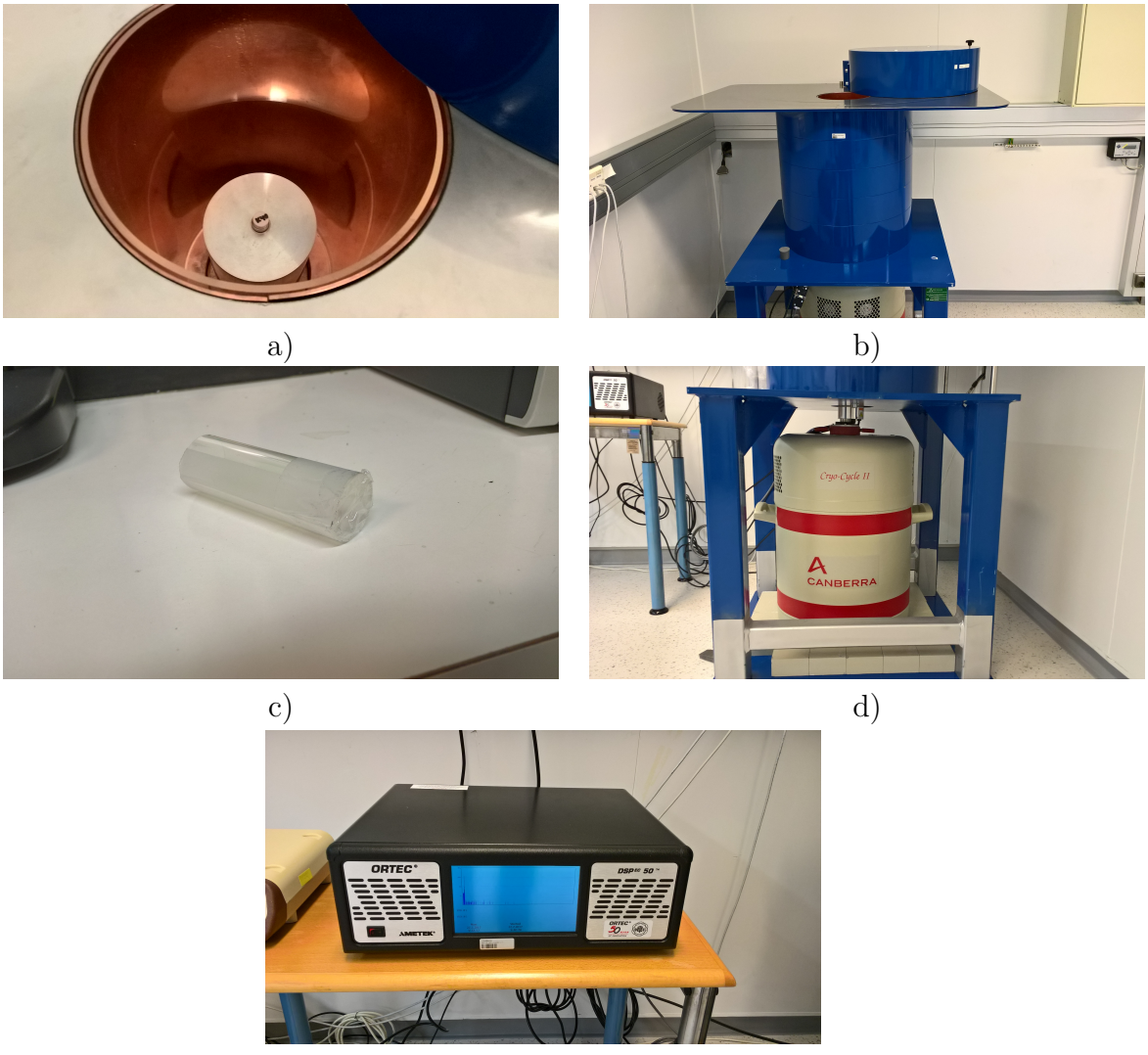

Figure 5.1. a) Canberra's SAGe well detector inside its shield with a sample in the well, b) the shield photographed from outside, c) contamination cover for the well , d) Canberra's Cryo Cycle II dewar and e) Ortec's DSPEC50 signal processing hardware.

5.3 Samples

5.3.1 NPL W0 and T0 Samples

Two certified low thickness filter samples were manufactured by National Physics Laboratory (NPL) in Britain. The diameters of the samples were those of two standard containers at STUK, labeled as the *Williams* and the *T* container. The dimensions of the containers can be seen in Figure 5.2. The measurement geometries are referred to as W0 and T0 and the samples from NPL as NPL W0 and NPL T0.

The zero refers to the low thickness (0.4 mm) of the samples. Thin sources were selected for the calibration to reduce uncertainties caused by self absorption in the samples. The filling height varies when measuring environmental samples and there is no standard filling height. The reference date for the samples is 1st of June 2016.

The samples were prepared by soaking drops of radioactive solution on the filters and putting the filters on bottom of the containers. The drops were spread as homogeneously as possible. The containers were filled with with paper to keep the filters tightly pressed to the bottom. The activities and gamma emission rates on the reference date are given in Tables 5.2 and 5.3. Pictures of the samples can be seen in Figure 5.3. The activity distribution of the samples were determined with imaging plates (Figure 5.4). The radiation excites electrons on a plate and some of these electrons are excited to stable states. These states can be de-excited with light and in the process a photon in the visible wave length region is emitted. The image caused by radiation can therefore be read by scanning the plate with a laser and measuring the amount of photons.

The 136.4 keV gamma-ray of ^{57}Co and 255.2 keV gamma-ray of ^{113}Sn were not included in the certificate provided by the NPL. They were calculated with the information that the yield of the 136.4 keV gamma-ray is 10.68% and 2.11% for the 255.2 keV gamma-ray [17]. The uncertainties of the yields of these nuclides are insignificant and the relative emission rate uncertainties are equal to those of the other gamma energies [17].

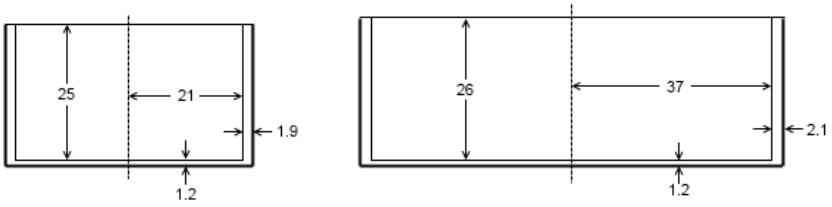

Figure 5.2. Dimensions of Williams (left) and T containers (right) made of polystyrene. All the values are in millimeters.

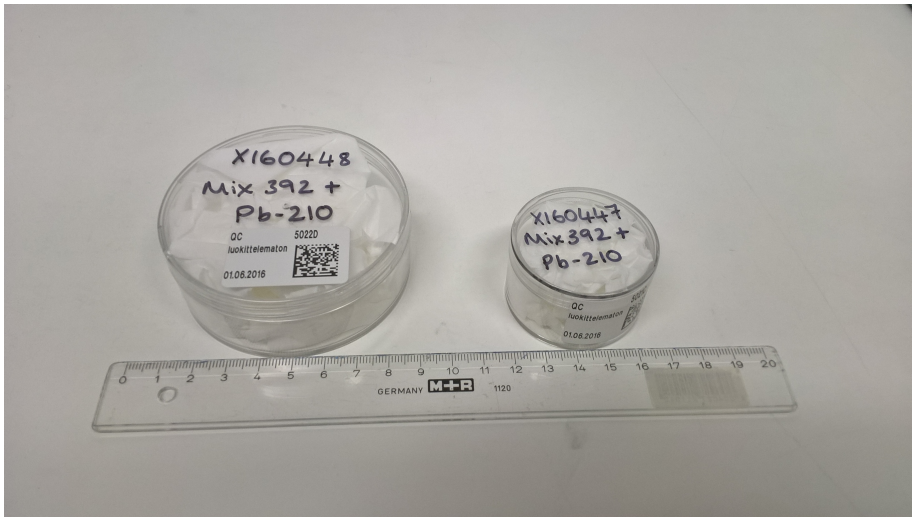

Figure 5.3. W0 and T0 samples manufactured by NPL. The samples are thin filters on the bottoms of the containers. Additional paper was put in the containers to keep the filters pressed to the bottom.

Table 5.2. Nuclides and their half lives, gamma energies, activities and gamma emission rates for the NPL W0 sample on 1st of June 2016. The uncertainty coverage factor is two ($k = 2$).

Nuclide	half life (d)	E (keV)	A (Bq)	δA (Bq)	γ/s	$\delta(\gamma/\mathrm{s})$
Pb-210	8120	46.5	183.8	3.8	7.82	0.22
Am-241	158000	59.5	250.8	4	90.1	1.7
Cd-109	461.4	88.0	1393	53	50.5	2.1
Co-57	271.8	122.1	52.63	0.91	45	0.78
Co-57	271.8	136.4	52.63	0.91	5.6	0.097
Ce-139	137.641	165.9	65.5	1.5	52.3	1.2
Sn-113EC	115.09	255.2	166	2.9	3.5	0.065
Cr-51	27.703	320.1	1057	18	104.6	1.8
Sn-113IT	115.09	391.7	166	2.9	107.9	2
Sr-85	64.85	514.0	204.4	3.5	201.3	3.8
Cs-137	10976	661.7	279.8	4.8	237.8	4.2
Mn-54	312.13	834.8	257.8	3.2	257.8	3.2
Y-88	106.626	898.0	247.5	3.1	232.4	3.1
Zn-65	244.01	1115.5	536.7	9.2	269.5	4.8
Co-60	1925.2	1173.2	299.2	5.2	298.7	5.2
Co-60	1925.2	1332.5	299.2	5.2	299.1	5.2
Y-88	106.626	1836.1	247.5	3.1	245.8	3.1

5.3.2 NPL K40 Test Tube Sample

A radionuclide water solution was ordered from NPL. This solution was used to make a standard sample that can be measured inside the well. The solution was put inside a test tube and diluted to 40 mm filling height measured from the container bottom (Figure 5.5). The sample geometry will be referred to as K40 and the sample made from the NPL solution as NPL K40 sample. The number 40 refers to the filling height. This will be the standard filling height of the environmental samples. The liquid surface is in level with the top of the end cap of the detector. The container is made of polystyrene and the surface of the liquid does not curve as in glass tubes.

The nuclides, their activities and gamma emission rates are presented in Table 5.4. The gamma rates for the 136.4 keV gamma-ray of ^{57}Co and the 255.2 keV gamma-ray of ^{113}Sn were calculated the same way as for W0 and T0 samples. Uncertainties

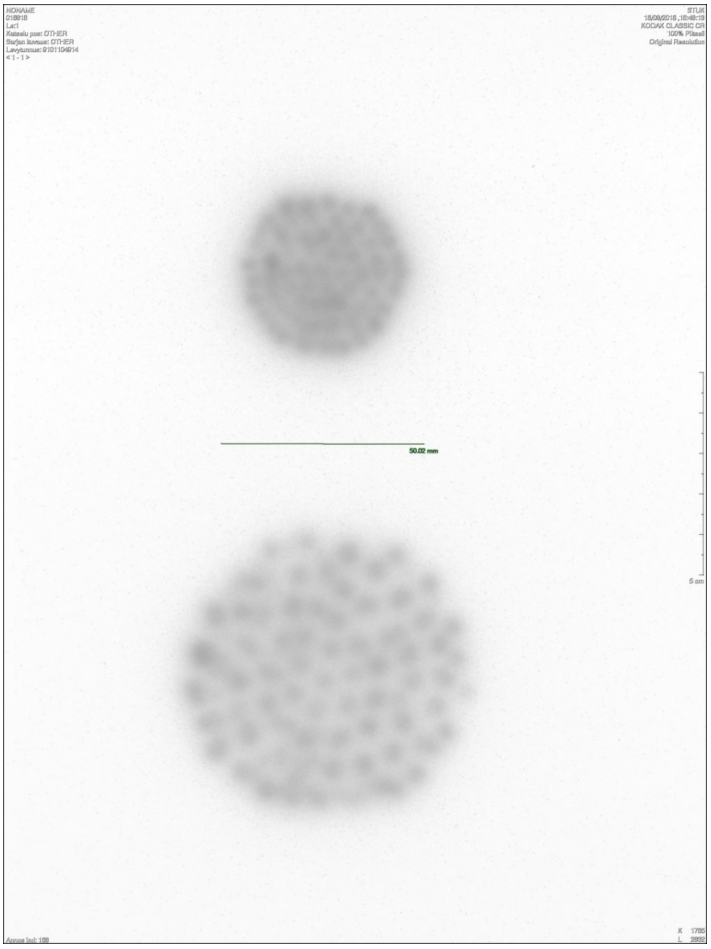

Figure 5.4. An imaging plate picture of the NPL W0 and T0 samples. The horizontal line in the middle is 5 cm long. The darker the area, the more active it is.

Table 5.3. Nuclides and their half lives, gamma energies, activities and gamma emission rates for the NPL T0 sample on first of June 2016. The uncertainty coverage factor is two ($k = 2$).

Nuclide	half life (d)	E (keV)	A (Bq)	δA (Bq)	γ/s	$\delta(\gamma/s)$
Pb-210	8120	46.5	338.2	7	14.38	0.4
Am-241	158000	59.5	372.8	6	133.9	2.5
Cd-109	461.4	88.0	2071	79	75.1	3.1
Co-57	271.8	122.1	78.2	1.4	66.9	1.2
Co-57	271.8	136.4	78.2	1.4	8.4	0.15
Ce-139	137.641	165.9	97.3	2.2	77.8	1.7
Sn-113EC	115.09	255.2	246.8	4.3	5.2	0.094
Cr-51	27.703	320.1	1572	27	155.4	2.7
Sn-113IT	115.09	391.7	246.8	4.3	160.3	2.9
Sr-85	64.85	514.0	303.9	5.2	299.3	5.6
Cs-137	10976	661.7	416	7.1	353.5	6.3
Mn-54	312.13	834.8	383.3	4.8	383.2	4.8
Y-88	106.626	898.0	368	4.6	345.5	4.6
Zn-65	244.01	1115.5	798	14	400.7	7.1
Co-60	1925.2	1173.2	444.8	7.7	444.1	7.7
Co-60	1925.2	1332.5	444.8	7.7	444.7	7.7
Y-88	106.626	1836.1	368	4.6	365.5	4.6

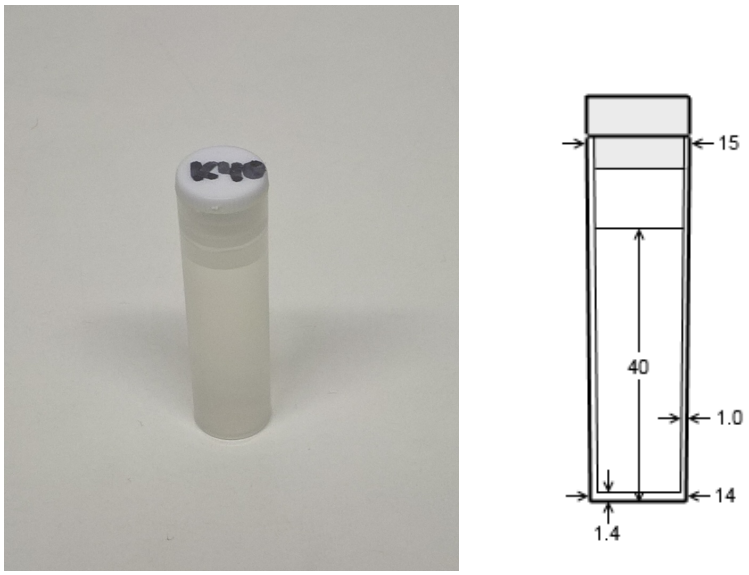

Figure 5.5. The NPL K40 sample and the sample geometry dimensions. All the values are in millimeters. The container is made from polystyrene.

Table 5.4. Nuclides and their half lives, gamma energies, activities and gamma emission rates for the NPL K40 sample. The uncertainty coverage factor is two ($k = 2$).

Nuclide	half life (d)	E (keV)	A (Bq)	δA (Bq)	γ/s	$\delta(\gamma/s)$
Pb-210	8120	46.5	127.60	3.00	5.40	0.10
Am-241	158000	59.5	46.41	0.74	16.67	0.31
Cd-109	461.4	88.0	194.33	7.72	7.11	0.33
Co-57	271.8	122.1	5.99	0.10	5.12	0.09
Co-57	271.8	136.4	5.99	0.10	0.64	0.011
Ce-139	137.641	165.9	4.60	0.10	3.68	0.08
Sn-113EC	115.09	255.2	9.63	0.17	0.20	0.0037
Cr-51	27.703	320.1	1.54	0.03	0.15	0.00
Sn-113IT	115.09	391.7	9.63	0.17	6.26	0.11
Sr-85	64.85	514.0	4.80	0.08	4.72	0.09
Cs-137	10976	661.7	51.58	0.88	43.84	0.78
Mn-54	312.13	834.8	31.28	0.39	31.27	0.39
Y-88	106.626	898.0	13.09	0.16	12.26	0.17
Zn-65	244.01	1115.5	57.74	0.98	28.99	0.51
Co-60	1925.2	1173.2	52.07	0.90	51.99	0.90
Co-60	1925.2	1332.5	52.07	0.90	52.06	0.90
Y-88	106.626	1836.1	13.09	0.16	13.00	0.16

arising from preparing the sample were assumed to be negligible.

5.3.3 One-Nuclide Samples

Samples containing only one radionuclide were manufactured for the total efficiency calibration. The samples were made with solutions of ^{210}Pb, ^{241}Am, ^{137}Cs and ^{60}Co. To make the W0 and T0 samples, discs of filter paper were cut from Shleicher & Schuell Micro Science 589/2 filter paper. The diameters of the discs were the inner diameters of the W and T containers (Figure 5.2). The filter paper was 0.2 mm thick. The samples will be referred to as W0 and T0 one-nuclide samples.

Drops of the solutions were dropped on the filters with a pipette. The distribution of the activity should be as homogenous as possible. Therefore the locations of the drops were determined beforehand. The models for the distribution are in Figure 5.6. If the drops do not overlap, the optimal distance between two rows should be $r \cdot \sin(\pi/3)$, where r is the diameter of one drop. For a 5 µl drop the radius was 11 mm and the distance between rows 9.53 mm. However, to fit more drops to the filter the distance was reduced to 9.0 mm, which means that the drops overlap slightly.

A drop of solution was soaked one or two times on every point, depending on the

gamma emission rate of the solution. The filters were already inside the containers to avoid contamination. If the distribution seemed uneven, drops were put on the filter by hand on dry spots. The filters were dried in a fume hood before closing the containers. Paper filling was put inside the containers after drying to keep the filters tightly pressed to the bottom. Imaging plate pictures were taken of the one-nuclide samples to verify their homogeneity (Figure 5.7).

The K40 samples were done by pipetting the solution to the test tube and filling the tube to the 40 mm height with distilled water. Activity concentration in the tube was assumed to be homogenous. The uncertainty of the filling height was 1 mm.

When the samples were manufactured, it was assumed that the ^{60}Co samples could be used in the total efficiency calibration. Later this assumption was shown to be wrong because the method for calculating the ^{60}Co total efficiency described in chapter 3.3 did not work for the manufactured sources.

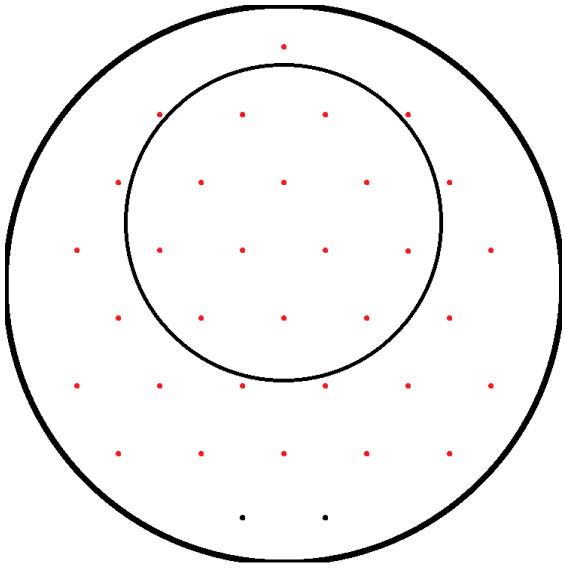

Figure 5.6. Distribution of drops in the one-nuclide Williams and T samples. The inner circle is the distribution for the Williams sample.

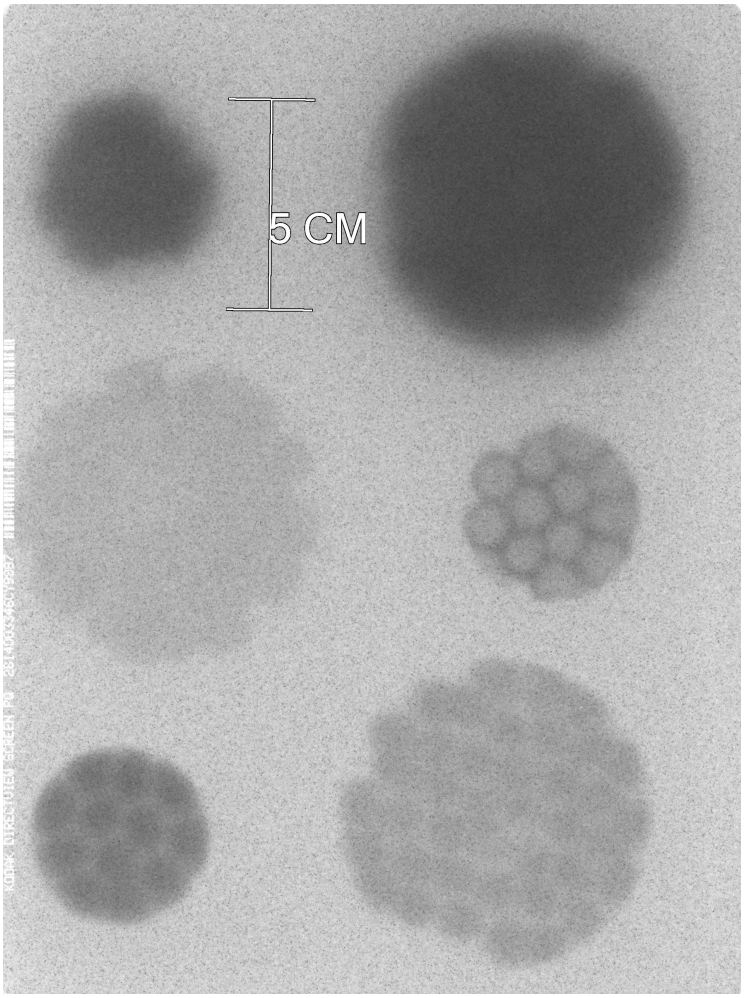

Figure 5.7. An image taken with an image plate of the ^{60}Co (top), ^{137}Cs (middle) and ^{210}Pb (bottom) W0 and T0 one-nuclide samples. The line between the upper samples was 5 cm long. The darker the area, the more energy was absorbed.

6 Experimental Methods and Measurements

This chapter describes setting up the detector and the measurements and the results for the time constant and the background measurements. These results are prerequisites for later measurements and are therefore presented in this chapter. Results of the peak and total efficiency measurements are considered in chapter 7.

6.1 Setting Up The Detector

The Cryo Cycle was filled with liquid nitrogen and the detector dipstick installed. Installing the room temperature warm dipstick vaporized part of the nitrogen and therefore the dewar was filled again after the installation. The detector was cooled for a day before raising the voltage to ensure that the crystal was cold enough.

The preamplifier was attached to the DSPEC50 MCA with two coaxial cables, one cable with a DE-9 connector and one with a safe high voltage (SHV) cable. One of the coaxial cables was used as output for the signal and the other for bias shutdown monitoring. The DE-9 connector was used to give the voltage to the preamp. The preamp has also a test output and a timing output but these were not used. The MCA was connected to a USB port of a PC.

The bias voltage was set to the recommended value of -4000 V. If considerable noise or leakage current is present, the voltage can be raised as long as it is below the depletion voltage -3500 V.

The energy calibration was performed by placing a ^{60}Co source on top of the detector and adjusting the amplification so that the 1332.5 keV peak was at channel 4000. When the peak was adjusted within a few keV, the pole zero adjustment was made. When the energy calibration was complete, the resolution was checked. If the FWHM of the 1332.5 keV peak would have been considerably larger than 1.75 keV, the FWHM given in the detector specification sheet, the detector should have been warmed to room temperature and cooled again. If this had not improved the resolution, the detector should have been sent for repairs. The energy calibration and resolution at other energies was checked with the NPL W0 sample.

6.2 Comparison of Amplifier Time Constants

The effect of rise time and flat top on peak resolution was compared by measuring ^{133}Ba and ^{60}Co point sources on top of the detector. The cobalt source was placed on a Williams container to reduce dead time. Values of flat top of 1.2, 1.6, 2.0 and 2.4 µs were measured with rise times of 6, 9, 12 and 16 µs. The energy calibration and pole zero adjustment were made every time the time constants were changed.

The FWHM and FWTM were compared for the 81.0 keV and 302.9 keV peaks of ^{133}Ba and the 1332.5 keV peak of ^{60}Co. These peaks were chosen to observe the resolution behavior in a wide energy range. The FWHM values were given by Maestro. The FWTM values were not given, so the values had to be approximated by manual calculation. The height of the peak was determined from the channel that contained the maximum number of counts. A straight line was fitted between channels where the count was below and above the tenth of the maximum count. The value where the peak crosses the tenth maximum can be approximated from the straight line by

$$E_{\mathrm{FWTM},i} \approx \frac{\frac{h}{10} - c_1}{\frac{c_2 - c_1}{E_2 - E_1}} + E_1, \tag{6.1}$$

where i refers either to lower or upper side of the peak top, h is the maximum count. On the left side E_1 and E_2 are the energies of the channels where the count is below and above the tenth maximum. On the right side the definitions go vice versa. c_1 is the count in the channel corresponding to energy E_1 and c_2 to energy E_2. (Notice that this equation is a modification of the equation $y - y_0 = k(x - x_0)$.) The same approximation is done on both sides of the peak maximum and the FWTM value is given by

$$\mathrm{FWTM} = E_{\mathrm{FWTM,\ upper}} - E_{\mathrm{FWTM,\ lower}}. \tag{6.2}$$

The measurement times were long enough to ensure an area of at least 40000 for each peak.

The results of the measurements are plotted in Figures 6.1a–f. The FWTM values for the 81.0 keV peak are not completely reliable because the peak began to merge with the 79.6 keV peak of ^{133}Ba. This can be seen as a sharp increase in the FWTM between the rise times of 9 and 12 µs.

For the 81.0 keV and 302.9 keV peaks flat top does not affect the resolution as much as the rise time. For the 1332.5 keV peak flat top is the more important factor and especially with the flat top of 1.2 µs the peak widths are considerably larger. This is a sign of ballistic deficit. This was expected due to large crystal size.

Another important factor in choosing the time constants when analyzing spectra with USS is how well the peak fitting works. If the peak shape differs from equations (3.10) and (4.4), the fit is more difficult to make and the peak area is not equal to the sum of counts in each channel. With the flat top value of 1.2 µs, the 1332.5 keV peak had a large tail on the left side that could not be fitted with USS. The tail is

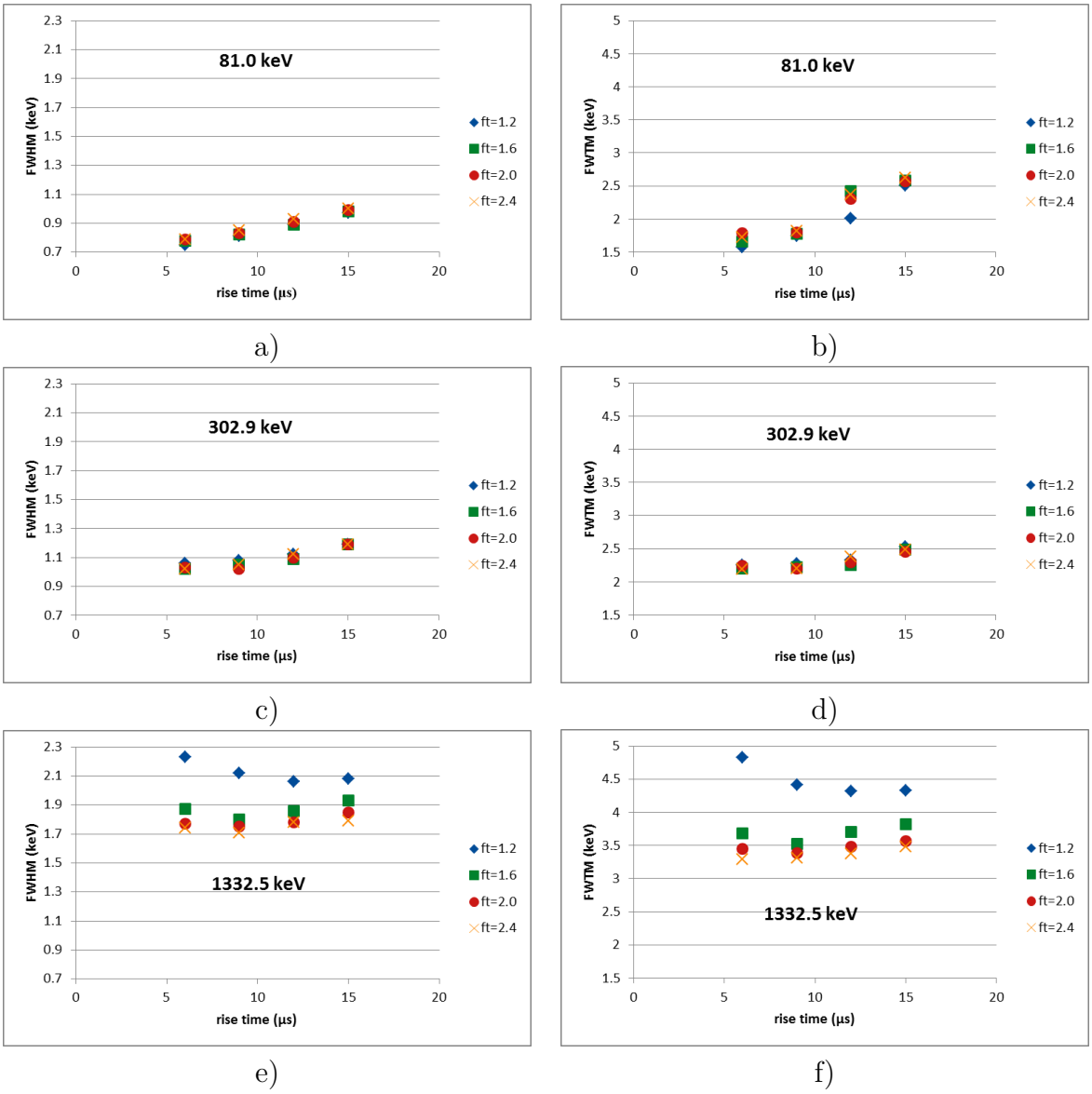

Figure 6.1. FWHM and FWTM values of the 81.0 keV, 302.9 keV and 1332.5 keV peaks as a function of rise time with different values of flat top (ft).

present in every spectra but it is considerably smaller with the larger values of the flat top. The other two peaks were equally easy to fit with all the time constants. Therefore more attention should be paid on the characteristics of the 1332.5 keV peak.

The dead time behavior of the measurements can be seen in Figure 6.2. This Figure contains only values that could be compared with each other. The sources were moved or the measurement geometry altered between other measurements.

After considering the dead time, quality of the peak fit and resolution, time constants

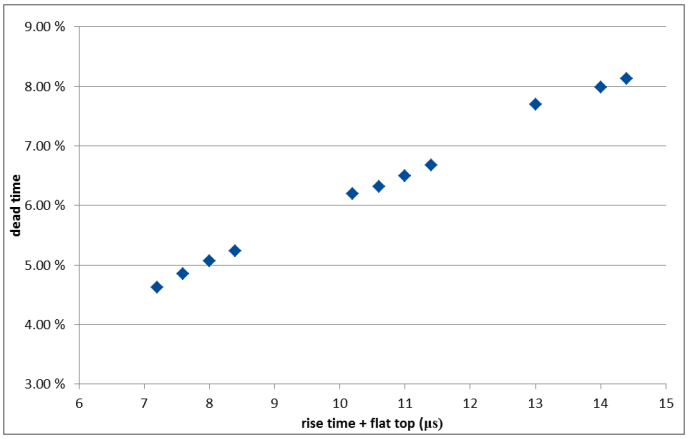

Figure 6.2. Dead time behavior with different time constants. The measurements were done in an identical geometry and the sources were not moved between measurements.

of 9 µs for the rise time and 2.4 µs for the flat top were chosen. This decision was based on the judgment of the author and was validated by an experienced analyst. Although a rise time of 6 µs would lead to lower dead times without considerably increasing peak widths, the peak shape was inferior compared to the 9 µs case.

6.3 Background Measurement

The background was measured for 164 hours and 24 minutes from 6.2.2017 to 13.2.2017. The contamination covers were removed and the lid of the shield was closed. The measured spectrum can be seen in Figure 6.3.

In the background spectrum, the count rate was high below channel 50. This effect is due to noise and does not correspond to any interactions of radiation in the detector. The lower limit of the spectrum was therefore moved to channel 50, or to 16.5 keV. This does not affect the FEP area calculations since the low level for spectrometry is limited to 20 keV.

The measured background spectrum was analyzed using methods discussed in chapter 4.3.1. Some peaks whose area was near the detection limit were discarded. The peaks, their count rates and candidate nuclides of origin are presented in Table 6.1.

Most of the identified nuclides belong to the natural decay series of ^{235}U, ^{238}U and ^{232}Th. Only ^{40}K and the excited states of germanium originate from other sources. The background is consistent with the results of background measurements made with other HPGe detectors at STUK.

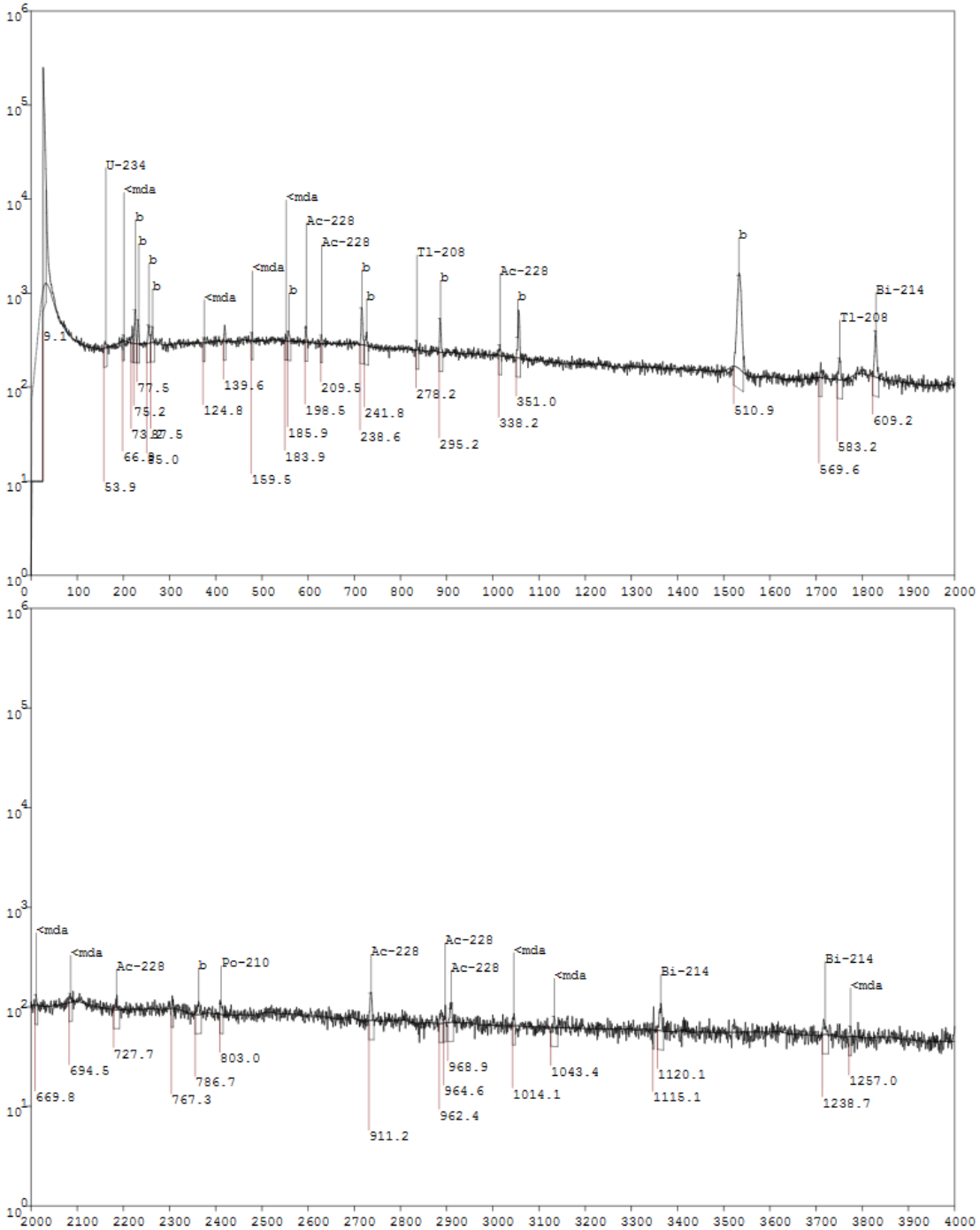
U-234
<mda
b
Ac-228
Tl-208
Bi-214
9.1
53.9
159.5
183.9
185.9
198.5
209.5
238.6
241.8
278.2
295.2
338.2
351.0
510.9
569.6
583.2
609.2
669.8
694.5
727.7
767.3
786.7
803.0
911.2
962.4
964.6
968.9
1014.1
1043.4
1115.1
1120.1
1238.7
1257.0
Po-210

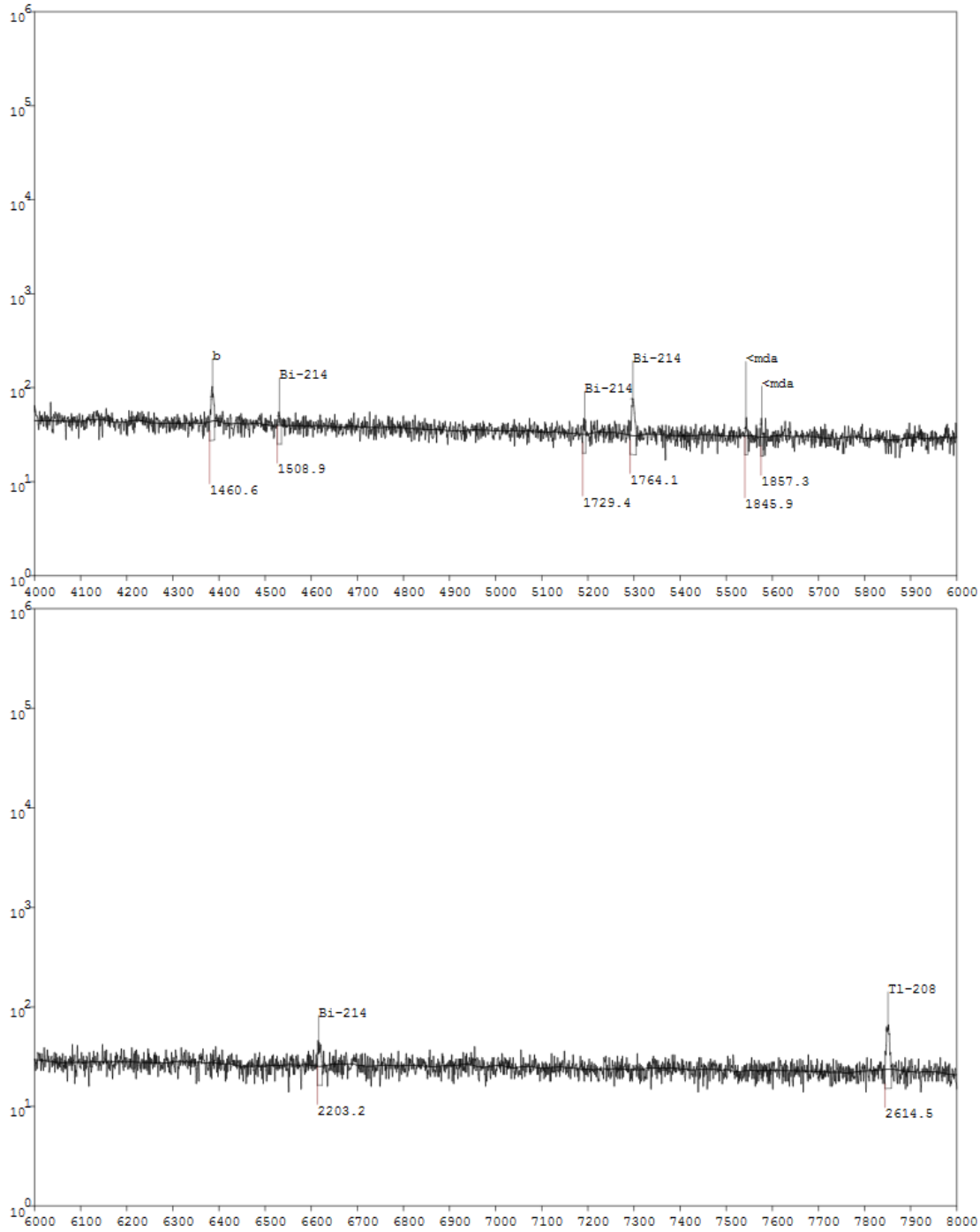

Figure 6.3. The background spectrum with nuclide recognitions made by Gamma-99. The horizontal axis is the channel number. Label b indicates that the peak was not recognized and <mda that the peak area is below a defined detection limit. The energies of the peaks are below the baseline in keV. Some of the peaks were discarded in the analysis made with USS. The spectrum was measured for 164 hours and 24 minutes.

Table 6.1. Peaks identified from the background spectrum. Nuclides identified by Shaman are shown in the fifth column.

E (keV)	δE (keV)	n (cps)	$\delta n/n$ (%)	Nuclides
73.14	0.47	0.0008	4.74	81Tl208
75.2	0.47	0.0021	2.84	81Tl208 82Pb212 82Pb214
77.43	0.47	0.0011	3.92	82Pb212 82Pb214 83Bi214
85	0.48	0.0011	7.72	90Th228 90Th231
87.49	0.48	0.0007	11.82	82Pb212 82Pb214
139.78	0.53	0.0008	11.15	32Ge75M
159.5	0.54	0.0003	31.86	32Ge77M
185.99	0.56	0.0005	16.42	88Ra226 92U235
198.37	0.57	0.0009	10.28	32Ge71M
209.54	0.58	0.0003	32.48	89Ac228
238.68	0.59	0.0026	4.02	82Pb212
241.91	0.6	0.0006	13.18	82Pb214
278.19	0.62	0.0004	19.01	81Tl208
295.27	0.63	0.0018	5.28	82Pb214
338.12	0.65	0.0004	20.07	89Ac228
351.9	0.66	0.0029	3.55	82Pb214
510.95	0.73	0.017	1.07	81Tl208
583.28	0.76	0.0007	9.73	81Tl208
609.22	0.77	0.0021	4.13	83Bi214
911.27	0.86	0.0006	8.85	89Ac228
1120.17	0.9	0.0005	11.00	83Bi214
1460.63	0.94	0.0006	8.18	19K40
1764.49	0.95	0.0005	8.30	83Bi214
2614.62	0.82	0.0005	7.28	81Tl208

6.4 Measurement of The Calibration Samples

The one-nuclide samples were measured to obtain the total efficiency curve. The measurement time was selected so that the full energy peak area was at least 10000 counts to assure a low uncertainty of counting statistics. Some of the measurements were much longer for practical reasons. The W0 and T0 samples were carefully placed on the detector symmetry axis. However, human eye can not see the position of the containers with unlimited accuracy and the uncertainty of the distance of the container center from the symmetry axis was approximated to be 2 mm.

The NPL W0 and T0 samples were measured long enough to detect the 320.1 keV peak of ^{51}Cr. This assured a sufficient counting statistic for other peaks since the half life of ^{51}Cr is 27.7 days and the measurements were done in February 2017. The measurement geometry was the same as for the one-nuclide samples. The measurement starting times and measurement live times are shown in Table 6.2.

The dead time for every measurement was less than 3%, keeping the the effects pulse pile up insignificant.

Table 6.2. Starting times and live times of the measurements.

Sample		Measurement started	Live time (s)
Pb-210	K40	1.2.2017 8:30	26701
	W0	2.2.2017 16:03	61319
	T0	21.2.2017 11:31	73054
Am-241	K40	17.3.2017 16:03	75833
	W0	22.2.2017 9:40	8869
	T0	22.2.2017 12:26	69589
Cs-137	K40	1.2.2017 16:03	57081
	W0	3.2.2017 9:17	12618
	T0	22.2.2017 8:10	4056
NPL	K40	20.2.2017 9:16	92832
	W0	15.2.2017 9:47	88144
	T0	16.2.2017 10:54	89758

7 Analysis of Data and Results

This chapter contains the simulation of the total efficiency curve, the TCS correction factor calculation, FEPE calculation and uncertainty estimations for the results. The calculations, apart from those done in dedicated software, were mostly done by using spreadsheet tools in Microsoft Excel. This chapter also includes the constructing of the model in the MCNP, fitting of the model parameters to experimental results and comparison of the MCNP with GESPECOR.

7.1 Results of The NPL Sample Measurements

The spectra obtained from the NPL sample measurements were analyzed with USS. Since the fitting parameters had to be adjusted by the user, the fit may vary between spectra and this had to be taken into account in the uncertainty calculations. The uncertainty caused by the fit is represented as δn_{fit}. δn_{fit} was approximated by changing the fitting parameters while the quality of the fit seemed to remain equal. Dead times were less than 3% and therefore they were not accounted for in the uncertainty estimations. The peak count rates, relative uncertainties given by USS and relative uncertainties of the peak fits are in Tables 7.1-7.3.

Preliminary full energy peak efficiencies were calculated with equation (3.29) by only correcting for the decay of the nuclides. The FEPE values are shown in Figures 7.1-7.3. These values were needed when calculating the coincidence correction factors with USS.

7.2 Results of The One-nuclide Sample Measurements

The total count rates for ^{210}Pb, ^{241}Am and ^{137}Cs were obtained by calculating the summed count rate in the channels from 50 to the right edge of the peak with Maestro. In addition for ^{137}Cs, the areas of the x-ray peaks were analyzed with Gamma-99. The x-rays can be considered as two separate photons, one caused by the 31.817 keV and 32.194 keV Kα, and the other by 36.304 keV, 36.378 keV and 37.255 keV Kβ x-rays. The energy of the first peak was considered as 32.06 keV and of the second as 36.51 keV. The energies of the peaks were calculated by weighed average where the intensities were used as weights. The summed intensities of the peaks were 5.80% and 1.30%. The data used in these calculations is from ref. [17].

Table 7.1. Results of the NPL W0 sample measurement analyzed with USS. n is the peak count rate. The $\delta n_{\mathrm{stat}}/n$ is the relative uncertainty of the count rate given by USS.

Nuclide	Energy (keV)	n (cps)	$\delta n_{\mathrm{stat}}/n$ (%)	$\delta n_{\mathrm{fit}}/n$ (%)
Pb-210	46.5	0.5982	0.70	3
Am-241	59.5	13.1847	0.10	3
Cd-109	88.0	7.4374	0.13	1
Co-57	122.1	5.4266	0.15	0.5
Co-57	136.4	0.6625	0.53	0.5
Ce-139	165.9	2.7244	0.22	0.5
Sn-113EC	255.2	0.1197	2.01	0.5
Cr-51	320.1	0.0209	9.92	5
Sn-113IT	391.7	2.7261	0.22	0.5
Sr-85	514.0	1.2879	0.34	0.5
Cs-137	661.7	19.9676	0.08	0.5
Mn-54	834.8	10.5997	0.11	0.5
Y-88	898.0	2.3524	0.24	0.5
Zn-65	1115.5	7.7245	0.12	0.5
Co-60	1173.2	12.1488	0.10	0.5
Co-60	1332.5	11.0563	0.10	0.5
Y-88	1836.1	1.4476	0.29	0.5

The activities of the samples were calculated using the results obtained from the NPL sample measurements. The FEPEs for the one-nuclide samples that are made of nuclides present in NPL samples are known without having to fit the FEPE curve.

Table 7.2. Results of the NPL T0 sample measurement analyzed with USS.

Nuclide	Energy (keV)	n (cps)	$\delta n_{\mathrm{stat}}/n$ (%)	$\delta n_{\mathrm{fit}}/n$ (%)
Pb-210	46.5	0.7751	0.58	3
Am-241	59.5	14.8032	0.09	3
Cd-109	88.0	8.5874	0.12	1
Co-57	122.1	6.2699	0.14	0.5
Co-57	136.4	0.7688	0.50	0.5
Ce-139	165.9	3.2446	0.20	0.5
Sn-113EC	255.2	0.1316	2.07	0.5
Cr-51	320.1	0.0282	8.6	5
Sn-113IT	391.7	3.2251	0.21	0.5
Sr-85	514.0	1.545	0.27	0.5
Cs-137	661.7	24.0612	0.07	0.5
Mn-54	834.8	12.7954	0.10	0.5
Y-88	898.0	2.9444	0.22	0.5
Zn-65	1115.5	9.3756	0.11	0.5
Co-60	1173.2	15.4549	0.09	0.5
Co-60	1332.5	14.1531	0.09	0.5
Y-88	1836.1	1.8702	0.25	0.5

Table 7.3. Results of the NPL K40 sample measurement analyzed with USS.

Nuclide	Energy (keV)	n (cps)	$\delta n_{\text{stat}}/n$ (%)	$\delta n_{\text{fit}}/n$ (%)
Pb-210	46.5	2.025	0.26	3
Am-241	59.5	8.1651	0.12	3
Cd-109	88.0	3.5463	0.18	1
Co-57	122.1	2.3753	0.22	0.5
Co-57	136.4	0.2879	0.75	0.5
Ce-139	165.9	0.7802	0.41	0.5
Sn-113EC	255.2	0.0392	3.5	0.5
Cr-51	320.1	0.008	14.93	5
Sn-113IT	391.7	1.1377	0.33	0.5
Sr-85	514.0	0.5168	0.52	0.5
Cs-137	661.7	8.2855	0.12	0.5
Mn-54	834.8	4.2695	0.16	0.5
Y-88	898.0	0.6672	0.44	0.5
Zn-65	1115.5	3.0254	0.19	0.5
Co-60	1173.2	3.3319	0.18	0.5
Co-60	1332.5	2.9304	0.19	0.5
Y-88	1836.1	0.3542	0.58	0.5

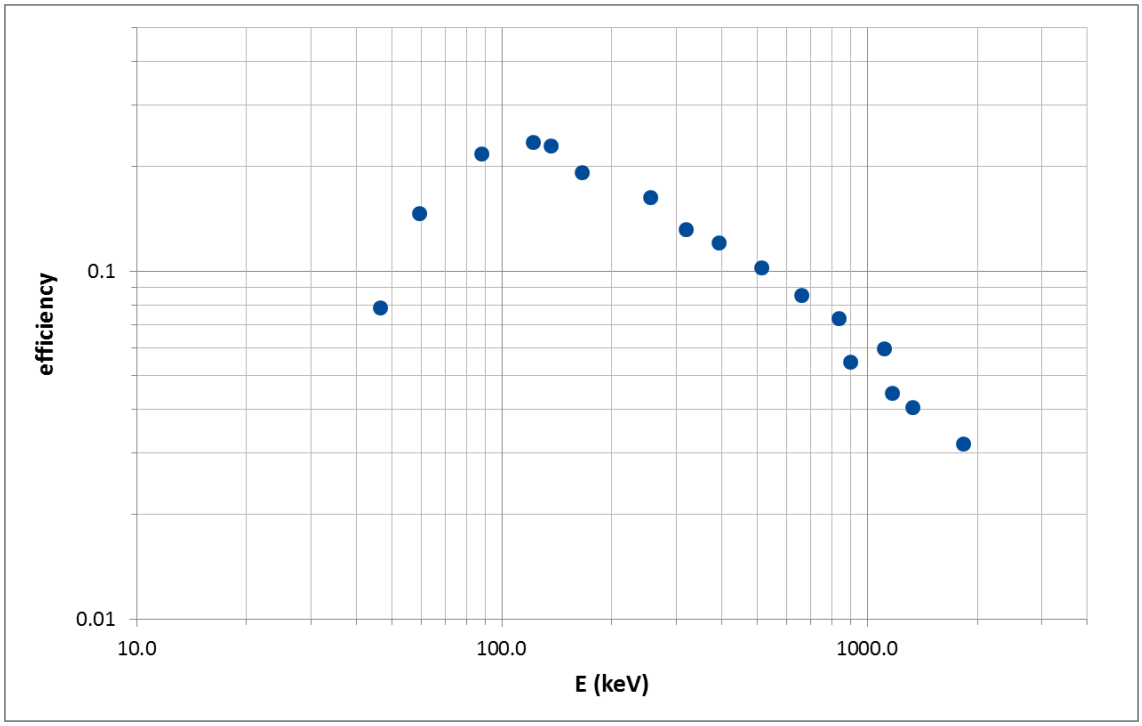

Figure 7.1. The experimental FEPE values without TCS corrections for the NPL W0 sample.

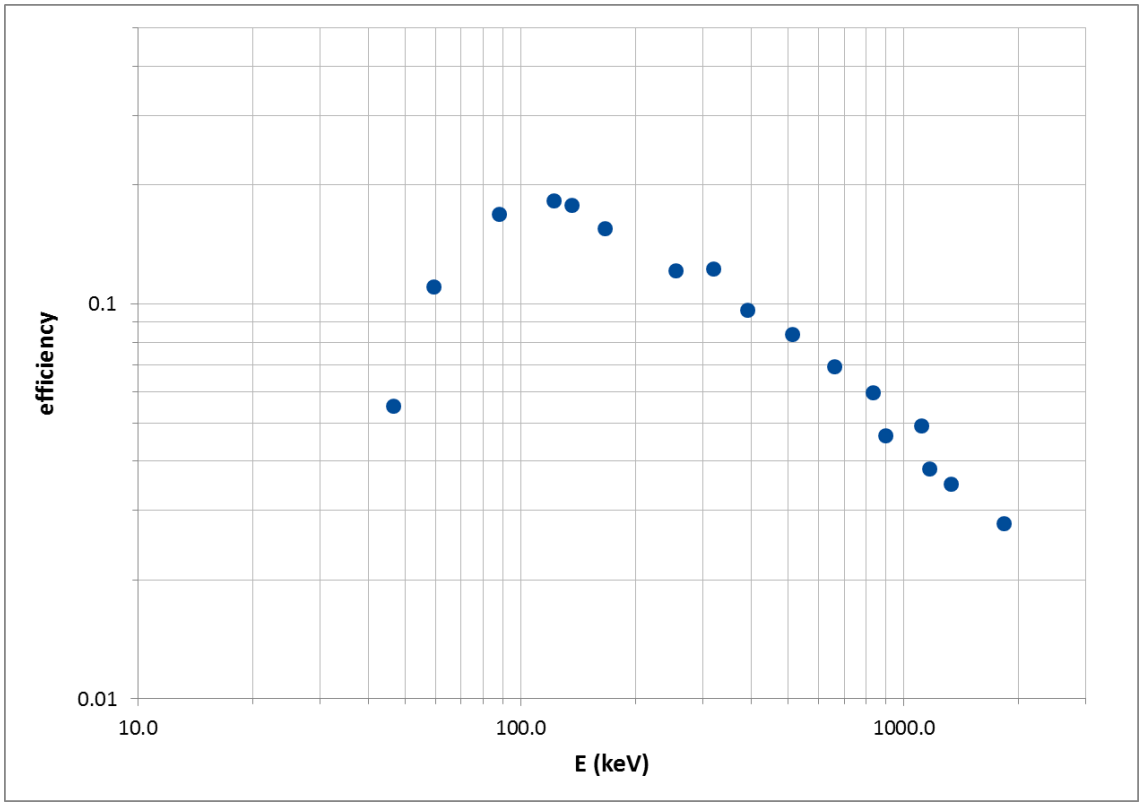

Figure 7.2. The experimental FEPE values without TCS corrections for the NPL T0 sample.

Therefore the activities of the one-nuclide samples can be calculated with

$$A = \frac{n_{\text{peak}}}{n} A_{\text{NPL}}, \tag{7.1}$$

where n_{peak} is the count rate of the full energy peak from the one-nuclide sample measurement, n the count rate of the nuclide in question in the NPL sample measurement and A_{NPL} the activity of the nuclide in the NPL sample with same sample geometry. The count rates of the peaks were calculated with USS.

After calculating the activities, the total efficiency values are obtained with equation (3.31), where

$$n'_{\text{tot}} = n_{\text{tot}} - n_{\text{xray}} - n_{\text{bg}}. \tag{7.2}$$

The summed count rates from the spectra n_{tot}, background count rates n_{bg}, x-ray peak count rates n_{xray} and the peak count rates n_{peak} and their uncertainties are presented in Table 7.4.

The x-rays cause more counts in the spectrum than just the counts in the fill energy peaks. However, the majority of the counts can be assumed to be in the peaks. In addition, the effect on n'_{tot} will be small and the method in equation (7.2) can be used. The uncertainty of the x-ray total count rates was assumed to be 50%. The uncertainties of the peak fits for the FEPs of x-rays were estimated to be 10%.

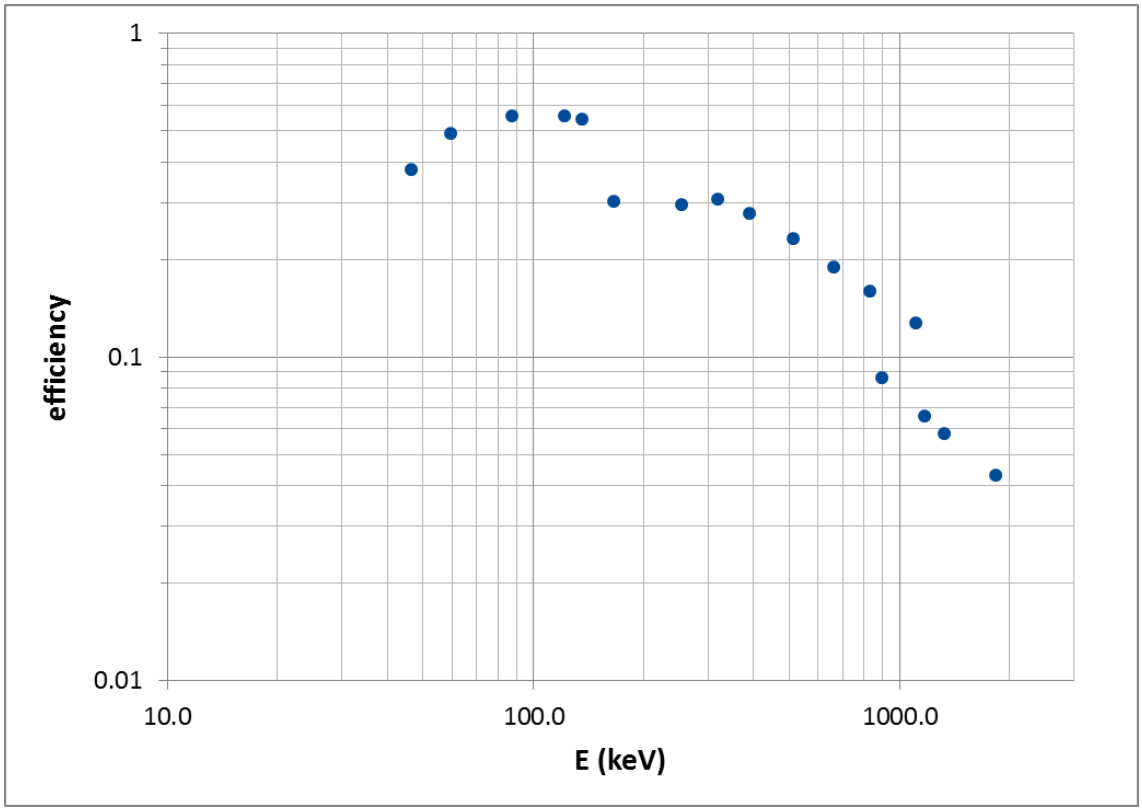

Figure 7.3. The experimental FEPE values without TCS corrections for the NPL K40 sample.

The relative statistical uncertainty of the summed count rates $n_{\mathrm{tot,stat}}$ and the background count rate n_{bg} were $1/\sqrt{N}$, where N is the total count. There was also uncertainty in determining the peak right side limit. Uncertainty caused by this, $\delta n_{\mathrm{tot,fit}}$ was estimated by varying the summing interval upper limit between the minimum and maximum value. As with the count rates of the NPL sample measurements, the peak count rate has an uncertainty given by USS and one associated with the uncertainty of the fit.

7.3 MCNP Model of The Well Detector and Samples

A model of the W1 well detector was made with the MCNP. The purpose of the MC simulations was to acquire the total efficiency curves and approximate uncertainties caused by variations in the sample dimensions. Detector datasheet, specification sheet and an x-ray image of the detector in Figure 7.4 were used to get the detector dimensions. The MCNP model dimensions of the detector, shield and samples are presented in Table 7.5. A cross section of the model with the K40 sample inside the well is shown in Figure 7.5.

Table 7.4. Data from the one-nuclide sample measurements and the uncertainties of the fits.

Nuclide	E (keV)	n_{tot} (cps)	$\delta n_{\mathrm{tot,\ stat}}/n_{\mathrm{tot}}$ (%)	$\delta n_{\mathrm{tot,\ fit}}/n_{\mathrm{tot}}$ (%)	n_{bg} (cps)	$\delta n_{\mathrm{bg}}/n_{\mathrm{bg}}$ (%)	n_{xray} (cps)	$\delta n_{\mathrm{xray}}/n_{\mathrm{xray}}$ (%)	n_{peak} (cps)	$\delta n_{\mathrm{peak,\ USS}}/n_{\mathrm{peak}}$ (%)	$\delta n_{\mathrm{peak,\ fit}}/n_{\mathrm{peak}}$ (%)
W0:											
Pb-210	46.5	0.8856	0.43	2	0.0589	0.54	0		0.3866	0.7	3
Am-241	59.5	8.7677	0.35	2	0.0751	0.47	0		5.0500	0.5	3
Cs-137	661.7	25.6149	0.18	0.03	0.7271	0.15	0.1738	50	8.3438	0.3	1
T0:											
Pb-210	46.5	1.1292	0.35	2	0.0589	0.54	0		0.4763	0.6	3
Am-241	59.5	7.4325	0.14	2	0.0751	0.47	0		4.1761	0.2	3
Cs-137	661.7	33.5191	0.27	0.03	0.7271	0.15	0.125	50	10.643	0.5	1
K40:											
Pb-210	46.5	6.1540	0.25	2.2	0.0589	0.54	0		3.7452	0.32	3
Am-241	59.5	29.733	0.07	1	0.0751	0.47	0		20.5221	0.08	3
Cs-137	661.7	64.049	0.05	0.03	0.7271	0.15	1.906	50	22.7146	0.09	1

Table 7.5. Parameters of the MCNP models. Picture of the model can be seen in Figure 7.5. The dead layer values inside the brackets are for the FEPE model. The parts under the detector crystal were not included in the table because their effect on the simulations was found to be insignificant.

Parameter	cm	Parameter	cm
Detector		**W0**	
crystal radius in middle	4.475	container inner radius	2.1
crystal radius on top	3.556	bottom thickness	0.12
crystal height	6.85	side thickness	0.19
crystal well radius	1.05	sample height	0.04
crystal well depth	3.85	**T0**	
holder thickness	0.15	container inner radius	3.7
holder band thickness	0.175	bottom thickness	0.12
holder band height	1.0	side thickness	0.21
plastic thickness	0.15	sample height	0.04
end cap outside radius	5.4	**K40**	
end cap thickness side	0.1	container outer radius bottom	0.7
end cap thickness top	0.15	container outer radius top	0.75
end cap well radius	0.8	container side thickness	0.1
end cap well depth	4.0	container bottom thickness	0.14
end cap thickness in well side	0.055	container height	5.16
end cap thickness in well bottom	0.1	sample height	3.86
crystal-window distance on top	0.45	container cap height	1.0
dead layer top	0.02 (0.04)	contamination cover thickness	0.03
dead layer side	0.03 (0.3)	contamination cover height	4.0
dead layer well	0.005 (0.016)		
Shield			
shield height	72.5		
shield top height	16		
shield outer radius	26.25		
shield inner radius	10.25		
height of cavity inside the shield	39.5		
end cap shield vertical distance	19.4		

The detector is curved on the top corner. This was modeled by constructing the crystal from two cells, a cylindrical part on bottom and a cut cone on the top. The conical part begins 3 cm from the top of the crystal. From Figure 7.4 it can be seen that there is material on top of the crystal that radiation penetrates relatively well. This material was assumed to be plastic. Every other detector material except the crystal was assumed to be aluminum. The density of the germanium was calculated by assuming that its thermal expansion behaves normally to 77 K. The same assumption was done in ref. [11]. The density of germanium in room temperature is 5.323 g/cm^3 and 5.344 g/cm^3 at 77 K.

The thickness of the dead layer was determined by comparing the results of the

simulations with the experimental values. Two detector models were made: one for the total efficiency and the other for the FEPE simulations. The dead layer values given in the detector datasheet were used as initial guesses.

The slightly conical shape of the K40 sample was taken into account. The contamination cover inside the well was included in the model without tape or the wrap on the bottom. The end cap is slightly curved inwards on top. This was not modeled but was corrected for by raising the T0 sample 0.5 mm from top of the end cap. All the container materials were modeled as polyethylene (C_2H_4) with a density of 0.93 g/cm^3. The filters were modeled as polyethylene with a density of 1.6 g/cm^3. The modeling of the filter material can not cause large errors, especially since the filters do not contain heavy nuclides.

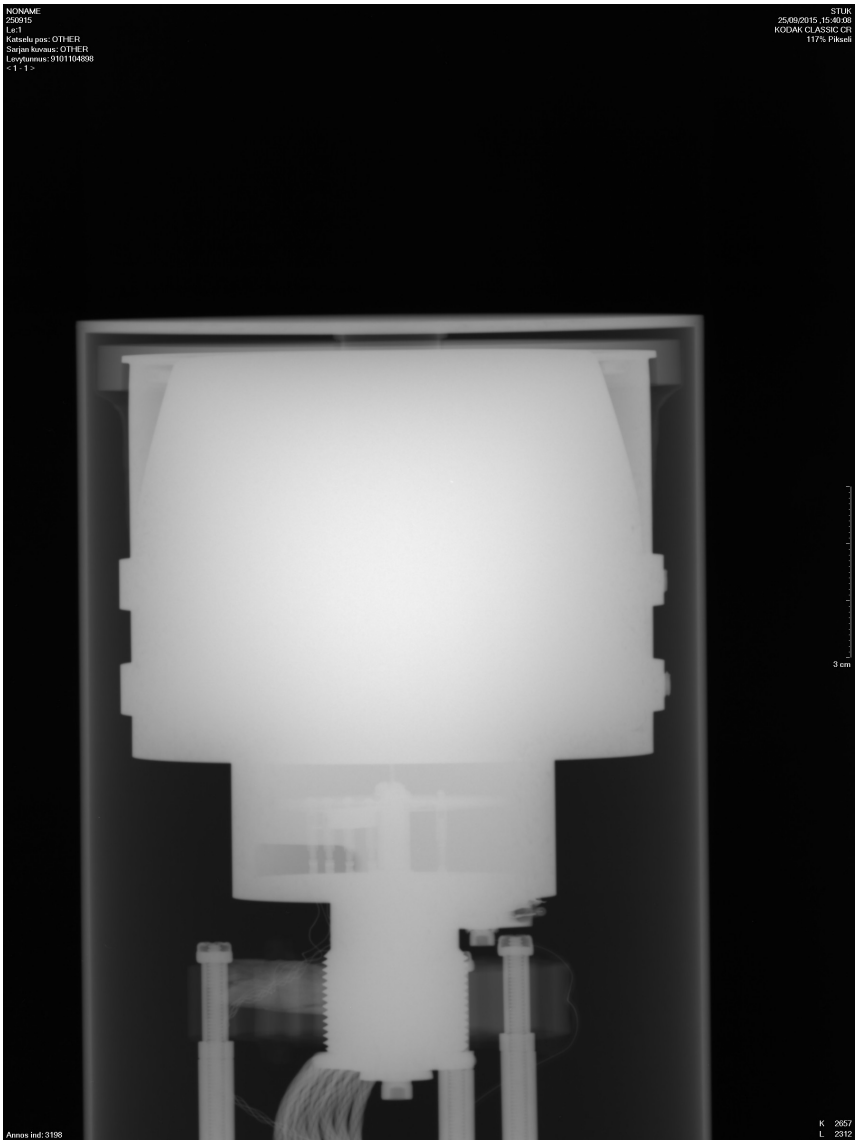

Figure 7.4. X-ray image taken of the W1 well detector.

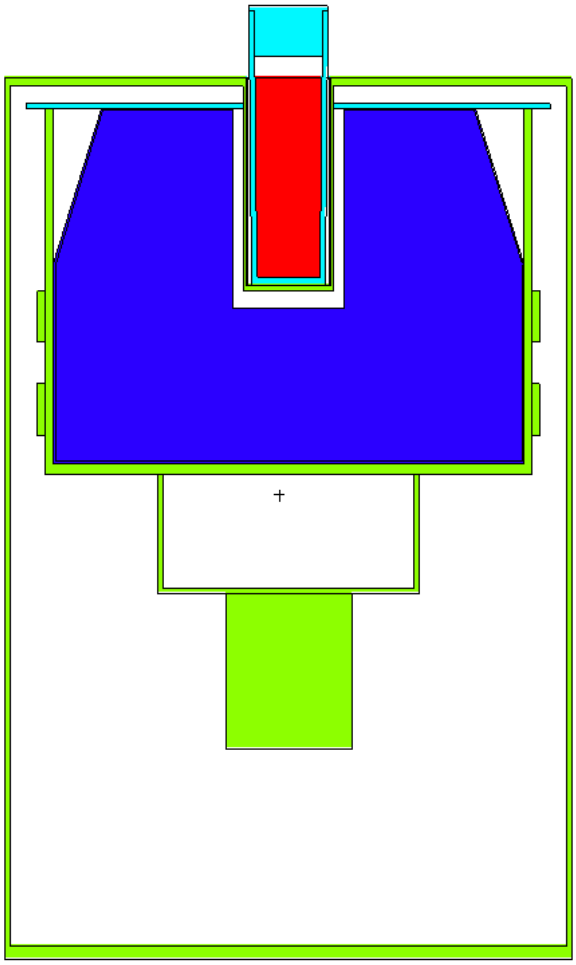

Figure 7.5. Cross section of the MCNP model of the W1 well detector with the K40 sample inside the well. The materials are labeled with different colors.

When simulating FEPEs, the number of runs per energy was one million. This resulted in relative statistical uncertainties less than 0.6% at energies higher than 30 keV. When simulating total efficiencies, the number of runs per energy was one hundred thousand resulting in relative statistical uncertainty less than one percent for energies higher than 40 keV and less than 0.7% for energies higher than 70 keV. The electron transport was off in the simulations.

The uncertainty caused by the inaccuracy of the MCNP total efficiency model can not be taken into account in spectra analyzed with USS. This is because USS does not use the uncertainties of the total efficiency values. The FEPE model is used only to estimate uncertainties caused by variation of the sample dimensions and therefore the uncertainty of the model is of no consequence as long as the simulated values are close to measured ones.

7.4 Uncertainties Related to Samples

7.4.1 Calibration Samples

The homogeneity of the W0 and T0 samples were determined from the imaging plate pictures (Figures 5.4 and 5.7). The image of the one-nuclide samples in Figure 5.7 was printed and the length of the 5 cm line was measured to get the scale of the picture. The images made by the ^{60}Co samples were more blurry. When converted into real dimensions, The diameters of the T0 samples were 7.66 cm for the ^{60}Co sample and 7.42 cm for the ^{210}Pb and ^{137}Cs samples. The diameters of the W0 samples were 4.03 cm and 4.19 cm. If the results of ^{60}Co samples are not taken into account, the diameters of the one-nuclide sample active areas can be assumed to be the same as the container inner diameters.

The spread of the solution on the filters for the one-nuclide samples varied. For cesium, the areas where the drops overlapped had a larger activity concentration than the areas were the drops were put. For Pb the highest activity concentration was in the middle of the drop. The solution did not spread through the whole filter and the samples had a slight triangle like shape. The difference to homogenous circular sample was assumed to result from the activity distribution on the sides. The effect of the sample inhomogeneity on uncertainty was estimated by simulating W0 and T0 samples whose radius was 1 mm smaller than the container inner radius. The collected uncertainties caused by the samples for the Williams and T samples are shown in Tables 7.6–7.7.

The diameters of the W0 and T0 NPL sample active areas were calculated from the image in Figure 5.4 with the same method as the one-nuclide sample diameters. The diameters of the radioactive areas on the filters were 4.19 cm and 7.34 cm, which correspond to the actual filter diameters. The resolution of the image was worse than for the ^{210}Pb and ^{137}Cs one-nuclide samples which resulted to larger uncertainty in determining the diameters of the active areas.

The shape of the active areas of the NPL W0 and T0 were not completely circular. Also, the distribution of drops on the filters did not seem to be planned in any particular way. The drops were probably distributed by hand and may have led to unevenness of the distribution. However, because of the small drop size the distribution could be assumed to be close to homogenous. The uncertainty caused by inhomogeneity and sample radius was estimated by simulating samples with 1 mm smaller radius.

All the container diameters can be assumed to have an uncertainty of 0.2 mm. For the zero thickness samples, this effect was assumed to be negligible on the sides. The uncertainty caused by the container bottom thickness variation was approximated by varying the thickness in the MCNP simulations. The uncertainty caused by the positioning of the sample on the detector was also estimated with the MCNP. The effect of the 2 mm distance from the symmetry axis caused a negligible difference.

For the K40 sample, the filling height uncertainty was estimated to be 1 mm. The effect of this uncertainty on the FEPE values was simulated with the MCNP. The container bottom and side thicknesses were assumed to have an uncertainty of 0.2 mm but the effect on FEPE values was less than 0.2%. The added uncertainty was approximated to be 0.3% at every energy. The uncertainties caused by the K40 samples are in Table 7.8.

7.4.2 Other Samples

Uncertainties related to samples measured with the W1 detector after the calibration must be taken into account in the uncertainties of the FEPE calibration. The K40 samples are designed to be only water samples, or samples that are mostly water with the filling height of 40 mm. Therefore the uncertainties of the K40 calibration sample are the same as for any K40 sample. The following discussion considers only Williams and T samples.

The uncertainty of the filling height was estimated to be 1 mm. The uncertainty caused by this variation was simulated with MCNP by changing the filling height of water samples in case of a full container. The maximum filling height for a Williams container is 25 mm and 26 mm for a T container. Unlike in the case of the calibration samples, the variation of the container side thickness becomes significant for the full containers. This effect too was simulated with the MCNP for containers filled with water. Both cases, the one where the outer and the one where the inner radius remained constant were simulated and the one with the larger difference to the average case was taken as the uncertainty.

The self absorption correction in USS was compared to the MCNP simulations to approximate its uncertainty. The corrections are known not to be valid for thicknesses above approximately 1.5 g/cm^3. Sample material is not given to USS and therefore the sample material should be included in the uncertainty simulations. Self absorption coefficients for a pure carbon sample with a density of 1.5 g/cm^3 were calculated and the relative uncertainty was considered as the difference between the USS and MCNP values. The differences for energies of the ^{137}Cs x-rays could not be compared and were assumed to be 20%.

The uncertainty of the positioning of the sample in a general case is larger than in case of calibration samples. The person responsible for routine measurements can not be assumed to check the positioning as thoroughly as in case of calibration samples. An upper limit of 5 mm was estimated for the distance between the detector and container symmetry axis. The effect of this difference was largest with a full container and this difference was used as the uncertainty. The total relative uncertainty caused by the variation of the sample dimensions δ_{sample} was obtained with the error propagation law.

Table 7.6. Uncertainties of the FEPE values caused by variations of the sample parameters for the Willams containers. All values are in percentage. The total relative sample uncertainty δ_{sample} was calculated with the error propagation law.

E (keV)	inhomogeneity	bottom thickness	filling height	position	side thickness	self absorption	δ_{sample}
30	4.898	0.913	2.041	0.555	0.630	20	20.73
40	1.790	0.917	2.151	1.612	0.168	16.022	16.37
47	1.315	1.044	2.064	1.391	0.138	13.502	13.83
60	0.927	1.050	2.008	1.538	0.207	10.884	11.26
88	0.830	1.160	2.088	1.308	0.141	7.528	8.05
122	0.934	1.273	1.988	1.203	0.221	6.173	6.79
136	0.955	1.243	2.057	1.148	0.225	5.975	6.61
166	1.054	1.244	2.051	1.153	0.165	5.969	6.62
255	1.056	1.083	1.948	1.098	0.145	6.430	6.98
320	1.077	1.148	1.948	1.180	0.094	6.647	7.20
392	0.956	1.145	1.777	1.091	0.136	6.844	7.31
514	1.027	1.147	1.677	1.272	0.104	6.905	7.38
662	0.998	1.052	1.825	0.940	0.080	6.781	7.23
835	0.963	1.203	1.659	1.192	0.083	6.610	7.09
898	1.035	1.105	1.680	1.512	0.005	6.639	7.17
1116	1.195	1.028	1.632	1.755	0.086	6.821	7.40
1174	1.064	0.984	1.591	1.424	0.023	6.750	7.23
1323	1.026	0.956	1.571	1.422	0.040	6.764	7.23
1837	0.667	0.918	1.822	0.772	0.313	6.513	6.91

7.5 Simulation of Total Efficiency Curves

From equations (3.31), (7.1) and (7.2) the total efficiency is

$$\eta = \frac{n_{\text{tot}} - n_{\text{bg}} - n_{\text{xray}}}{I \cdot A} = \frac{(n_{\text{tot}} - n_{\text{bg}} - n_{\text{xray}})n}{I \cdot n_{\text{peak}} \cdot A_{\text{NPL}}}. \tag{7.3}$$

The uncertainty of the total efficiency calculated with the error propagation law is

$$\delta\eta = \left(\left(\frac{\delta n_{\text{tot}}}{I \cdot A} \right)^2 + \left(\frac{\delta n_{\text{bg}}}{I \cdot A} \right)^2 + \left(\frac{\delta n_{\text{xray}}}{I \cdot A} \right)^2 + \left(\frac{(n_{\text{tot}} - n_{\text{bg}} - n_{\text{xray}})\delta A}{I \cdot A^2} \right)^2 \right)^{\frac{1}{2}}, \tag{7.4}$$

where

$$\delta n_{\text{tot}}^2 = \delta n_{\text{tot, stat}}^2 + \delta n_{\text{tot, fit}}^2 + n_{\text{tot}}^2 \delta_{\text{sample, tot}}^2, \tag{7.5}$$

$$\delta A^2 = \left(\frac{\delta n_{\text{peak}} A_{\text{NPL}}}{n} \right)^2 + \left(\frac{n_{\text{peak}} \delta A_{\text{NPL}}}{n} \right)^2 + \left(\frac{n_{\text{peak}} A_{\text{NPL}} \delta n}{n^2} \right)^2, \tag{7.6}$$

$$\delta n_{\text{peak}}^2 = \delta n_{\text{peak, stat}}^2 + \delta n_{\text{peak, fit}}^2 + n_{\text{peak}}^2 \delta_{\text{sample, tot}}^2 \tag{7.7}$$

and

$$\delta n^2 = \delta n_{\text{stat}}^2 + \delta n_{\text{fit}}^2 + n^2 \delta_{\text{sample, tot}}^2. \tag{7.8}$$

For the W0 and T0 samples $\delta_{\text{sample, tot}}$ is the sample uncertainty caused by the components inhomogeneity and bottom thickness from Tables 7.6 and 7.7. This is because these components are the only ones related to the W0 and T0 samples and the uncertainties of other samples do not need to be taken into account in the total efficiency calibration. For the K40 sample $\delta_{\text{sample, tot}}$ and δ_{sample} are equal. The relative sample uncertainty was assumed to be the same for the total count rates and the FEP count rates. The uncertainty of the gamma yield was assumed to be negligible. The total efficiency values and their uncertainties are presented in Table 7.9.

In the MCNP model the dead layer thickness was adjusted so that the simulated total efficiencies were close to the experimental values. The dead layer thickness inside the well and on top of the detector were adjusted by fitting the simulated values to the experimental values at 46.5 keV and 59.5 keV. The dead layer thicknesses on the side and bottom were determined with the 661.7 keV experimental value. When adjusting the model, the lower limit of the energy bin was set to 16.5 keV to have the same lower limit as in the spectra. This cut was made in the measurements because there was considerable noise below this limit and no information about the interactions of the photons was available in channels below 50. The simulated total efficiency values and their comparison to experimental values are shown in Table 7.9.

Table 7.7. Uncertainties of the FEPE values caused by variations of the sample parameters for the T containers. All values are in percentage. The total relative sample uncertainty δ_{sample} was calculated with the error propagation law.

E (keV)	inhomogeneity	bottom thickness	filling height	position	side thickness	self absorption	δ_{sample}
30	5.202	0.740	1.925	1.882	1.540	20	20.91
40	4.276	0.901	1.736	2.487	1.238	16.854	17.72
47	3.936	1.020	2.089	2.255	1.413	12.590	13.66
60	3.516	1.133	1.997	2.327	1.424	9.092	10.38
88	3.160	1.249	2.048	2.163	1.559	5.811	7.52
122	2.771	1.290	1.990	2.270	1.511	5.176	6.89
136	2.652	1.245	1.962	2.022	1.462	5.143	6.72
166	2.447	1.263	2.020	1.886	1.377	5.418	6.82
255	2.104	1.117	1.841	2.004	1.321	6.275	7.36
320	1.960	1.181	1.881	2.039	1.185	6.725	7.72
392	1.965	1.076	1.885	2.060	1.170	6.989	7.94
514	1.986	1.052	1.846	1.840	1.120	7.045	7.92
662	1.755	1.095	1.683	1.506	1.064	7.299	7.99
835	1.625	1.112	1.626	1.387	1.172	7.027	7.69
898	1.586	1.098	1.677	1.603	1.119	7.007	7.71
1116	1.611	1.026	1.622	1.789	1.005	7.036	7.75
1174	1.733	0.984	1.647	1.507	0.999	7.072	7.74
1323	1.687	0.901	1.452	1.009	1.074	7.029	7.57
1837	1.358	0.844	1.681	0.697	0.931	6.982	7.45

Table 7.8. Uncertainties of the FEPE values caused by variations of the sample parameters for the K40 containers. All values are in percentage. The total relative sample uncertainty δ_{sample} was calculated with the error propagation law.

E (keV)	filling height	container dimensions	δ_{sample}
20	2.462	0.300	2.480
30	2.194	0.300	2.215
40	1.976	0.300	1.999
47	1.859	0.300	1.883
60	1.701	0.300	1.727
88	1.545	0.300	1.574
122	1.506	0.300	1.536
136	1.503	0.300	1.533
166	1.485	0.300	1.515
255	1.467	0.300	1.497
320	1.447	0.300	1.478
392	1.452	0.300	1.483
514	1.404	0.300	1.436
662	1.397	0.300	1.429
835	1.396	0.300	1.428
898	1.366	0.300	1.398
1116	1.403	0.300	1.435
1174	1.419	0.300	1.451
1323	1.393	0.300	1.425
1837	1.370	0.300	1.402

Table 7.9. The experimental total efficiencies η_{exp}, the simulated total efficiencies η_{sim} and their difference. The lower energy limit of the bin for the simulations was 16.5 keV corresponding to the lower limit of the spectra.

Sample	E (keV)	η_{exp}	$\delta\eta_{\text{exp}}$	η_{sim}	$\lvert\eta_{\text{exp}} - \eta_{\text{sim}}\rvert$	$\frac{\lvert\eta_{\text{exp}}-\eta_{\text{sim}}\rvert}{\eta_{\text{exp}}}$ (%)
W0	46.5	0.1674	0.00842	0.17039	0.0029	1.79
	59.5	0.2523	0.01128	0.24734	0.005	1.97
	661.7	0.2528	0.00744	0.26064	0.0078	3.10
T0	46.5	0.1239	0.00869	0.13131	0.0074	5.98
	59.5	0.1951	0.01245	0.19549	0.0004	0.20
	661.7	0.2132	0.00674	0.21714	0.004	1.85
K40	46.5	0.6114	0.03225	0.61503	0.0037	0.59
	59.5	0.7084	0.03052	0.70141	0.007	0.99
	661.7	0.5133	0.01675	0.53175	0.0185	3.59

In the simulation of the total efficiency curve, the lower limit of the energy bin was set to 1 keV. The simulation does not have background and therefore information about the photon interactions in the region 1 keV–16.5 keV was available. The total efficiency curves are plotted in Figure 7.6. USS does a linear interpolation on log-log scale to the given total efficiency values.

There is a correlation between the uncertainties related to sample dimensions with the total and the peak count rates. The uncertainties of the total efficiencies were calculated only for the MCNP model fitting and they do not propagate into uncertainties of the results. Therefore the correlations can be neglected.

7.6 The TCS Correction Factor Calculation and Uncertainty Estimation for The FEPE Values

The preliminary FEPE values from Figures 7.1-7.3 and the simulated total efficiency curves from Figure 7.6 were set as the efficiency calibration points in USS. In addition, the FEPs of x-rays from the ^{137}Cs one-nuclide sample measurements were used as FEPE points. The FEPE values were fitted with linear interpolation. Using these efficiency curves, USS calculated the TCS correction factors for the nuclides present in the NPL samples. The TCS correction was then made to the preliminary

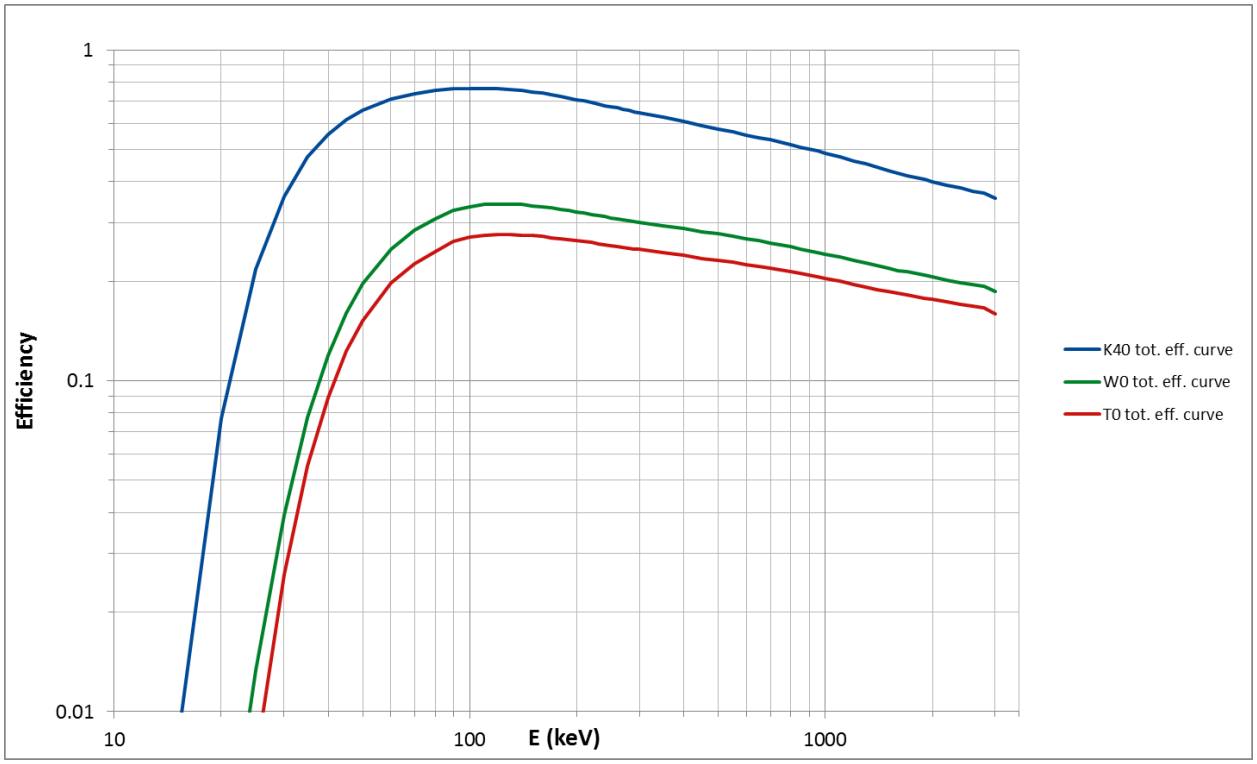

Figure 7.6. Simulated total efficiency curves for the three calibration geometries.

FEPE values. The corrected FEPEs were fed to USS and another coincidence correction factor calculation was performed. The c_{TCS} values were identical to the first calculation.

Equation (4.7) is used for the TCS correction factor uncertainty estimation. The uncertainty caused by self absorption in the sample can be assumed to be negligible because of the thin sample thicknesses of W0 and T0 samples. With the K40 samples the self absorption in the samples is constant since the sample material and filling height is constant in every sample. The effect of the half life uncertainty was neglected. The relative uncertainties of the FEPE values were calculated with the equation

$$\frac{\delta\varepsilon}{\varepsilon} = \sqrt{\left(\frac{\delta n}{n}\right)^2 + \left(\frac{\delta A_{\mathrm{NPL}}}{A_{\mathrm{NPL}}}\right)^2 + \left(\frac{\delta c_{\mathrm{TCS}}}{c_{\mathrm{TCS}}}\right)^2}, \tag{7.9}$$

where

$$\left(\frac{\delta n}{n}\right)^2 = \left(\frac{\delta n_{\mathrm{stat}}}{n}\right)^2 + \left(\frac{\delta n_{\mathrm{fit}}}{n}\right)^2 + \delta^2_{\mathrm{sample}}. \tag{7.10}$$

The TCS correction factors and the final full energy peak efficiency values used as the calibration curve fitting points are presented in Tables 7.10-7.12. A fifth order logarithmic polynomial of equation (3.30) was used as the fitting function in USS. The fit and the discrepancies of the FEPE values are shown in Figures 7.7–7.9.

Table 7.10. The TCS correction factors and full energy peak efficiencies for the W0 NPL sample nuclides.

Nuclide	E (keV)	c_{TCS}	ε	$\delta\varepsilon/\varepsilon(\%)$
Cs-137	32.0	1	0.018	23
Cs-137	36.8	1	0.037	24
Pb-210	46.5	1	0.079	14.3
Am-241	59.5	1	0.147	11.8
Cd-109	88.0	1	0.218	9.0
Co-57	122.1	1	0.234	7.0
Co-57	136.4	0.997	0.229	6.9
Ce-139	165.9	1.06	0.204	7.1
Sn-113EC	255.2	1.009	0.165	7.5
Cr-51	320.1	1	0.132	12.4
Sn-113IT	391.7	1	0.121	7.5
Sr-85	514.0	1	0.103	7.6
Cs-137	661.7	1	0.086	7.5
Mn-54	834.8	1	0.073	7.2
Y-88	898.0	1.266	0.069	7.6
Zn-65	1115.5	1	0.060	7.6
Co-60	1173.2	1.291	0.058	7.8
Co-60	1332.5	1.304	0.053	7.8
Y-88	1836.1	1.298	0.041	7.4

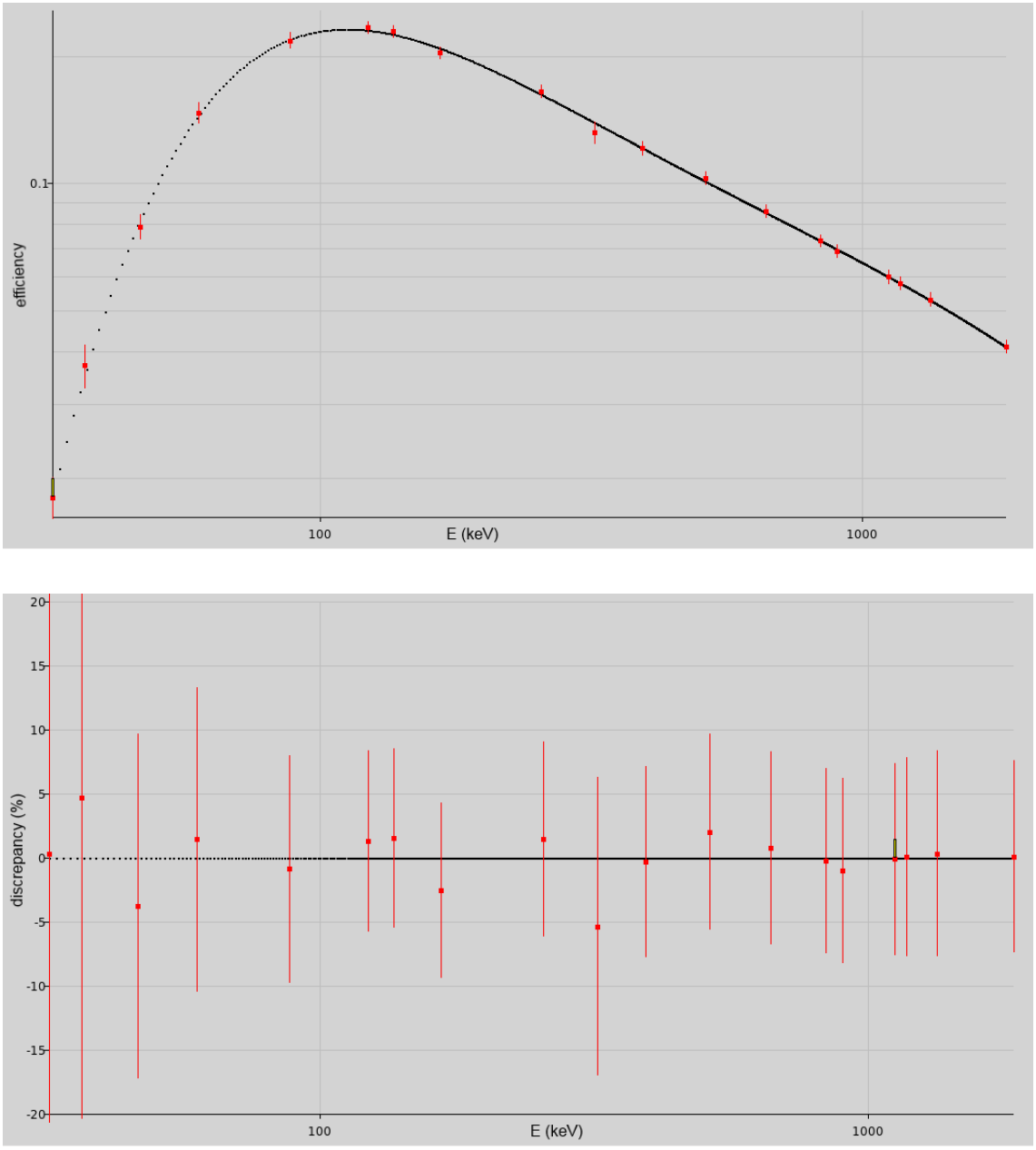

Figure 7.7. The FEPE curve of the W0 sample geometry for detector W1 fitted to the experimental values by USS (top) and the discrepancies of the fit (bottom). The pictures are snapshots from the USS screen.

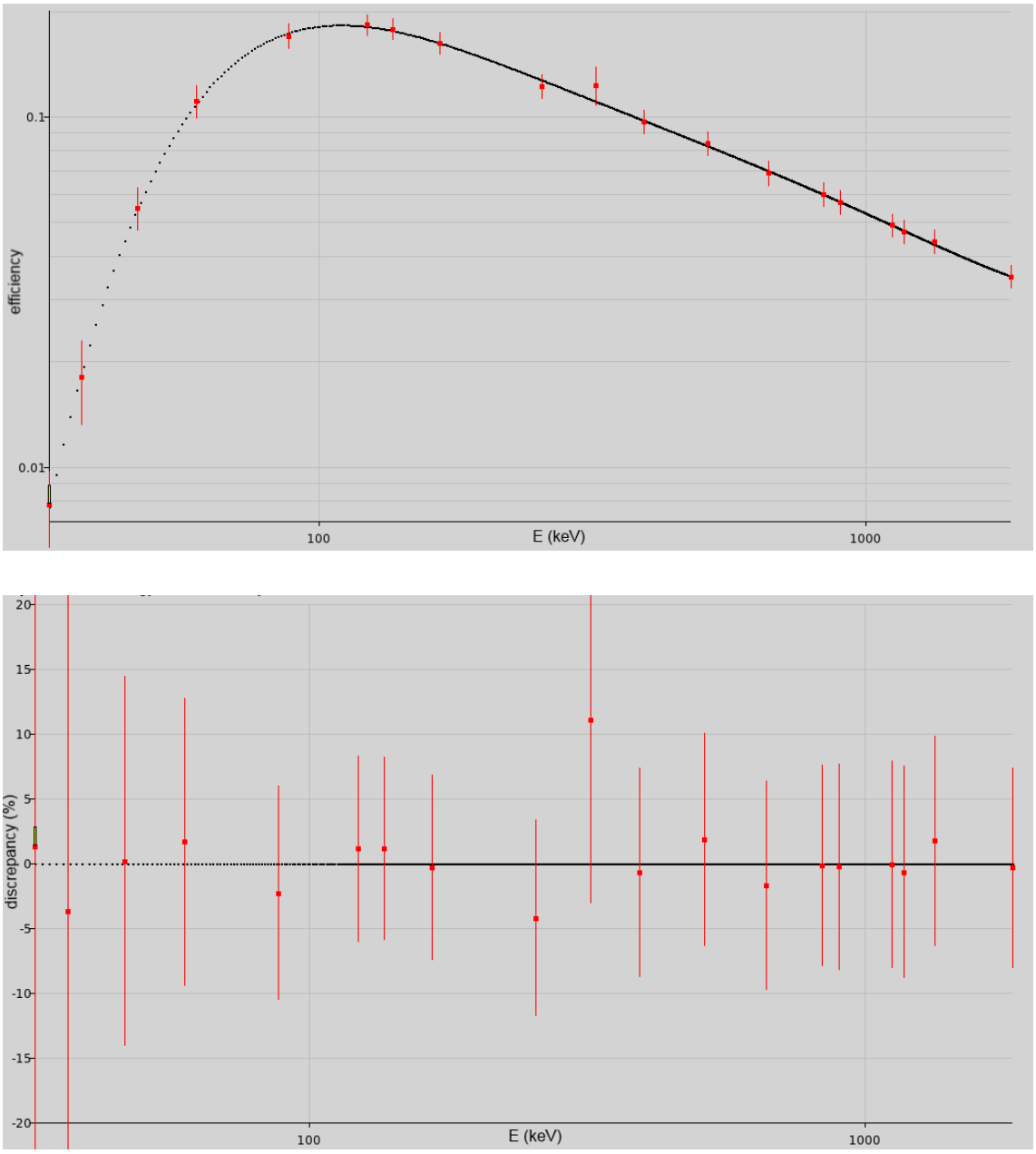

Figure 7.8. The FEPE curve of the T0 sample geometry for detector W1 fitted to the experimental values by USS (top) and the discrepancies of the fit (bottom). The pictures are snapshots from the USS screen.

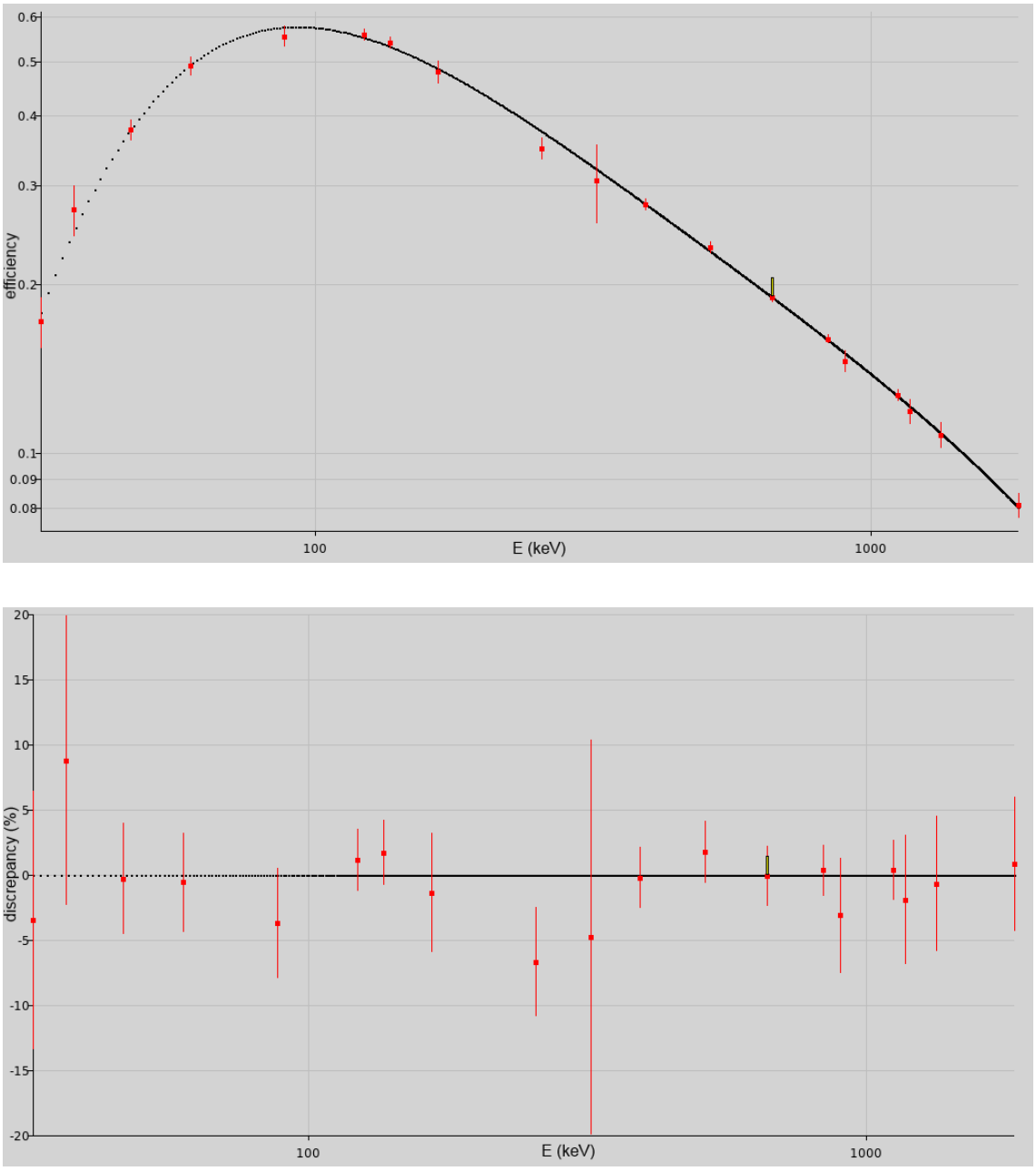

Figure 7.9. The FEPE curve of the K40 sample geometry for detector W1 fitted to the experimental values by USS (top) and the discrepancies of the fit (bottom). The pictures are snapshots from the USS screen.

Table 7.11. The TCS correction factors and full energy peak efficiencies for the T0 NPL sample nuclides.

Nuclide	E (keV)	c_{TCS}	ε	$\delta\varepsilon/\varepsilon(\%)$
Cs-137	32.0	1	0.0078	24.5
Cs-137	36.8	1	0.0181	27.1
Pb-210	46.5	1	0.055	14.1
Am-241	59.5	1	0.111	10.9
Cd-109	88.0	1	0.170	8.5
Co-57	122.1	1	0.183	7.1
Co-57	136.4	0.998	0.178	7.0
Ce-139	165.9	1.042	0.162	7.2
Sn-113EC	255.2	1.005	0.122	7.9
Cr-51	320.1	1	0.123	12.7
Sn-113IT	391.7	1	0.097	8.1
Sr-85	514.0	1	0.084	8.1
Cs-137	661.7	1	0.069	8.2
Mn-54	834.8	1	0.060	7.8
Y-88	898.0	1.218	0.057	8.0
Zn-65	1115.5	1	0.049	8.0
Co-60	1173.2	1.236	0.047	8.2
Co-60	1332.5	1.245	0.044	8.0
Y-88	1836.1	1.241	0.035	7.8

Table 7.12. The TCS correction factors and full energy peak efficiencies for the K40 NPL sample nuclides.

Nuclide	E (keV)	c_{TCS}	ε	$\delta\varepsilon/\varepsilon(\%)$
Cs-137	32.0	1	0.172	10.3
Cs-137	36.8	1	0.272	10.3
Pb-210	46.5	1	0.377	4.3
Am-241	59.5	1	0.490	3.8
Cd-109	88.0	1	0.554	4.4
Co-57	122.1	1.005	0.558	2.4
Co-57	136.4	0.999	0.540	2.5
Ce-139	165.9	1.583	0.479	4.6
Sn-113EC	255.2	1.186	0.350	4.5
Cr-51	320.1	1	0.306	15.9
Sn-113IT	391.7	1	0.278	2.4
Sr-85	514.0	1.005	0.233	2.3
Cs-137	661.7	1	0.190	2.3
Mn-54	834.8	1	0.160	2.0
Y-88	898.0	1.7	0.146	4.6
Zn-65	1115.5	1	0.127	2.3
Co-60	1173.2	1.814	0.119	5.1
Co-60	1332.5	1.871	0.108	5.2
Y-88	1836.1	1.884	0.081	5.1

7.7 Comparison of MCNP and GESPECOR

An identical well detector model was build with MCNP and GESPECOR. The model was as close to the W1 model as possible but was not identical due to disabilities in GESPECOR. GESPECOR can model only cylindrical shapes and therefore the crystal outer surface was cylindrical, not conical on the top part. The radius was the same as for the W1. The holder was not modeled. The dead layer thickness on top and on sides of the detector had to be identical. There was no information about how the dead layer on the detector bottom was modeled. Also, the end cap thickness inside the well, as well as on the top and on the sides was uniform. The dead layer thickness was 0.05 mm inside and 0.03 mm outside the well. The end cap thickness was 1 mm inside the well and 1.5 mm outside the well. Other detector parameters were the same as in Table 7.5.

The container in the model was a test tube with 1 mm side and bottom thickness, 40 mm height measured from outside and 0.65 mm inner radius. The container was inside the well. The sample material was water and the filling height was 39 mm. The sample would have been a K40 sample, but the container thickness had to be uniform on the bottom and on the sides. The FEPE values for the model were simulated with both programs. The simulated FEPE values and their differences are presented in Table 7.13.

7.8 Comparison of W0 and T0 calibrations with a BEGe detector

The FEPEs of the W0 and T0 geometries for the model BE6530P/S BEGe detector B7 and W1 were compared. The FEPE curves of the B7 and the FEPE values of W1 for W0 and T0 geometries are plotted in Figures 7.10–7.11. The FEPE curves of W1 were not plotted because USS does not provide the fitting coefficients.

Most of the Ge detectors at STUK are BEGe detectors similar to the B7 and therefore comparison with the W1 was of interest. The B7 has the largest detector active volume and the largest detection efficiency of the BEGe detectors. The detector dimensions for B7 from the detector specification sheet provided by the manufacturer are shown in table 7.14. The dead layer on the top of the detector is less than 1 µm. The window is thinner than with the W1 and the atomic number of the window material is smaller. Therefore the FEPE at low energies is significantly higher for the B7. The difference between the FEPE curves becomes smaller at higher energies because the attenuation in the window and dead layer become less significant and the mean traveled distance in the crystal more significant. At the energy of approximately 2 MeV, the FEPE of the W1 becomes larger than that of the B7. A comparison between a filter sample measured on top of a BE5030 BEGe detector and inside the well of a SAGe detector is presented in reference [23].

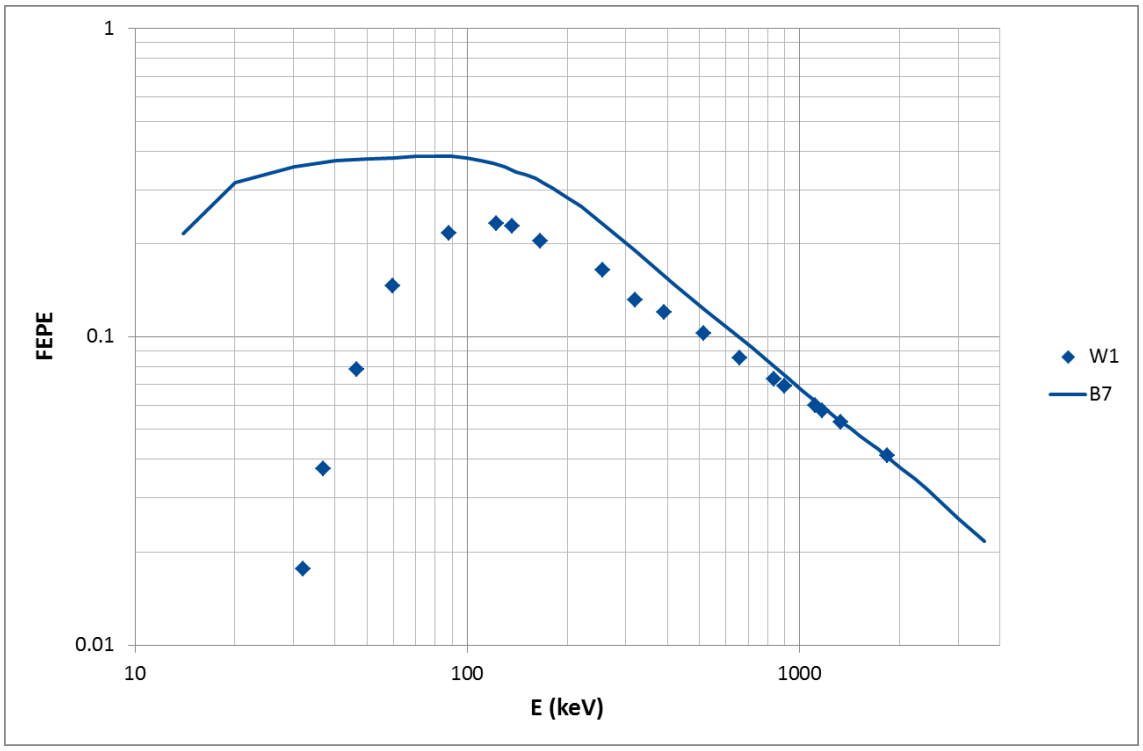

Figure 7.10. FEPE curve of the B7 detector and the FEPE values of W1 for the W0 sample geometry.

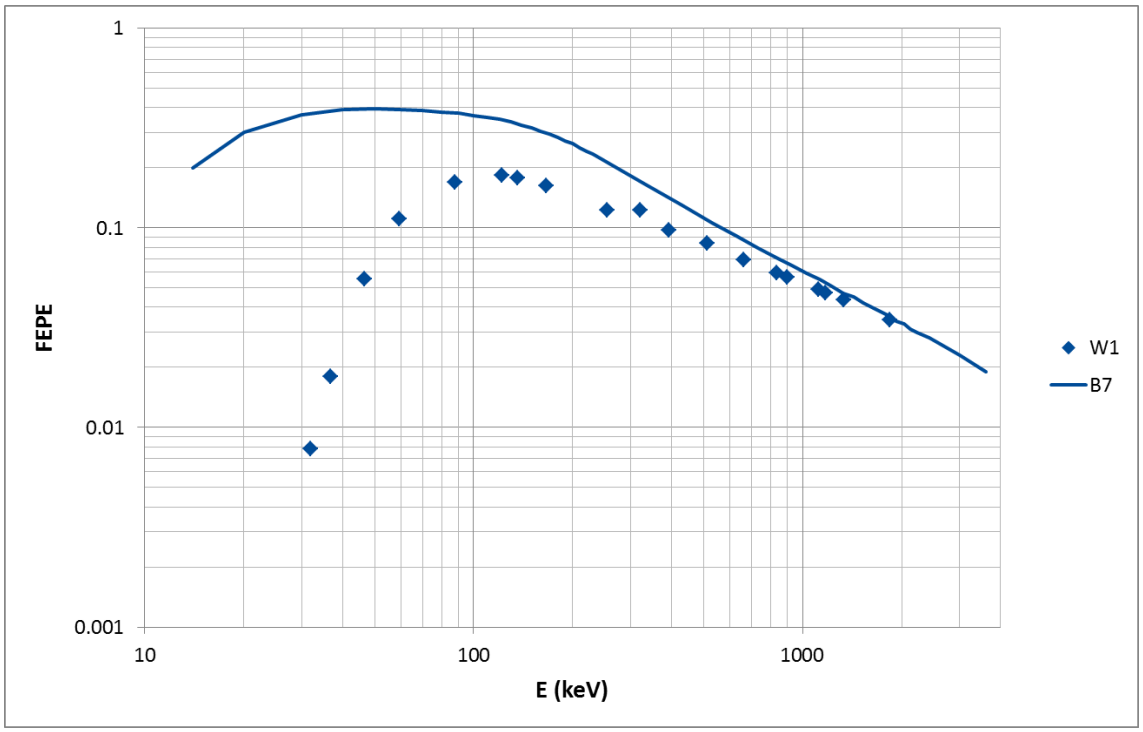

Figure 7.11. FEPE curve of the B7 detector and the FEPE values of W1 for the T0 sample geometry.

Table 7.13. FEPE values of an identical model simulated with MCNP ($\varepsilon_{\mathrm{MCNP}}$) and GESPECOR ($\varepsilon_{\mathrm{GES}}$) and their difference. The MCNP efficiencies were larger.

E (keV)	$\varepsilon_{\mathrm{MCNP}}$	$\delta\varepsilon_{\mathrm{MCNP}}/\varepsilon_{\mathrm{MCNP}}$ (%)	$\varepsilon_{\mathrm{GES}}$	$\delta\varepsilon_{\mathrm{GES}}/\varepsilon_{\mathrm{GES}}$ (%)	difference (%)
30	0.269	0.16	0.262	0.04	2.61
40	0.446	0.11	0.430	0.03	3.61
46.5	0.505	0.10	0.494	0.05	2.22
59.5	0.574	0.09	0.561	0.04	2.31
88	0.620	0.08	0.607	0.05	2.16
122.1	0.621	0.08	0.608	0.02	2.05
136.4	0.613	0.08	0.600	0.04	2.20
165.9	0.584	0.08	0.571	0.06	2.22
255.2	0.466	0.11	0.455	0.08	2.49
320.1	0.399	0.12	0.389	0.05	2.46
391.7	0.344	0.14	0.336	0.08	2.52
514	0.283	0.16	0.276	0.13	2.49
661.7	0.236	0.18	0.230	0.11	2.33
834.8	0.200	0.20	0.195	0.14	2.65
898	0.190	0.21	0.185	0.15	2.71
1115.5	0.163	0.23	0.158	0.16	3.09
1173.2	0.157	0.23	0.153	0.16	2.71
1332.5	0.143	0.24	0.140	0.11	2.74
1836.1	0.111	0.28	0.108	0.09	3.35

Table 7.14. Parameters of the detector B7 from the detector specification sheet.

Diameter	90.5 mm	Window thickness	0.6 mm
Thickness	30.0 mm	Window material	Carbon epoxy
Distance from window	5 mm	Active volume	195 cm^3

8 Discussion and Conclusions

8.1 The Optimization of Time Constants

The selected time constants 9 µs for the rise time and 2.4 µs for the flat top led to peak shapes that could be fitted well with USS. The FWHM of 1.71 keV and the FWTM of 3.31 keV for the 1332.5 keV peak was less than promised by the manufacturer and approximately the same as given in the specification sheet. The FWHM of 0.85 keV for the 81.0 keV point was clearly higher than mentioned in the datasheet and the specification sheet, 0.75 keV and 0.727 keV respectively [21]. This was expected since resolution at low energies was sacrificed for better resolution at higher energies. The resolution at high energies was close to values reported in publications [22, 24, 23]. The peak widths could have been measured with thinner spreads of time constants but after comparing the resolution to the detector specification sheet and to values in literature, it can be concluded that the achieved resolution could not have been far from optimal.

The flat top time constant was larger than with other HPGe detectors at STUK, with which it is in most cases 0.8 µs. This suggests that the ballistic deficit effect is more pronounced with the W1 and the variation of the charge collection time is larger. This is probably due to the size of the crystal and a non homogenous electric field.

8.2 The MCNP Model and The Simulation of The Total Efficiency Curve

The MCNP model was constructed with the best information available, i.e. the data was from the detector specification sheet, datasheet and the x-ray image of the detector in Figure 7.4. The crystal to window distance in the specification sheet was more than 5 mm larger compared to the x-ray image and therefore the specification sheet values were altered when the values did not seem to fit to the model. Also, the rounded edge of the crystal was not mentioned in the specification sheet.

The x-ray image does not give information from inside the well. There could be, for example, rounding up of the corners or the well may not be strictly cylindrical. These possible deficiencies in the model would not cause considerable differences in the geometric efficiency but may change the detection efficiency for high energy photons due to reduced crystal volume.

A layer of constant thickness on the side, top, bottom and inside the well were assumed for the shape of the dead layer in the model. The actual shape can deviate from this considerably especially when measuring FEPEs. Efforts have been made to measure the dead layer thickness and shape for HPGe detectors but the results give no indication on the dead layer shape on the bottom of a well detector [25, 26, 27]. A thicker dead layer may be found in the bottom corner of the detector due to a weak electric field [1].

The effect of electron transport in the MCNP was tested and the differences in the efficiencies were less than 2% for FEPE values and less than 1% for total efficiencies. The differences increased when the energy increased and were less than a couple of tenths of a percent below 500 keV. With higher energy photons, the recoil electrons have higher average energies and therefore are more likely to enter the dead layer or even escape the crystal. Even though the differences were significant for the highest energies, the electron transport was omitted because of the more than tenfold simulations times.

There were other simplifications made in the MCNP model including uniform window thickness, non curved window and non curved outer surface of the upper half of the crystal. The simplifications and deviations from the real geometries may lead to considerable differences in actual and simulated efficiencies at energies far from the experimental values. The uncertainty caused by deviations between the MCNP and the actual geometries can not be estimated without measurements.

The omission of the channels under the energy of 16.5 keV in one-nuclide sample measurements meant that a part of the pulses were not counted. However, the pulses would have drowned to the large background in those channels. The effect was compensated for by comparing the MCNP values to the experiments when the lower limit was also 16.5 keV and simulating the total efficiency with the 1 keV lower limit. This method is not accurate because of uncertainties in the library data and the model at low energies. The differences between Monte Carlo simulation software can be as high as 10% at the energy of 45 keV and approximately 2% at higher energies [28]. The proportion of counts below 16.5 keV is highest for the 46.5 keV gamma-rays of ^{210}Pb. The difference in the total count rate between the MCNP simulations with lower limits of 1 keV and 16.5 keV was less than 6.5%. This demonstrates that only a small percentage of the counts were at the low energies. An estimate of the uncertainty of the low energy cut off method could have been included in the total efficiency uncertainty calculations, but since the uncertainties of the total calibration curves in USS are not used, it would not have provided any additional benefit. For the same reasons the effect of the correlation between the peak area n_{peak} and the total count rate n_{tot} sample uncertainties was left out of equation (7.4).

When fitting the MCNP model to the experimental points, the fact that the efficiency curves should be linear above few hundred keV was used when fitting the model. The limits for TCS correction factors and hence the total efficiencies for ^{60}Co

and ^{88}Y were deduced from this fact: If not within certain limits, the FEPE curve would be far from linear at high energies. To ensure linearity, the total efficiencies were systematically higher than the experimental value of 661.7 keV for ^{137}Cs in Table 7.9. The simulated values were within the uncertainty limits otherwise but with 661.7 keV points of W0 and K40 samples.

8.3 The Full Energy Peak Efficiencies

Since the uncertainties of the sample parameters were calculated by comparing the relative differences between the parameters, an accurate model for the FEPE simulations with the MCNP was not necessary. Still, the simulated efficiencies were within 10% of the experimental values for nuclides with no TCS correction. The reported statistical uncertainties of the FEPE values do not influence the uncertainty calculation. This is because the simulated photons had the same initial parameters in two subsequent simulations and even between all simulations with the same source definition. The behavior of the simulated FEPE values was too even for them to behave in a statistical manner. In other words, the discrepancies of efficiencies between simulations did not oscillate as would have been predicted by the given statistical uncertainties. Therefore the given statistical uncertainty refers to the deviation from the result given by an infinite amount of simulated photons.

The suitability of the method of taking the differences between the MCNP simulations as uncertainties for the FEPE values was not verified with experiments. The assumption that the relative uncertainties could be simulated may not be a good one. However, the method was the best one available and because of the reliability of photon modeling in the MCNP, the uncertainties can be assumed to be close to actual ones.

As can be seen from Tables 7.6 and 7.7, the most significant uncertainty for the Williams and T containers arises from the self absorption correction factor. The function in equation (4.5) has been fitted for one detector over twenty years ago and it is not suitable for well type detectors since the geometries differ significantly [7]. The self absorption effects may not be simulated correctly in the MCNP but the error in the correction made by USS is more likely. In future, better methods for self attenuation correction should be developed. One method could be to calculate the self attenuation factors automatically with numerical methods and correct the efficiency curve before sending the data to USS. With this method, the uncertainties of samples whose geometry is close to calibration geometries would not be overestimated. Another option is to make a new fit of equation (4.5) for the well detector. For now, the error has to be included in the uncertainties of the FEPE calibration values.

The uncertainty caused by the inhomogeneity of the sample given by the NPL for the W0 and T0 samples were 2.5% (k=1). There was no information about how this estimation was done and it was chosen not to be used. From Figure 5.4 it

can be seen that the distribution is not far from homogenous in the center and therefore the simulation of a smaller sample was assumed to be sufficient. The sample distribution could be simulated with the MCNP but constructing the model would demand a considerable amount of labor. The same applies for the one-nuclide samples. In addition, at the moment even the 2.5% uncertainty would be dwarfed by other sources of uncertainty.

The uncertainties of the fits for the NPL samples from Tables 7.1-7.3 were largest for the peaks of ^{210}Pb, ^{241}Am and ^{51}Cr. This is due to the size and shape of the baseline at the foot of the peaks and due to the small peak sizes of ^{51}Cr. As can be seen from Figure 8.1 the shape of the baseline can not be modeled accurately with USS. The baseline is caused by the Compton effects and incomplete charge collection near the surface of the crystal. The difference in the peak shape and fit would not matter if the fit was identical in every analysis. Then the relative difference to better modeled peaks would be equal in all cases and would be compensated for in the calibration curve. However, the fit will always depend on the spectrum to some degree and achieving identical fits is improbable, especially with two different analysts. Therefore the uncertainty of the fit was included in the uncertainty calculation.

The areas of the x-ray peaks were analyzed with Gamma-99 because the peak shapes, shown in Figure 8.2, were far from Gaussian. This was because the peaks consisted of multiple transitions with energies close to each other. The edges of the peaks were unclear and the uncertainty estimate of 10% for the fits was reasonable.

The method for calculating the TCS correction factors by using the uncorrected FEPE values from Tables 7.1-7.3 was justified because the correction factors did not change after using the corrected FEPE values in the second calculation. This also means that the TCS correction factors and their uncertainties do not depend on FEPEs in case of the nuclides in the NPL samples. The uncertainty estimate of equation (4.7) for the TCS correction factors is not based on any physical principles. Still, it gives the scale of the uncertainty and was the best method known. In future, the effect of uncertainty of the total efficiencies on the TCS could be checked by varying the total efficiency values given to USS. This would still leave the question of the effects of the library data correlations unknown.

The TCS corrected FEPE values plotted in Figures 7.7–7.9 form curves with expected shapes. The fitted fifth order logarithmic polynomial is within the uncertainty limits of every other value except the 255.2 keV point of ^{113}Sn for the K40 sample. The fit is not based on any physical principles and therefore does not give information about the quality of the experimental values. A good fit for the W0 and T0 samples was logical because of the large uncertainties. The uncertainty of the curve is propagated via the uncertainties of the experimental values. Using a higher order for the polynomial would not have given an improved fit and the fifth order was deemed optimal.

The 255.2 keV point of ^{113}Sn being clearly below the fitted curve might be a symptom

of underestimated total efficiency for the ^{113}Sn x-rays with energies between 24 keV and 28 keV. If the total efficiency of the x-rays is underestimated, the TCS correction factor for the gamma line will be underestimated too. The difference could also be explained by statistical fluctuations and therefore no attempts were made to modify the MCNP total efficiency model.

The FEPE curve is not linear for the K40 geometry at high energies but bends downwards approximately after 900 keV. This is caused by the values of ^{88}Y and ^{60}Co and is probably symptom of under estimation of the total efficiencies at high energies. The FEPE curves for the W0 and T0 geometries are closer to linear at the high energies on a log-log scale. Because of no data above 1836.1 keV, the activities and their uncertainties given by USS in that energy region should not be accepted without consideration.

8.4 Conclusions

The simulated total efficiency curves were reliable enough to be used in the analysis of gamma spectrometric measurements although the uncertainties of the curves can not be used in the uncertainty estimation. The TCS correction factors should not be taken as such without consideration for nuclides with complex decay schemes or with coincidence effects at energies between 20 keV and 40 keV, where the uncertainty of the total efficiencies is high and the total efficiency large enough for the TCS effects to be noticed. More reliable total efficiency curves would be achieved with the use of other nuclides but the list of suitable and easily attainable sample materials is short.

Other types of methods for the TCS correction factor calculation are available [29, 30, 31]. The MC method was selected here because of software availability. The MCNP allowed more accurate modeling than GESPECOR and therefore the MCNP was used for the W1 model simulations. The MCNP is widely used in efficiency calibrations and allows fitting the total efficiency curve to experimental values. The comparison between MCNP and GESPECOR gave validation to the method of using the MCNP. The differences in Table 7.13 were less than 3.5% and the difference behaved statically. If the two models were fitted to same experimental values, the resulting FEPE curves would be close to each other.

Comparisons of the MCNP and GESPECOR were not found in literature. Therefore the comparison done in this thesis might be of interest to users of the two programs. This comparison was concise and more rigorous comparisons might be done in future. The modeling of the W1 detector in the MCNP differed with methods found in literature. The crystal shape is usually assumed to be cylindrical, which in this case would have been a clearly erroneous assumption.

The shapes of the FEPE curves were similar to the ones in literature [22, 24, 23]. The results were difficult to compare since there are no publications where the

measurement geometry is identical. The closest one found was in ref. [24] where the sample with 35 mm height was inside a 28 mm diameter well. The FEPE values are similar to K40 geometry FEPE values of W1 through the whole energy range. The uncertainties of the efficiencies are on average lower for K40 but it was not mentioned how the uncertainties were calculated. The TCS correction factors or the total efficiencies could not be compared with any values given in literature. The shape of the total efficiency curve for K40 is similar to that in ref. [29].

The method used in the FEPE calibrations was reliable enough for the calibrations to be used in the accredited gamma spectrometry measurements of environmental samples. The comparison in ref. [23] shows that significantly lower MDAs are achieved in measurements of samples inside the well of a SAGe detector than on top of a BEGe detector. This was the reason for the purchasing of the W1 detector. The limiting factor with W1 is the sample size. The FEPE for the W0 and T0 geometries is higher for B7 than for W1 especially below 100 keV resulting in shorter measurement times (Figures 7.10–7.11). Therefore the Williams and T samples where the interest is in nuclides emitting gamma-rays with energies below 100 keV should preferably be measured with BEGe detectors. For gamma rays with energies above 1 MeV the difference in FEPE is not as significant.

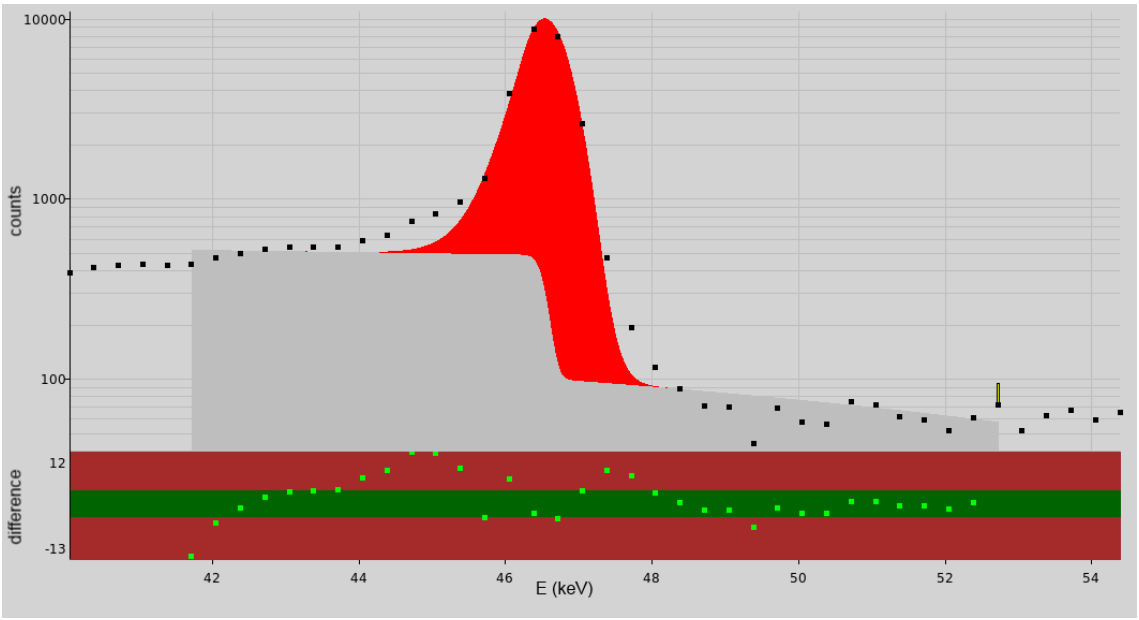

Figure 8.1. Fit done to the 59.5 keV peak of ^{241}Am W0 one-nuclide sample measurement. The peak fit is the red area and the counts are marked with the black dots. The gray area marks the baseline and the peak fitting interval. The lower part shows the difference between the count and fit in standard deviations.

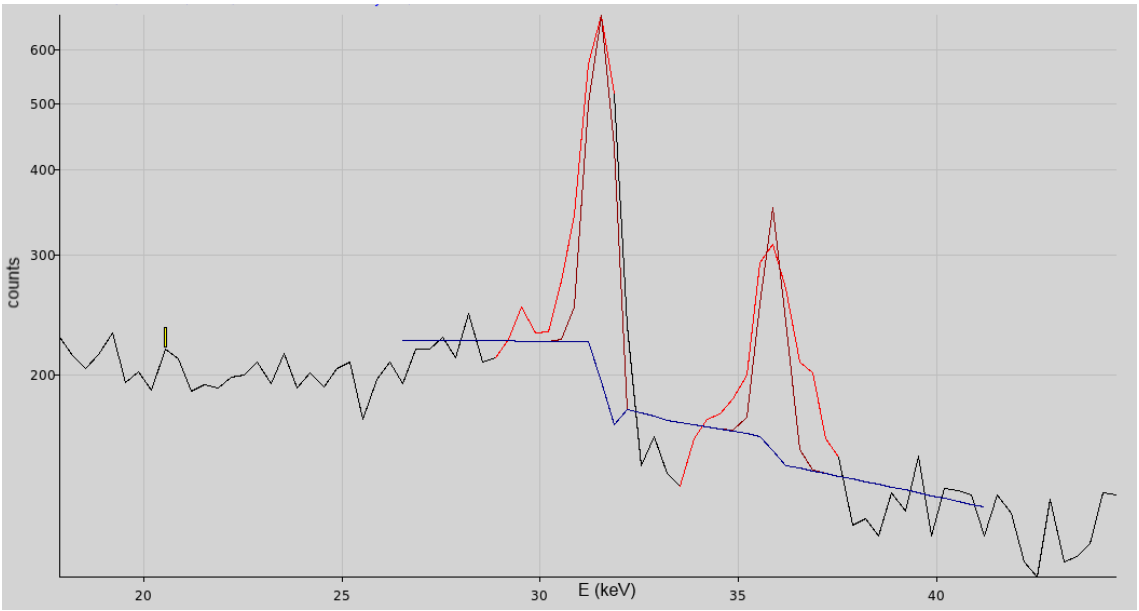

Figure 8.2. The shape of the x-ray peaks from the ^{137}Cs W0 one-nuclide sample spectrum. An automatic fit made by USS is shown in dark red.

References

[1] Glenn F. Knoll. *Radiation Detection and Measurment*. John Wiley & Sons, Inc., 4th edition, 2010.

[2] Michael F. L'Annuziata. *Handbook of Radioactivity Analysis*. Academic Press, 2nd edition, 2003.

[3] G. Yang, H. Mei, Y. T. Guan, G. J. Wang, D. M. Mei, and K. Irmscher. Study on the properties of high purity germanium crystals. *Journal of Physics: Conference Series*, 606(1):12–13, 2015.

[4] A.I. Kalinin and V.A. Bednyakov. Pulse shaping for Ge-spectrometers optimized for ballistic deficit and electronic noise. *Nuclear Instruments and Methods in Physics Research Section A: Accelerators, Spectrometers, Detectors and Associated Equipment*, 538(1–3):718 – 722, 2005.

[5] Nikola Marković, Per Roos, and Sven P. Nielsen. Low-level gamma-ray spectrometry for the determination of 210Pb. *Journal of Radioanalytical and Nuclear Chemistry*, 311(2):1473–1478, 2017.

[6] M.C. Lépy, A. Pearce, and O. Sima. Uncertainties in gamma-ray spectrometry. *Metrologia*, 52(3):123–145, 2015.

[7] P. Aarnio, J. Ala-Heikkilä, and T. Hakulinen. Shaman, Expert System for Radionuclide Identification, User's Guide. *Version 1.9*, 2008.

[8] G.L. Molnár, Zs. Révay, and T. Belgya. Wide energy range efficiency calibration method for Ge detectors. *Nuclear Instruments and Methods in Physics Research Section A: Accelerators, Spectrometers, Detectors and Associated Equipment*, 489(1–3):140 – 159, 2002.

[9] S. Hurtado, M. García-León, and R. García-Tenorio. A fitting algorithm based on simulated annealing techniques for efficiency calibration of HPGe detectors using different mathematical functions. *Nuclear Instruments and Methods in Physics Research Section A: Accelerators, Spectrometers, Detectors and Associated Equipment*, 594(3):362 – 367, 2008.

[10] S. J. Gelsema. *Advanced Gamma-ray Spectrometry Dealing With Coincidence And Attenuation Effects; A Three Curves Approach*. PhD thesis, Delft University of Technology, Delft, The Netherlands, 2001.

[11] François O. Bochud, Jean-Pascal Laedermann, and Octavian Sima. Uncertainty associated with Monte Carlo radiation transport in radionuclide metrology. *Metrologia*, 52(3):191–199, 2015.

[12] M.C. Lépy, T. Altzitzoglou, D. Arnold, F. Bronson, R.Capote Noy, M. Décombaz, F. De Corte, R. Edelmaier, E.Herrera Peraza, S. Klemola, M. Korun, M. Kralik, H. Neder, J. Plagnard, S. Pommé, J. de Sanoit, O. Sima, F. Ugletveit, L. Van Velzen, and T. Vidmar. Intercomparison of efficiency transfer software for gamma-ray spectrometry. *Applied Radiation and Isotopes*, 55(4):493 – 503, 2001.

[13] Dirk Arnold and Octavian Sima. Application of GESPECOR software for the calculation of coincidence summing effects in special cases. *Applied Radiation and Isotopes*, 60(2–4):167 – 172, 2004. Proceedings of the 14th International Conference on Radionuclide Metrology and its Applications, ICRM 2003.

[14] T. Goorley et al. Initial MCNP6 Release Overview. *Nuclear Technology*, 180:298–315, 2012.

[15] X-5 Monte Carlo Team. *MCNP — A General Monte Carlo N-Particle Transport Code, Version 5; Volume I: Overview and Theory*. Los Alamos National Laboratory, 2008.

[16] P. Aarnio, M. Nikkinen, and J. Routti. UniSAMPO, Advanced Gamma Spectrum Analysis Software. *Version 2.4*, 2006.

[17] NUDAT 2.6. http://www.nndc.bnl.gov/nudat2/. *National Nuclear Data Center*, 2017.

[18] Jarmo Ala-Heikkilä Baryon Oy. Personal communication, 2017.

[19] O. Sima, D. Arnold, and C. Dovlete. Gespecor: A versatile tool in gamma-ray spectrometry. *Journal of Radioanalytical and Nuclear Chemistry*, 248(2):359–364, 2001.

[20] GESPECOR. Version 4.2 Manual. *CID Media GmbH*, 2007.

[21] Datasheet. Small Anode Germanium Well Detector. *Mirion Technologies (Canberra)*, 2016. Referenced 15.2.2017.

[22] A.S. Adekola, J. Colaresi, J. Douwen, W.F. Mueller, and K.M. Yocum. Performance of a small anode germanium well detector. *Nuclear Instruments and Methods in Physics Research Section A: Accelerators, Spectrometers, Detectors and Associated Equipment*, 784:124 – 130, 2015. Symposium on Radiation Measurements and Applications 2014 (SORMA XV).

[23] A. S. Adekola, J. Colaresi, J. Douwen, H. Jäderström, W. F. Mueller, K. M. Yocum, and K. Carmichael. Characteristic Performance Evaluation of a New SAGe Well Detector for Small and Large Sample Geometries. *IEEE Transactions on Nuclear Science*, 63(3):1570–1577, June 2016.

[24] R. Britton and A.V. Davies. Characterisation of a SAGe well detector using GEANT4 and LabSOCS. *Nuclear Instruments and Methods in Physics Research Section A: Accelerators, Spectrometers, Detectors and Associated Equipment*, 786:12 – 16, 2015.

[25] Fabien Courtine, Thierry Pilleyre, Serge Sanzelle, and Didier Miallier. Ge well detector calibration by means of a trial and error procedure using the dead layers as a unique parameter in a Monte Carlo simulation. *Nuclear Instruments and Methods in Physics Research Section A: Accelerators, Spectrometers, Detectors and Associated Equipment*, 596(2):229 – 234, 2008.

[26] A. Elanique, O. Marzocchi, D. Leone, L. Hegenbart, B. Breustedt, and L. Oufni. Dead layer thickness characterization of an HPGe detector by measurements and Monte Carlo simulations. *Applied Radiation and Isotopes*, 70(3):538 – 542, 2012.

[27] E. Andreotti, M. Hult, G. Marissens, G. Lutter, A. Garfagnini, S. Hemmer, and K. von Sturm. Determination of dead-layer variation in HPGe detectors. *Applied Radiation and Isotopes*, 87:331 – 335, 2014. Proceedings of the 19th International Conference on Radionuclide Metrology and its Applications 17–21 June 2013, Antwerp, Belgium.

[28] T. Vidmar, I. Aubineau-Laniece, M.J. Anagnostakis, D. Arnold, R. Brettner-Messler, D. Budjas, M. Capogni, M.S. Dias, L-E. De Geer, A. Fazio, J. Gasparro, M. Hult, S. Hurtado, M. Jurado Vargas, M. Laubenstein, K.B. Lee, Y-K. Lee, M-C. Lepy, F-J. Maringer, V. Medina Peyres, M. Mille, M. Moralles, S. Nour, R. Plenteda, M.P. Rubio Montero, O. Sima, C. Tomei, and G. Vidmar. An intercomparison of Monte Carlo codes used in gamma-ray spectrometry. *Applied Radiation and Isotopes*, 66(6–7):764 – 768, 2008. Proceedings of the 16th International Conference on Radionuclide Metrology and its Applications.

[29] H. Jäderström, W.F. Mueller, V. Atrashkevich, and A.S. Adekola. True coincidence summing correction and mathematical efficiency modeling of a well detector. *Nuclear Instruments and Methods in Physics Research Section A: Accelerators, Spectrometers, Detectors and Associated Equipment*, 784:264 – 268, 2015. Symposium on Radiation Measurements and Applications 2014 (SORMA XV).

[30] Pierino De Felice, Paola Angelini, Aldo Fazio, and Roberto Biagini. Fast procedures for coincidence-summing correction in γ-ray spectrometry. *Applied Radiation and Isotopes*, 52(3):745 – 752, 2000.

[31] H. Yücel, A. N. Solmaz, E. Köse, and D. Bor. A semi-empirical method for calculation of true coincidence corrections for the case of a close-in detection in gamma-ray spectrometry. *Journal of Radioanalytical and Nuclear Chemistry*, 283(2):305–312, 2010.